UCLA
UCLA Electronic Theses and Dissertations

Title
Material and Device Design for Rapid Response and Long Lifetime Proton Exchange Membrane Fuel Cells (PEMFCs)

Permalink
https://escholarship.org/uc/item/8mj253np

Author
Shen, Gurong

Publication Date
2018

Peer reviewed|Thesis/dissertation

eScholarship.org Powered by the California Digital Library
University of California

UNIVERSITY OF CALIFORNIA

Los Angeles

Material and Device Design for Rapid Response and Long Lifetime Proton Exchange Membrane Fuel Cells (PEMFCs)

A dissertation submitted in partial satisfaction of the

requirements for the degree Doctor of Philosophy

in Chemical Engineering

by

Gurong Shen

2018

©Copyright by

Gurong Shen

2018

ABSTRACT OF THE DISSERTATION

Material and Device Design for Rapid Response and Long Lifetime Proton Exchange Membrane Fuel Cells (PEMFCs)

by

Gurong Shen

Doctor of Philosophy in Chemical Engineering

University of California, Los Angeles, 2018

Professor Yunfeng Lu, Chair

Proton exchange membrane fuel cells (PEMFCs) have been regarded as the most promising candidate for fuel cell vehicles and tools. Their broader adaption, however, has been impeded by cost and lifetime, as well as the inability to respond to fluctuations associated with operation conditions, fuel supply, and transient load. In this dissertation, a novel strategy to improve the performance and durability of PEMFCs for automotive application is purposed. Unlike the conventional hybrid strategies, which batteries or capacitors are always integrated with the fuel cell to achieve high fuel efficiency and high-power output, the novel fuel cell is integrated with energy-storage materials to form a hybrid device.

Tungsten oxide is proved to be a promising energy-storage material using in the PEMFC application, which has high chemical stability and excellent electrochemical performance in the fuel cell configuration. By integrating a thin layer of tungsten oxide (WO_3) within the anodes, novel PEMFCs shows significantly enhanced power performance for transient operation, as well as improved durability against adverse operating conditions. Meanwhile, the enhanced power performance minimizes the use of auxiliary energy-storage systems and reduces costs.

In addition, the mechanisms of degradation of PEMFCs, as well as the working principles of WO_3 in the hybrid cell are studied. The WO_3 layer in the hybrid cell serves as a rapid-response hydrogen reservoir, oxygen scavenger, sensor for power demand, and regulator for hydrogen-disassociation reaction, effectively stabilize the anode potential and inhibit rising of the anode potential during the transient conditions.

The dissertation of Gurong Shen is approved.

Dante A. Simonetti

Vasilios Manousiouthakis

Yang Yang

Yunfeng Lu, Committee Chair

University of California, Los Angeles

2018

TABLE OF CONTENTS

LIST OF FIGURES

LIST OF TABLES

ACKNOWLEDGEMENT

I would like to give my sincere gratitude to Dr. Yunfeng Lu, for providing me with the opportunity of being his student, which always makes me feel lucky. I wish to express my thanks to my academic committee members, Dr. Vasilios Manousiouthakis, Dr. Dante Simonetti, and Dr. Yang Yang for their guidance and help. In particular, I appreciate the generous help from Dr. Jing Liu. She taught me so much valuable knowledges and skills about fuel cell fabrication and measurement. I thank Dr. Haobin Wu for his suggestions. I also appreciate the assistance provided by Dr. Xiaoyan Liu, Dr. Gen Chen, Dr. Haiping Wu, Dr. Jiangqiang Shen. Thanks all the group members in UCLA, especially, thank Zaiyuan Le, Xinru Li, Shen Li, and Xupeng Cheng.

I finally thank my parents in China for their precious love and support through all of the years.

VITA

2006-2009 B. S., Chemical Engineering

Tianjin University

Tianjin, P. R. China

2009-2018 Teaching Assistant, Research Assistant

Department of Chemical and Biomolecular Engineering

University of California, Los Angeles, USA

Chapter 1. Introduction and Overview of the Research

1.1 Background

Energy is one of the most crucial topics in the 21th century. Nowadays fossil fuels remain the primary resource for world energy supply. In the USA in 2017, about 37% and 14% of total energy consumption came from petroleum and coal respectively. Especially for the transportation sector, petroleum provided 92% energy consumption.[1] With the increasingly worsened environmental pollution and energy constraints caused by vast fossil fuels consumption, the need for seeking clean and renewable energy sources to substitute fossil fuels has become all the more pressing. Energy storage and conversion as the intermediate step to efficient use of energy, has attracted worldwide attention and mounting researching interest.[2]

Electrical energy is the most important secondary energy source and the primary form of consumed energy and is indispensable in the fast-developing modern society. Therefore, much effort has been dedicated to developing the new, low-cost and environmentally friendly energy conversion and storage systems. Systems for electrochemical energy storage and conversion include batteries, electrochemical capacitors (ECs) and fuel cells. They can be used either as power source or as energy storage medium to store electricity in the form of chemical energy. Electrochemical devices and systems are commonly used in consumer electronics, such as cell phones, laptops, portable tools and mobile electric devices. In addition, they are growing in popularity for defense, electric vehicles and aerospace applications.[3]

A Ragone plot as shown in **Figure 1-1** discloses that supercapacitors can be considered to be high-power systems, whereas fuel cells are considered to be high-energy systems. Batteries have intermediate power and energy characteristics. High power and high energy can best be achieved when the available electrochemical power systems are combined.[4]

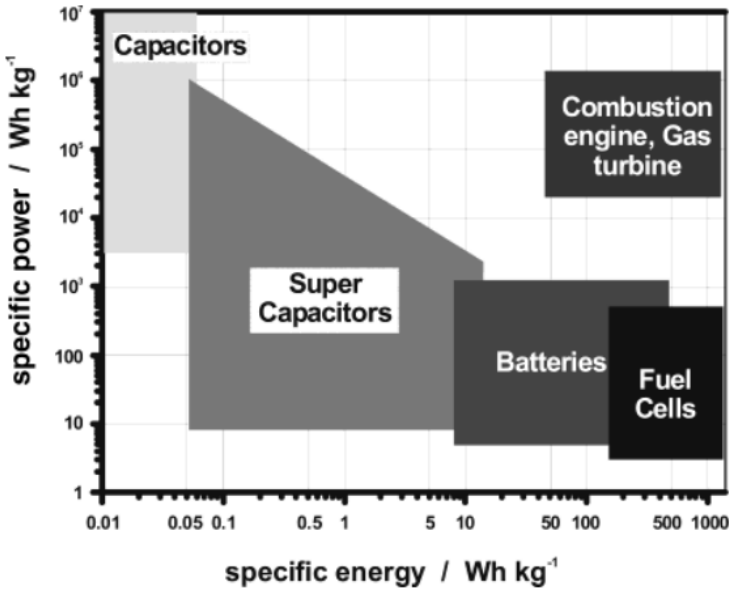

Figure 1-1. Simplified Ragone plot of the energy storage domains for the various electrochemical energy conversion systems compared to an internal combustion engine and turbines and conventional capacitors.[5]

1.2 Overview of fuel cell technology

A fuel cell is an electrochemical device that converts the chemical energy from a fuel into electricity. The fuel (e.g., hydrogen, methanol, and hydrocarbon) at the anode side of the cell is oxidized, while the oxidant (oxygen) at the cathode is reduced. During the electrochemical redox process, ions pass through the electrolyte and electrons travel

through the external circuit from the anode side to the cathode side. The flow of electrons during these electrochemical processes generates the electric current, while potential difference between the two electrodes based upon the nature of the redox reactions gives rise to voltage of the cell.[6]

A fuel cell is in some aspects similar to a battery. These two kinds of electrochemical devices are both comprised of an electrolyte, and negative and positive electrodes, and they generate DC electricity through electrochemical reactions. However, unlike a battery, a fuel cell can work continuously as long as the fuel and oxidant are supplied.[6] In this way, the pattern of using a fuel cell is more similar to the conventional internal combustion engine, except that a fuel cell produces electricity directly while an engine generates mechanical energy.

1.2.1 A brief history of fuel cells

The history of the fuel cell can be traced back to 19 century. The concept of using the gaseous fuels to generate electricity was proposed by Sir William Grove in 1839. The so-called "Gaseous Voltaic Battery" set up by Grove was a rudimentary apparatus shown in **Figure 1-2**, which looks nothing like current fuel cell devices.[7]

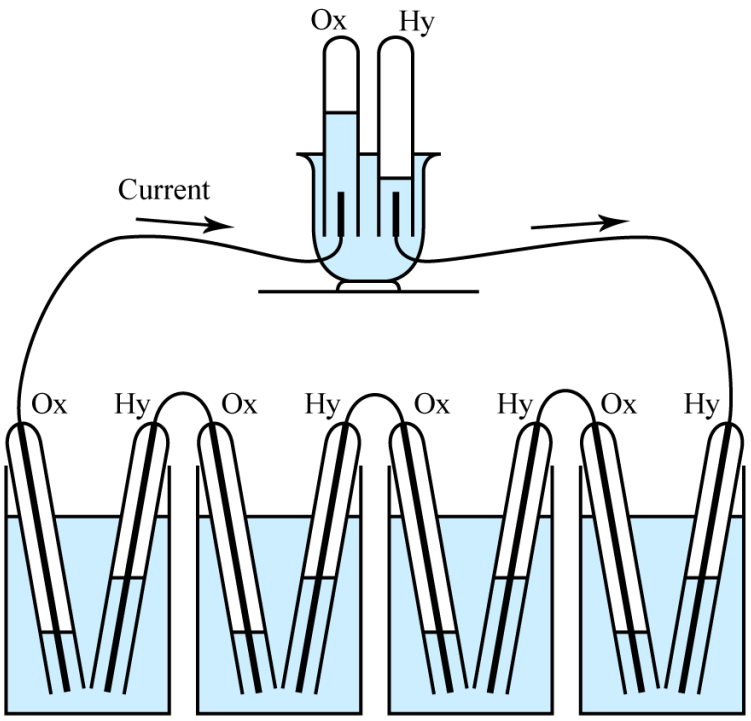

Figure 1-2. The schematic of "Gaseous Voltaic Battery" invented by Sir William Grove.[8]

However, the fuel cell remained nothing more than a scientific curiosity for almost a century. Until another Englishman, Francis T. Bacon, who started working on practical fuel cell in 1937. By the end of the 1950s, Bacon developed a 6 kW fuel cell. The first practical applications of fuel cell were in the U.S. Space Program. The first polymer membrane fuel cells developed by General Electric were used in the Gemini Program in the early 1960s. After that, the Apollo Space Program also used the fuel cells to provide electricity for life support and communications.[7]

For the next several decades, the applications of fuel cells were limited in the U.S. Space Program and military. In 1993, Ballard Power Systems, an emerging Canadian company, demonstrated fuel cell-powered buses. By the support of the U.S. Department

of Energy, almost every car manufacturer had built and demonstrated a fuel cell-powered vehicle by the end of the century and ushered in a new era of the fuel cell industry.[7] As to 2017, about 6500 fuel cell electric vehicles (FCEVs) have been leased or sold worldwide. The Mirai, developed by Toyota (**Figure 1-3**), is the first FCEV model to be sold commercially in 2015. Honda and Hyundai also launched their FCEVs, the Honda Clarity and the Hyundai ix35.[9]

With the efforts of several generations, scientists and researchers have invented various kinds of fuel cells. More and more novel materials are being applied to fuel cell technology to give fuel cells new characteristics such as flexibility and portability. The applications of fuel cells have been expanded to many areas, for example, stationary power generation, cogeneration and power systems for telecommunication.

Figure 1-3. Photo of the Mirai, Toyota.

1.2.2 Classifications of fuel cells

All of the fuel cells work in the similar way, i.e., a fuel is oxidized into electrons and protons; oxygen is reduced to oxide species; proton or ions are transported through the ion-conducting but electronically insulating electrolyte.[10]

Fuel cells can be sorted based on the type of electrolyte used in a fuel cell, namely:

Alkaline fuel cell (AFC) use concentrated (85 wt%) KOH as the electrolyte for the high temperature operation (250 °C) and less concentrated (35-50 wt%) for lower temperature operation (<120 °C). The electrolyte is retained in a matrix (usually asbestos), and a wide range of electrocatalysts can be used (such as Ni, Ag, metal oxides, and noble metals). This fuel cell is intolerant to CO_2 present in either fuel or oxidant. Alkaline fuel cells have been used in the space program (Apollo and Space Shuttle) since the 1960s.

Polymer electrolyte membrane or proton exchange membrane fuel cells (PEMFC) use a thin (≤ 50 μm) proton conductive polymer membrane (such as perfluorosulfonated acid polymer) as the electrolyte. The catalyst is typically platinum supported on carbon with loadings of about 0.3 mg/cm^2, or, if the hydrogen feed contains minute amounts of CO, Pt-Ru alloys are used. Operating temperature is typically between 60 and 80 °C. PEM fuel cells are a serious candidate for automotive applications, but also for small-scale distributed stationary power generation, and for portable power applications as well.

Phosphoric acid fuel cells (PAFC) use concentrated phosphoric acid (~ 100 %) as the electrolyte. The matrix used to retain the acid is usually SiC, and the electrocatalyst in both the anode and the cathode is platinum. Operating temperature is typically between 160 and 220 °C. Phosphoric acid fuel cells are already semicommercially available in container packages (200 KW) for stationary electricity generation (UTC Fuel cells). Hundreds of units have been installed all over the world.

Molten carbonate fuel cells (MCFC) have the electrolyte composed of a combination of alkali (Li, Na, K) carbonates, which is retained in a ceramic matrix of $LiAlO_2$. Operating temperatures are between 600 and 700 °C where the carbonates form a highly conductive molten salt, with carbonate ions providing ionic conduction. At such

high operating temperatures, noble metal catalysts are typically not required. These fuel cells are in the precommercial/demonstration stage for stationary power generation.

Solid oxide fuel cell (SOFC) use a solid, nonporous metal oxide, usually Y_2O_3-stabilized ZrO_2 (YSZ) as the electrolyte. These cells operate at 800 to 1000 °C where ionic conduction by oxygen ions takes place. Similar to MCFC, these fuel cells are in the precommercial/demonstration stage for stationary power generation, although smaller units are being developed for portable power and auxiliary power in automobiles.

The basic principles and electrochemical reactions in various fuel cell types are summarized in **Table 1-1**.

Sometimes, a direct methanol fuel cell (DMFC) is categorized as a separated type of fuel cell; however, according to the precious categorization (based on electrolyte), it is essentially a polymer membrane fuel cell that uses methanol instead of hydrogen as a fuel.[10]

Table 1-1. The basic principles and electrochemical reactions in major fuel cell types.[10]

	AFC	PEMFC	DMFC	PAFC	MCFC	SOFC
Electrolyte	Alkaline	Polymer Membrane	Direct Methanol	Phosphoric Acid	Molten Carbonate	Solid Oxide
Operating temp. (°C)	< 100	60 - 120	60 - 120	160 - 220	600 - 800	800 – 1000 or 500 - 600
Anode reaction	$H_2+2OH^- \rightarrow 2H_2O+2e^-$	$H_2 \rightarrow 2H^++2e^-$	$CH_3OH+H_2O \rightarrow CO_2+6H^++6e^-$	$H_2 \rightarrow 2H^++2e^-$	$H_2+CO_3^{2-} \rightarrow H_2O+CO_2+2e^-$	$H_2+O^{2-} \rightarrow H_2O+2e^-$
Cathode reaction	$1/2O_2+H_2O+2e^- \rightarrow 2OH^-$	$1/2O_2+2H^++2e^- \rightarrow 2H_2O$	$3/2O_2+6H^++6e^- \rightarrow 6H_2O$	$1/2O_2+2H^++2e^- \rightarrow 2H_2O$	$1/2O_2+CO_2+2e^- \rightarrow CO_3^{2-}$	$1/2O_2+2e^- \rightarrow O^{2-}$
Realized power	5 – 150 KW	5- 250 KW	5 KW	50 KW – 11 MW	100 KW – 2 MW	100 – 250 KW
Charge carrier in electrolyte	OH^-	H^+	H^+	H^+	CO_3^{2-}	O^{2-}
Applications	Transportation, space, military, energy storage systems		Combined heat and stationary power		Combined heat and stationary power and transportation	

1.3 Introduction of PEM fuel cell

Among various types of fuel cells, a considerable body of research work has been carried out to develop highly efficient and reliable single PEM fuel cell and stacks to be utilized in various applications such as portable devices as a power source, stationary and automotive applications. Significant development has been achieved recently, especially in materials and current density, which will eventually lead to increasing the power density and make the device more efficient and reliable.

Through this section, the basic working principle, operation, design, and materials of PEMFCs have been introduced.

1.3.1 Basic Reactions

A fuel cell is an electrochemical energy converter, it converts chemical energy of fuel directly into electricity. As such, it must obey the laws of thermodynamics.

The electrochemical reactions in fuel cells happen simultaneously on both sides of the membrane, the anode and the cathode. The basic fuel cell reactions are[10]:

At the anode:

$$H_2 \rightarrow 2H^+ + 2e^- \tag{1-1}$$

corresponding to an anode potential $E_a^0 = 0.00$ V (under standard conditions) versus SHE.

At the cathode:

$$^1/_2O_2 + 2H^+ + 2e^- \rightarrow H_2O \tag{1-2}$$

corresponding to a cathode potential $E_c^0 = 1.229$ V (under standard conditions) versus SHE.

Therefore, the overall reaction is:

$$H_2 + {}^1/_2O_2 \rightarrow H_2O \tag{1-3}$$

with the equilibrium standard electromotive force calculated to be 1.299 V. These reactions may have several intermediate steps, and some (unwanted) side reactions may occur, but for now these reactions accurately describe the main processes in a fuel cell.

The oxygen reduction reaction (ORR) is well recognized as sluggish.[11] The ORR process on Pt catalysts includes several individual reactions, as show in **Figure 1-4**. Two general processes are the most studied. One is the production of water through a four-electron pathway, and the other is production of hydrogen peroxide through a two-electron pathway. The desired route of a successful ORR catalyst would reduce oxygen molecules to water through four-electron pathway. Incomplete reduction of oxygen to hydrogen peroxide not only leads to low energy conversion efficiency, but also produce reactive intermediate that can further convert to harmful free radical species.

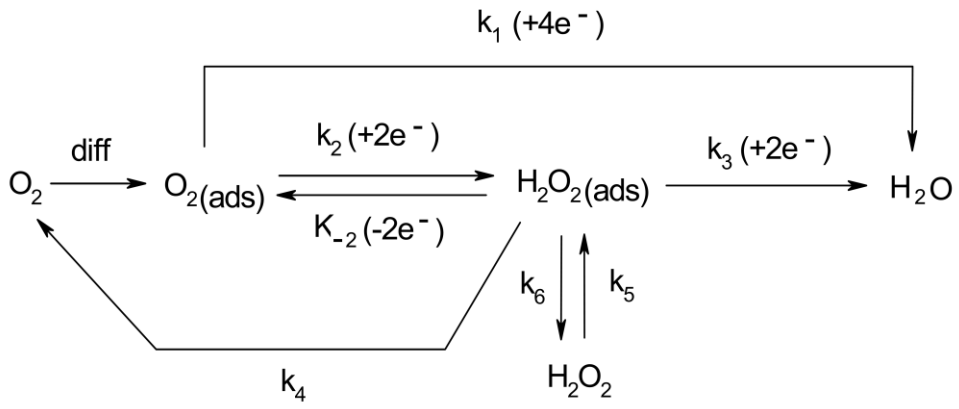

Figure 1-4. The ORR process on Pt catalysts.[11]

The hydrogen oxidation reaction (HOR) at the anode is a simple one electron reaction but is also with a reaction mechanism involving several steps. The overall reaction rate depends on the slowest elementary reaction, which is called the rate determined step. The steps of H_2 oxidation on Pt catalyst include the following:

$$H_2 + Pt \rightarrow Pt\text{-}H_2 \quad (1\text{-}4)$$

$$Pt\text{-}H_2 \rightarrow Pt\text{-}H_{ads} \quad (1\text{-}5)$$

$$Pt\text{-}H_{ads} \rightarrow Pt + H^+ + e^- \quad (1\text{-}6)$$

Platinum (Pt)-based catalysts are widely used as the anodic electrode material for hydrogen oxidation. The HOR on Pt catalysts has a lower overpotential and a higher kinetic rate comparing with other non-Pt catalysts. The apparent exchange current density of the HOR has been calculated to be $i^0_{anode} = 0.1\ Acm^{-2}$, which is extremely high compared with that of ORR ($i^0_{cathode} = 6\ \mu Acm^{-2}$), according to the charge transfer resistances of the cathode and anode obtained from electrochemical impedance spectroscopy (EIS) measurements done by Wagner *et al.*.[12]

However, although the reaction rate of HOR on Pt catalyst is very fast, the Pt catalyst is sensitive to carbon monoxide (CO) especially at temperatures lower than 100 °C. CO can strongly adsorb on the Pt catalyst and block the catalytically active area, thereby significantly decreasing its reactivity and causing so-called "CO poisoning". Even trace amount (10 ppm) of CO in the H_2 fuel will influence the performance and durability of the Pt catalyst dramatically, the presence of a trace level of CO in the hydrogen-rich gas mixture produced by the reforming of the other fuels is inevitable. Due to this, an excellent anode catalyst in PEM fuel cells has to show not only high catalytic activity toward hydrogen oxidation, but also enhanced durability in the presence of CO. The search for CO-tolerant catalysts has been a challenging task in the successful development of more efficient PEMFC systems.[13]

1.3.2 The Cell Voltage and Overpotentials

The reversible (Nernst) potential, E_{rev}, is defined as the cell potential at the equilibrium or reversible state, where no irreversibility exist in the system. The reversible potential of the anode in a PEMFC, where hydrogen oxidation reaction occurs, is 0 V. For the PEMFC cathode, where the oxygen reduction reaction occurs on Pt catalysts, the reversible potential is 1.23 V at 25 °C and 1 atm with liquid water as the product.

The terminal cell potential, E, is the voltage drop measured at the external electrical load. The open circuit voltage, E_{ocv}, is the potential obtained when the external circuit is open. In general, $E < E_{ocv} < E_{rev}$.

The ideal voltage (1.23 V) is unattainable due to losses inherent to the system. The potential losses used to run the cell itself are called overpotentials.[7] As shown in **Figure 1-5**, there are three kinds of overpotentials in the PEMFC, which are activation, ohmic, and concentration overpotential losses.

Activation Loss

The activation loss arises due to the energy required to drive the chemical reactions at the anode and cathode electrode surfaces.[7] This overpotential loss is determined by the catalytic activity of the electrodes, and can be modeled using the following equation:

$$V_{act} = V_0 + V_a(1 - e^{-c_1 \cdot i})$$

where V_0, V_a and c_1 depend on the oxygen partial pressure and temperature. These values can be determined from a regression of experimental data.

Ohmic Loss

The ohmic loss results from the resistance of the membrane to proton transfer and the electrode and collector plate to electron transfer. Ohmic losses expressed as:

$$V_{ohm} = i \cdot R_{ohm}$$

where R_{ohm}, the membrane's internal electrical resistance, is defined as the ratio of the membrane thickness t_m to its electrical conductivity σ_m,

$$R_{ohm} = \frac{t_m}{\sigma_m}$$

For the Nafion membrane, the membrane conductivity is a function of the membrane water content and is found using the empirical relations:

$$\sigma_m = b_1 \exp(b_2(\frac{1}{303} - \frac{1}{T_{fc}}))$$

$$b_1 = b_{11}\lambda_m - b_{12}$$

where b_2, b_{11}, and b_{12} are empirically determined constants specific to the membrane being used. Given the strong dependence of this term on the membrane humidity, the ohmic losses can vary substantially with the humidity level.

Each of the above overpotentials dominates at different current density regions. As shown in **Figure 1-5**, when the current density is low, the activation overpotential is the main loss mechanism. The ohmic losses dominate at the middle current density region. As the current density continues increasing, the mass transport limitation – concentration overpotential become important.

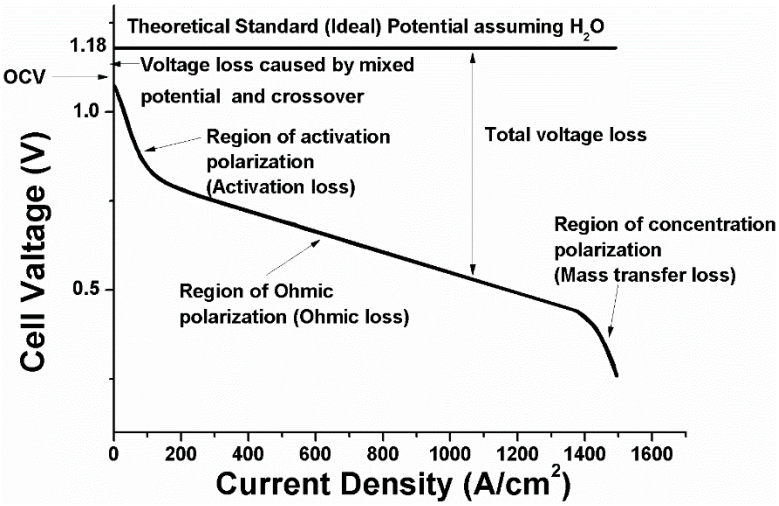

Figure 1-5. Typical polarization curve for a PEM fuel cell stack.

1.3.3 Components of a PEMFC

In general, a PEMFC consists of current collector, gas distributor and membrane electrode assembly (MEA).[10] **Figure 1-6** is a structure scheme of a typical PEMFC single cell. Among these components, the current collector is usually made of common metals with high electrical conductivity such as copper or aluminum. The gas distributor, in the form of monopolar plate in a single cell and a bipolar plate in a PEMFC stack, is injection-molded from a graphite plate with grooved gas channels to transport the reactant gases to the reaction sites. The membrane electrode assembly is an assembly, where the electrochemical reactions occur, with sandwich structure forming by two electrodes and an electrolyte membrane. The major parts in the MEA are gas diffusion layer (GDL), catalyst layer, and membrane.

Gas diffusion layer which is currently made from carbon fiber or carbon cloth because carbon-based materials are stable in acid environment. Its thickness is normally

between 200 and 300 μm. The main functions of GDL are providing high gas permeability and good electronic conductivity, providing elasticity under compression.

Using a dual-layer GDL has been approved as one of the most effective approaches to reduce mass transfer limitation in PEM fuel cells. Generally, a dual-layer GDL is composed of a carbon-fiber woven cloth or non-woven paper substrate that functions as a gas diffuser and as a mechanical support for the electrode, and a thin microporous layer (MPL) that comprises carbon black powder and hydrophobic agent, typically PTFE. The MPL reduces contact resistance between the catalyst layer and the macroporous carbon substrate by forming flat and uniform layer that is not permeable to the catalyst particles. More importantly, it has been widely reported that the MPL enhances water management in the MEA, resulting in the improvement in fuel cell performance.[14]

Another important function of the GDL is that it can absorb the pressure between plate and the membrane. The elasticity of the carbon material allows it to be compressed under pressure and keep its mechanical strength at the same time. The MEAs are assembled between bipolar plates under certain compress stress to ensure the close contact on the interface. During the operation, the membrane would swell or shrink depends on the water content in the membrane. Once the thickness of the membrane changes, the pressure between the plate and the MEA will increase or decrease. The GDL can function as a cushion layer to protect the soft membrane from physical damage.[15]

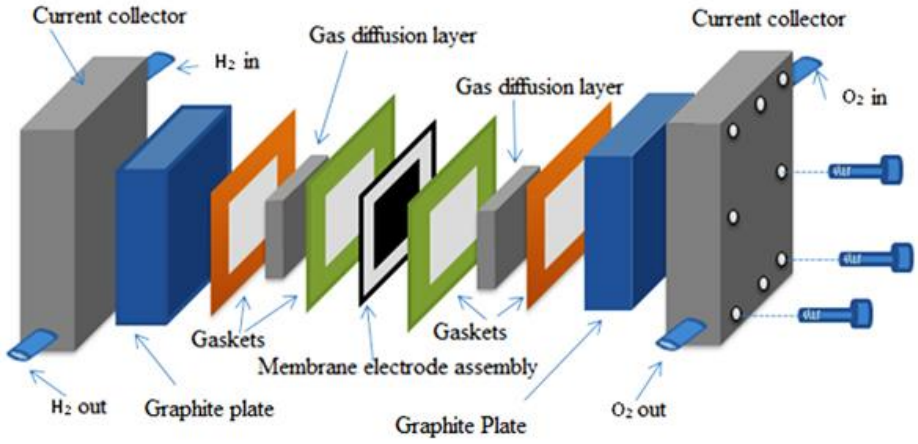

Figure 1-6. Structural schematics of a single PEM fuel cell.

Catalyst layer which is the region where the membrane and the electrodes overlap and the H_2 oxidation or O_2 reduction reaction occurs. It allows electron and ion conduction at the same time. Catalyst layer and gas diffusion layer together compose the electrode. The typical thickness of the catalyst layer in a PEMFC is about 10 μm.

Membrane which can transport the protons with the presence of water but is impermeable to gas and electrons. The membranes should possess good chemical, mechanical and thermal properties in order to withstand the fuel cell reaction environment. The thickness of membrane for hydrogen-air fuel cells is around 50 μm.

1.3.4 Primary Characteristics to Describe a PEMFC

The primary characteristics to describe the performance of a PEMFC are polarization curve and power curve (shown in **Figure 1-5**), limiting current density I, and local current density distribution. As for the transient state, the voltage-time behavior, start-stop performance and the performance under mechanical stress or cyclic operating conditions are usually concerned.

1.4 Reliability and Durability of PEMFCs

Reliability and lifetime analysis play significant roles for PEMFCs in the application of automobiles as well as stationary power sources. How to achieve desired beginning-of-life (BOL) and end-of-life (EOL) performance with lowest cost is the main objective of types of analyses. In general, reliability is defined as the ability of a fuel cell or stack to perform the required function under stated conditions for a period of time. Durability is the ability of a PEM fuel cell or stack to resist permanent change in performance over time. Durability decay does not lead to disastrous failure but simply to decrease in performance which is not recoverable or reversible. Lifetime prediction is based on the study of durability, whose meaning is similar to that of "wearability".[16] The term of stability of a PEM fuel cell is defined as the ability to recover power lost during continuous operation. Stability decay is always concerned with operating conditions such as water management and reversible material changes.[17]

According to the reports expressed by the U.S. Department of Energy (DOE), the targets in terms of lifetime for PEMFCs are 5000h (7 months) for cars and 20,000 h (5.8 years) for buses, and in stationary applications is 40,000 h (11.6 years).[9] The need to satisfy above requirements with optimum system design and material selection necessitates the PEMFC durability study.

Fuel cell power systems must be as durable and reliable as current automotive engines. The DOE targets a durability of 5,000 hours, which is equivalent to approximately 150,000 miles of driving, with less than 10% loss of performance. Also, fuel cell power systems should be able to function over a broad range of external environmental conditions

(-40 to +40 °C) as well as respond to the rapid variation in power demand required in automotive applications.[5]

Like any other applications, reliability modeling and evaluation of PEMFCs involves common methodologies applied in the field of reliability engineering, including the failure mode and effects analysis (FMEA), fault tree analysis (FTA), reliability block diagram (RBD), accelerated reliability engineering testing and cut set and tie set methods, etc.[17] The goal is to predict the values of reliability parameters such as mean time between forces outrages that can be used for setting up maintenance schedules.

By far the systematic reliability modeling for PEMFCs have not been carried out intensively, since the development of PEMFCs itself is still in a revolutionary stage. Nevertheless, a few papers regarding the durability study of PEMFC components have been published in the literature, the review of which is given in the next section.

1.4.1 Durability Study for PEMFCs

There are two ways to investigate the durability of PEMFCs, one of which is by theoretical analysis, the other is by experimental observations. The advantage of theoretical analysis is that it can be employed to predict the degradations in a PEMFC with low cost. But the mathematical modeling being used need detailed descriptions of the possible aging phenomena occurring in the cell components, along with proper incorporations of the aging effects to the performance model. Durability test stand can be utilized to examine the structural and property changes of components under realistic working environments, but the testing cost is very expensive. For example, a bus operation test with PEMFC stack for 20,000 h consumed about 2,000,000 Canadian dollars. The running cost includes supplying the fuel and air, building the test station, and the associated expenses such as electricity,

maintenance and operator.[7] The normal test stands can measure the durability of cells up to 15,000 h, hence is applicable only for automotive and compact type applications. For bus and stationary applications, accelerated stress tests (AST) are more suitable.

The degradation rate of PEMFCs that has been reported in the literature ranges between -27 and -121 μV/cycle under the urban transit authority (UMTA) driving cycles, though much lower rate was also seen.[8] It is necessary to keep in mind that for practical use, PEMFCs may be subjected to the following situations that affect durability to a large extent. PEMFC stacks are actually used instead of single cells; therefore, the issue of uniformity would come to play. High stoichiometric ratio and high operating pressure are not desirable in daily use. Reactant gases may be the reformate and air, and thus not very pure. Low catalyst loading, inexpensive gas diffusion layers and low-cost composite bipolar plates are preferred when manufacturing the real-life MEA. All the factors should be considered when studying the PEMFC durability.

1.4.2 Performance Degradations and Common Failure Modes of PEMFCs

The PEMFCs are involved with the strong acidic environment (pH ≈ 2), oxygen in gaseous phase and dissolved phase, water in vapor and liquid phase, mechanical compression, contamination, high temperature (90 °C for automotive and higher for stationary applications) and dynamic load cycles. Correspondingly the aging processes may occur in the polymer membrane, catalyst layers, electrodes, membrane-catalyst interface, monopolar/bipolar plates, and sealing materials. Therefore, the aging effects could cause the following variables to change: catalyst activity, reactive catalyst surface area, exchange current density, membrane proton conductivity, interfacial resistance,

contact between the cell components, fuel utility, bipolar plate conductivity, thickness of the MEA component, and so on.

In the following section, the sources of degradations in a PEMFC stack and their characterizations as well as effects on performance are browsed through in an order of component position, from inner part to outer part.

1.4.2.1 Membrane Degradation

The membrane is one of the critical and expensive parts in PEM fuel cells. The membrane, which is placed between two electrodes, separates oxidizing gases at the cathode and reduces gases at the cathode and allows protons to pass from the anode to the cathode at same time. To ensure the normal operation of PEM fuel cells, membrane should be of excellent thermal stability, ionic conductivity and chemical and flow reactant gas permeability.[18-20] Most commonly used membranes in PEM fuel cells are produced by Dupont TM (Nafion®), Asahi TM (Aciplex®, Flemion®) and Gore TM (Gore-Select®).

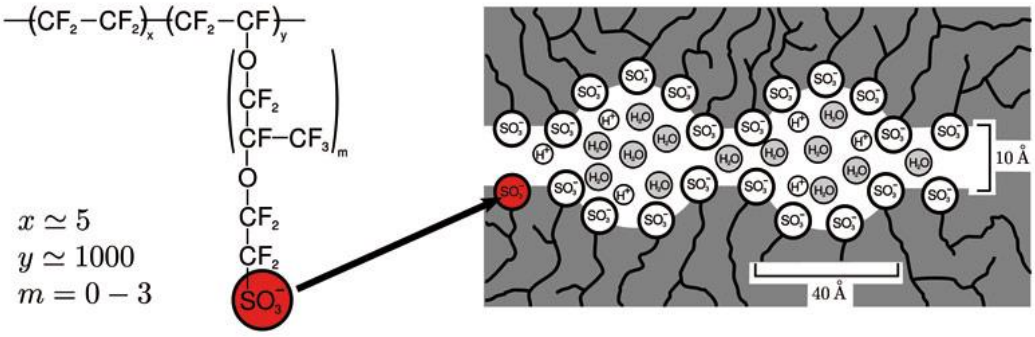

Figure 1-7. Chemical structure and water-filled channels of Nafion®.

Different kinds of membranes decay in diverse rates due to the variances of their chemical structures. For instance, the earlier polystyrene sulfonic acid (PSSA) membrane were proven to degrade at a higher rate compared to Nafion membranes, due to the

chemical attack of peroxide intermediates to the tertiary hydrogen at the α-carbon of the PSSA chain, leading to the simultaneous loss of aromatic rings and the sulfonic acid ($SO^{3-}H^{+}$) groups.[21] The PSSA membrane has relatively low mechanical and dimensional stability. It may physically deform, crack and form some types of perforation, especially when hydration/dehydration cycling- induced local stresses or puncture of catalyst particles is taking place.

Nafion membranes are broadly used in the fuel cell application. The degradation mechanism of nafion membranes has been extensively studied. Nafion is a kind of perfluorinated sulfonic acid (PFSA) membrane developed in the mid-1960s by Dupont. It is based on an aliphatic perfluorocarbon sulfonic acid (**Figure 1-7**), and it exhibited excellent physical properties and oxidative stability in both wet and dry states. It was reported that the Nafion 120 membranes show no deterioration (<0.1%) after 5000h of operation and only 2% degradation after 100,000h of operation.[21] The dissolution and thinning of Nafion membranes occurs at a comparatively slow rate, though pinholes may form at the end. Pinholes can cause the crossover of reactant gases. In this case, the fuel and oxidant react with each other directly on the surface of platinum without generating any electricity. The heat released by fuel and oxidant recombination could be sufficient to melt a small portion of the membrane around the pinholes and make the pinhole even bigger.[21] The sizes and locations of pinholes can be detected by use of an infrared camera.

The detailed membrane thinning mechanisms for fluorinated membranes was proposed by Stucki, Scherrer, Wilson et al..[21] It has been shown that the dissolution of PTFE backbone mainly occurs at the anode side. The gaseous oxygen molecules first dissolve into the membrane, diffuse from the cathode side to the anode side, and then react

with hydrogen molecules chemisorbed on the anode platinum surface and generate hydrogen peroxide (H_2O_2). Because the reduction of hydrogen peroxide is inhibited at the H_2-covered Pt electrode, hydrogen peroxide accumulates at the anode Pt/membrane interface and diffuses back into the membrane. Following this step, the hydroxyl and hydroperoxy radicals are produced within the membrane, which attack the – CHF- groups in the polymer backbones as well as the sulfonic acid groups. The above processes can be summarized in a series of proposed chemical reactions as shown below[21]:

Step 1: $2Pt_{(s)} + H_2 \rightarrow 2Pt{\cdot}H$

Step 2: $Pt{\cdot}H + O_2 \rightarrow Pt{\cdot}HO_2$

Step 3: $Pt{\cdot}HO_2 + H{\cdot} \rightarrow Pt(s) + H_2O_2$

Step 4: $H_2O_2 + M^{2+}$ (Fe^{2+}, Cu^{2+}…) $\rightarrow M^{3+} + OH{\cdot} + OH^-$

Step 5: $OH{\cdot} + H_2O_2 \rightarrow H_2O+HO_2{\cdot}$ (hydrogen peroxide radical attacks the PEM)

It can be seen from above mechanism that the membrane degradation is influenced by the permeation of oxygen and the occurrence of contaminant metal ions in the membrane. If the oxygen dissolution and diffusion rates through the membrane become larger due to higher water content, it may transport more oxygen to the anode side and result in increased peroxide formation at the hydrogen electrode. The presence of liquid water in the membrane could also help transport leached impurities, which may decrease the membrane proton conductivity and water diffusion coefficient via the cation effect, since a large portion of the sulfonic acid groups may be attached with other cations instead of protons due to the high affinity.[21] Nevertheless, the lack of water in the membrane can decrease the proton conductivity, change membrane dimensions and shape by shrinking, and put the membrane under mechanical-electrochemical stresses.

The issue of the thermal stability and thermal degradation of Nafion membranes have been addressed by several studies. The polytetrafluoroethylene (PTFE)-like molecular backbone allows Nafion membrane be relative stable until beyond 150 ℃ due to the strength of the C-F bond and the shielding effect of the electronegative fluorine atoms. Side sulfonate acid groups of Nafion begin to decompose at higher temperatures. The thermal stability of Nafion was investigated by Surowiec and Bogoczek using thermal gravimetric analysis and Fourier transform infrared spectroscopy.[22] Only water was detected below 280 ℃, sulfonic acid groups were split off at temperatures above 280 ℃. Wilkie et al.[23] and Samms et al.[24] proposed the detailed mechanisms for PFSA thermal degradation, including initiative break of the C-S bond to produce Sulphur dioxide, OH· radicals, and a left carbon-based radical for further cleavage at higher temperatures.

1.4.2.2 Catalyst Layers

The degradation of catalyst layer in PEMFCs has been studied by many researchers as another significant factor in durability study, though the relation between platinum catalyst evolution and change of reaction kinetics has not been fully understood. Pt and binary, ternary, or even quaternary Pt-transition metal alloys, such as PtCo, Pt-Cr-Ni, and Pt-Ru-Ir-Sn, supported on conductive supports have been proposed and implemented as electrocatalysts in PEM fuel cells. High-surface-area carbon materials such as Vulcan-XC 72, Ketjen black, or Black pearls BP2000 are commonly used as supports. It should be noticed that the catalyst layer structure and morphology and hence the performance of the cell greatly depend on the catalyst and electrode fabrication methods. The fabrication methods include spread, spray, catalyst powder deposition, ion exchange, electro-deposition, impregnation reduction, evaporative deposition, dry spraying, precipitation,

colloidal method catalyst decaling and painting, and so on.[25] In order to improve the carbon monoxide (CO) poisoning resistance, the platinum is usually alloyed with other noble metals. The content of oxide in the catalysts can influence the H_2 and O_2 adsorption characteristics and also the effective platinum surface area (EPSA) that is defined by EPSA = ECA · Pt utilization · catalyst loading, where ECA is the intrinsic catalyst area.[26]

Catalyst sintering or migration is one of the main causes for the reduction of catalysis activity.[21] It has been shown that the catalyst particle sintering occurs at the cathode side more readily, the mechanism of which was proposed as the dissolution-redeposition of small platinum crystallites. Small Pt particles may dissolve in the ionomer phase and redeposit on the surface of large particles, leading to particle growth, a phenomenon known as Ostwald ripening.[27] The agglomeration of Pt particles may occur at the nanometer scale due to random cluster-cluster collisions of the particles on the carbon support, or at the atomic scale by the minimization of the clusters' Gibbs free energy. Coarsening of the catalyst due to movement of its particles and coalescence on the carbon support can cause the decline of the catalytically active surface area, then further decrease the fuel cell performance.[28] Moreover, the dissolved Pt species may diffuse into the ionomer phase and subsequently precipitate in the membrane via reduction of Pt ions by the crossover hydrogen from the anode side, which dramatically decreases membrane stability and conductivity. For the anode side, the loss of catalyst surface area could be due to the formation of Pt-hydrogen complexes and subsequent moving away from the catalyst/membrane interface.[26]

The reduction of the catalyst effective surface area may also result from the degradation of the membrane phase (ionomer) in the catalyst layer. Once degradation

occurs, it may not only affect the transport of hydrogen ion, but also the dissolution and diffusion of H_2 and O_2 gases to the reaction sites. In this case the exchange current density of the electrochemical reactions will be decreased.

Besides catalyst sintering, the catalyst poisoning and contamination in a PEMFC can occur via two mechanisms, one of which is the geometrical effect by blocking the sites, e.g. only trace amount of carbon monoxide can block part of the platinum reaction sites; the other of which is via electronic effect such as changing the rate or selectivity of the electrochemical reaction by modifying the strength of chemisorption of the nearby sites.[26] The contaminants may come from the reactant gases, recycled liquid water, the degradation products of diffusion media, sealing material and membrane, as well as the corrosion rust of bipolar plate and current collector. What's more, the corrosion of Pt itself into PtO_2 at the cathode side was suggested in Ahn et al.'s paper, although platinum is a noble metal and has very high corrosion resistance.[29]

Corrosion of the catalyst carbon support is another important issue relating to electrocatalyst and catalyst layer durability that has attracted considerable attention. In a normal PEM fuel cell, carbon corrosion is negligible at potentials lower than 1.1 V vs. reversible hydrogen electrode (RHE) due to its slow kinetics. However, recent researches have confirmed that the presence of electrocatalysts like Pt/C or PtRu/C can accelerate carbon corrosion and reduce the potentials for carbon oxidation to 0.55 V (vs. RHE) or lower.[28, 30] Carbon corrosion can cause the drop of the relative percentage of conductive material in the electrode and the increase of the contact resistance with the current collector as well as the internal resistance of the cell. Another serious consequence of carbon

corrosion is the number of sites available to anchor the catalyst decreases, causing catalyst metal sintering.

1.4.2.3 Gas Diffusion Layers (GDL)

The Gas diffusion layer (GDL) is generally a dual-layer carbon-based porous material, which consists of a microporous carbon fiber paper or carbon cloth substrate covered by a microporous layer (MPL) consisting of carbon black powder and a hydrophobic agent.

The changes of gas diffusion layer (GDL) along with time can be reflected in property parameters including porosity, tuotoristy, hydrophilicity and electrical conductivity. The degradations result from the weakness of carbon material subjected to water and oxygen under high temperature and ion contaminations along with the conduction of electrons. Fowler et al. presented that prolonged exposure of the MEA to water could result in a permanent loss of performance due to GDL degradation, involving changes in carbon surface functional groups and GDL porosity, accumulation of hydrophilic impurities and PTFE loss. This may in turn affect the gas and liquid water transport through GDL.[26] However, the detailed mechanisms were not provided.

In addition, the GDL/catalyst layer interfacial delamination was reported occurring in a 5-KW PEMFC stack after an operation of 8000 h, which driven the interfacial resistance to infinity and lead to cell failure.[29] Fowler et al. explained this phenomenon on the basis of localized tensile stresses that were caused by MEA hydration/dehydration. The decomposition of electrode carbon materials as well as its polytetrafluoroethylene (PTFE) coating under electrochemical stress and attack of chemical species such as HOO· radicals may have accelerated the delamination process.[31]

1.4.2.4 Bipolar Plates

The bipolar plate that functions as a separator between the fuel, oxidant gases, and coolant is a multifunctional component of the fuel cell system, which consistently distributes the reactants and produces streams, providing a path to current that produces during the electrochemical reactions. To accomplish all the necessary functions, several characteristics are required for the materials to be suitable for bipolar component, which including, but are not restricted to, high electrical conductivity, low gas permeability, sufficient strength, low thermal resistance, high resistance to corrosion and reasonable manufacturing cost. In addition to graphite, materials such as metals, polymer-based composites with conductive graphite/carbon fillers, and graphite/carbon-based composites are being tested and evaluated.

According to Fowler et al., bipolar plates can corrode, foul, crack, permeate hydrogen, deform and leach contaminants.[26] The transport of reactant gases and water vapor, the electron conduction, thermal and hydration cycling as well as the acidic environment and mechanical compression may cause the degradations of the polymeric bindings in the graphite bipolar plate. Once degradations occur, there would be less adhesion forces between the polymer bindings and the graphite flake sheets, which may lead to the "creeping" of materials, loss of integrity, mechanical strength and electrical conductivity, and changes in the dimensions and shape of grooves. Hence aging may increase the ohmic and contact resistance of the bipolar plates, and also disturb the designed flow field. Commercially available metals and their alloys such as Ni, Al and Ti have shown strong potential for their use in bipolar plates due to their good mechanical properties, high electrical conductivity and low cost. However, the contact resistance

between these metallic bipolar plates and the GDL, which is ascribed to the formation of electrically resistant oxide films on the surfaces that inevitably increase the internal electrical resistance, is still a problem to solve. Stainless steel is considered as a promising material for the bipolar plate due to its wide range of alloy choices and applicability to mass production. But stainless steel is vulnerable to corrosion in aggressive humid and acidic environments inside a PEM fuel cell.[32] Moreover, corrosion of the metallic materials leads to the production of multivalent cations, which can impair the durability of the membrane and catalyst significantly as described in Section 1.4.3.2.[33-34] A chemical analysis of the MEA after 100 h of cell operation revealed that a large quantity of Fe and Ni atoms, as well as traces of Cr, was released from untreated stainless steel 316L.[34] As a result, a voltage drop of up to 300 mV at a current of 700 mA cm^{-2} was detected due to the chemical corrosion of this bipolar plated material.[35]

1.4.2.5 Sealing Materials

Sealing material is placed between the bipolar plates to prevent gas and coolant leakage and crossover. Typical sealing materials using in PEM fuel cells include fluorine caoutchouc, EPDM, and silicone. There is little information from the literature regarding the degradations of sealing materials in a PEM fuel cell. But the possible chemical instability of the sealant to acid and reactant gases may cause the breakdown of the polymer network and release of silicon atoms to the MEA. Swelling experiment and tensile testing can be performed to determine the network crosslink density. Scanning electron microscope-energy dispersive atomic X-ray (SEM-EDAX) machine can be utilized to examine the components of MEA to detect leached contaminants. This is definitely an issue deserving more investigation. One consequence of sealant degradation to the operating

stack is fuel leakage due to loss of elasticity. It can decrease the stoichiometric ratio of fuel and oxidant (mainly fuel) supplied to the cells, lowering the stack power efficiency by reactant starvation.[36]

1.4.3 Operational Effects on Fuel Cell Durability

Operating conditions are known to have an impact on a fuel cell's durability. Although the durability of stationary fuel cell systems in most instances does not reach DOE targets, PEMFC systems applied to micro CHP (<1-25 kW) have demonstrated durability in excess of 70,000 hours. In contrast, a projected lifetime of only 3,900 hours (2015) before 10% degradation for the automotive fuel cell systems was evaluated by the Technology Validation sub-program's Learning Demonstration.[9] This great contrast in the lifetime of fuel cell systems for different applications is ascribed to the difference in the operating conditions undergoing in the various operating circumstances. In this section, effects impact to all kinds of PEM fuel cell systems such like exposure to impurities, changes in temperature and/or relative humidity, and fuel starvation will be discussed. These other conditions including potential cycling, start/stop cycling, and start-up from subfreezing conditions, which are common operations for the automotive application, will be mentioned as well.

1.4.3.1 Impurities

Impurities are known to affect FC performance by various mechanisms that lead to performance loss. Impurities that adsorb onto the anode or cathode electrocatalyst surface inhibit the electrode charge-transfer processes, resulting in interfacial overpotential losses. Impurities such as ammonia, which can form cations, or other cations introduced to the cell directly from salts or corrosion byproducts can cause ion exchange with protons in the

ionomer. These cations lower proton conduction and can result in increased ohmic losses. Foreign substances can also change the water and/or gas transport behavior of the gas diffusion layer and thus adversely affect fuel cell performance by decreasing mass transport.

Performance losses due to impurities can be permanent and irreversible, or temporary and reversible. The performance loss of some poisoning species can be negated by simply ending introduction of the impurity or by performing a recovery procedure. Additionally, one cannot state if an effect is permanent unless rigorous procedures have been attempted. Exposure to high potentials or repeated cyclic voltammetry (CV) sweeps and operation at high currents should be performed to determine if the effects are permanent.

While the effects of one impurity (CO) have been thoroughly researched, there are fewer publications investigating the effect of other impurities on fuel cell performance.[37-50] **Table 1-2** lists the most common impurities and their sources. CO, NH_3, H_2S, HCN, hydrocarbons, aldehydes, and mercaptans are common impurities exist in hydrogen fuel.[51] The trace impurities can have a larger impact on performance and durability than either N_2 or CO_2 even though the concentrations of these species are typically 4 orders of magnitude lower. The best-known, and well-studied example of an anode catalyst poison is carbon monoxide.[37, 51-59] CO forms a strong bond with Pt, chemisorbing on the metal surface. The chemisorbed CO blocks the adsorption of hydrogen onto active Pt sites for HOR. This catalyst poisoning reduces electro-oxidation rates and raises electrode overpotentials, resulting in performance losses compared to CO-free tests. Fortunately, the durability implications of long-term exposure to CO-containing streams appeared to be similar to those of fuel cells without CO.

The presence of ammonia levels as low as 13 ppm in the fuel stream has rapid deleterious effects on performance.[47] Higher concentrations (80, 200, and 500 ppm) of NH_3 have shown a marked decrease in performance in simulated reformate: cell performance decreases with exposure to NH_3 in reformate from 825 to 200 mA/cm^2 at 0.6 V.38 Short-term exposure (<1 h) to NH_3 shows reversible effects.[47] However, the negative effects caused by long-term exposure are irreversible, meaning that further operation on neat H_2 results only in a partial recovery. the degradation mechanism appears to be due to protonic conductivity loss. The likely culprit is that NH_3 reacts with ionomeric H^+, generating NH^{4+} and consequently lowering the protonic activity. The negative effect gradually starts at the anode catalyst layer, the first region exposed, and continues into the membrane as the ammonia diffuses deeper and deeper.

Large amounts of H_2S (up to several vol %) may exist in natural gas and other fuels from fossil origin. Pt catalysts have a strong chemical affinity with H_2S. The degrading effects of the presence of this impurity in the FC are significant and commensurate with H_2S concentration and time of exposure. The electrochemical desorption of sulfur requires potentials unachievable in a continuously operating H_2/air fuel cell. 10 ppb of H_2S has been shown during long operating times to have a degrading effect on fuel cell performance.[45]

Hydrocarbon impurities tend to be ubiquitous from reforming reactions, with methane being the most common, as the equilibrium level of methane during reforming reactions is normally 0.1-1.0%.[60] Methane, as an impurity, is known to have no poisoning effect, as many stationary systems operate from reformed natural gas and contain methane. Other hydrocarbons, such as benzene and toluene, did not show evidence of fuel cell degradation upon exposure on the anode, although toluene hydrogenation occurs in the

anode, resulting in 90% conversion of the toluene to methylcyclohexane.[47] However, benzene was noted to "smother" the cell with exposure on the cathode.

The air side of the fuel cell is exposed to air pollutants that can vary tremendously in concentration. Research has concentrated on commonly occurring air pollutants and aerosols. The work performed to date on cathode impurities includes oxides of sulfur and nitrogen, hydrocarbons, ozone, particulates, and aerosol salts.

Sulfur dioxide is a common air contaminant resulting from fossil fuel combustion and can be found in high concentrations in urban areas with heavy traffic and in close proximity to some chemical plants. The effects of SO_2 injected at the cathode are similar to those produced by the presence of H_2S in the anode.[51] Performance degradation appears to be a function of SO_2 concentration in the bulk, as the performance decrease was measured to be 53% at 2.5 ppm SO_2 as compared to a 78% decrease at 5 ppm SO_2 for the same applied dosage.[42] Performance does not improve after impurity injection is turned off; thus, is not reversible just by normal operation.[30, 51] The severity of the effect is due to the strong chemisorption of SO_2 (or other S-species) onto the Pt catalyst surface. Electrochemical oxidation (during a CV) of adsorbed SO_2 shows full cell performance recovery. Nitrogen oxides (NO*x*) are air contaminants that mostly originate in the combustion of fossil fuels. Internal combustion engine emissions are the major source of NO*x*; thus, they are abundant in urban areas.

NO_2 has been shown to quickly degrade fuel cell performance,[42, 51] with a gradual decrease over 30 h of operation, after which degradation did not continue.[51] The rate of poisoning of PEMFCs by NO_2 does not strongly depend on NO_2 bulk concentration. The degradation of performance of the fuel cell can reach 50%, while the cell performance

completely recovers after applying neat air for 24 h.[42] The poisoning effects of NO_2 do not appear to be a catalyst poisoning issue, since no surface species can be detected during cyclic voltammetry;[42, 51] the poisoning mechanism is still not understood.

Table 1-2. Origin of common fuel and air impurities.[51]

Hydrogen Fuel Impurities	
Fuel for hydrogen	Potential impurities
Crude oil: gasolines diesels	CO, NH_3, H_2S, HCN hydrocarbons, aldehydes mercaptans
Natural gas	CO, NH_3, H_2S, HCN, hydrocarbons, mercaptans
Methanol/DME	CO, odorants, alcohols
BioMass	cations, aldehydes, alcohols, formic acid, NH_3, H_2S, HCN
Water electrolysis	anion, cations
Air impurities	
Fuel combustion pollution	SO_x, NO_x, hydrocarbons, soots and particulates
Ambient air, farming	NH_3
Natural sources	Ocean salts, dust
others	
de-icers	NaCl, $CaCl_2$
FC system corrosion products	cations, anions

In addition to gas-phase contaminants, salts (principally from ocean mists and road deicer) may contaminate the cathode air supply. The presence of NaCl at the electrode decreases its performance. The performance loss is mostly due to a decrease of protonic conductivity as a consequence of exchange of H^+ by Na^+ at the catalyst layer and at the

membrane. Large concentrations of the salt also decreased the hydrophobicity of the gas diffusion layer, increased liquid water retention, and correspondingly decreased oxygen transport to the electrocatalyst at high current densities. Surprisingly, Cl^- does not appear to block adsorption on the catalyst surfaces, as revealed by CV measurements.[51] However, chloride has a dramatic effect on the oxygen reduction kinetics of cathode electrocatalysts. Chloride has also been noted to affect GDL materials, which can lead to changes in water and gas transport.

1.4.3.2 Fuel Starvation

Full-sized cells, on the order of several hundred square centimeters in area, will experience different conditions between the inlet and the outlet, and this can lead to current distributions that cannot easily be simulated in subscale testing. Furthermore, cells arranged in a stack configuration can experience different flows of fuel, air, and coolant resulting from imperfect manifolding. Therefore, adjacent cells in a stack can experience different conditions in terms of hydrogen and oxygen content, but they will be forced to carry the same current as their neighboring cells, as they are connected in series.

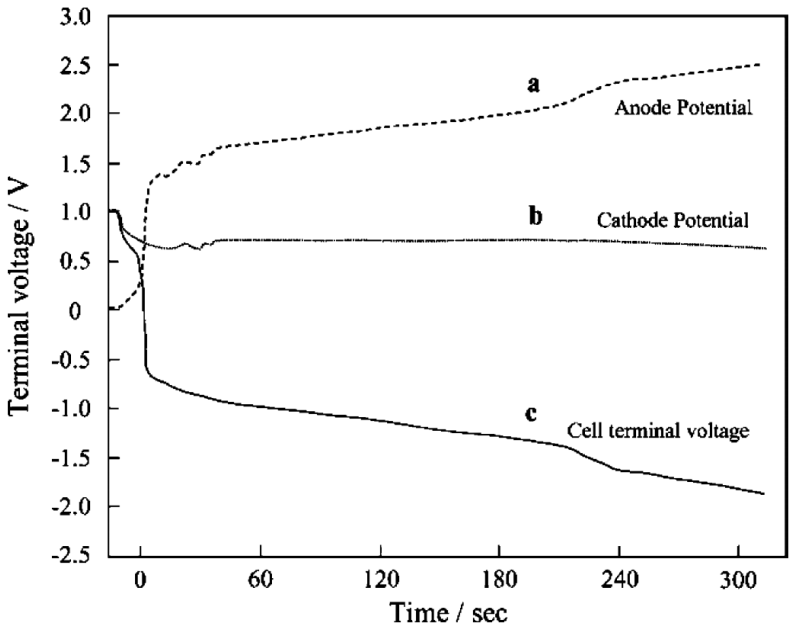

Figure 1-8. Electrode potentials for a cell driven to pass current after hydrogen flow is interrupted.

Several authors have noted that, in the case of gross fuel starvation, cell voltages can become negative, as the anode is elevated to positive potentials and the carbon is consumed instead of the absent fuel.[61-63] In the case of gross fuel starvation, for multiple cells in a stack, fuel maldistributions can lead to some cells having insufficient fuel to carry the current that is being pushed through them by adjacent cells. In the absence of a sufficient anodic current source from hydrogen, the cell potential climbs higher until oxidation occurs in this case, the oxidation of the carbon support of the catalyst layer. A diagram illustrating the change of electrode potentials under starvation conditions is shown in **Figure 1-8**.

For reversals of this type, the anodic current is generally provided by carbon corrosion to form carbon dioxide, and results in permanent damage to the anode catalyst

layer. Modeling has been conducted to describe how a poor hydrogen distribution can induce both O evolution and carbon corrosion at the cathode of the fuel cell.[64] Modeling has also predicted that O_2 crossover through the membrane controls the total amount of current that goes to carbon corrosion.[65] These issues have led to the conclusion that conventional carbon supports for Pt are unlikely to meet automotive durability targets and implementation of corrosion-resistant supports combined with controlled system strategies are required.[66] Proper reactant distribution is critical to avoid this problem, and stack developers have accordingly sought to monitor the voltage of each cell to avoid such a problem.[67] Obviously, such an extensive monitoring system will add considerable cost and complexity to the fuel cell stack and control scheme.

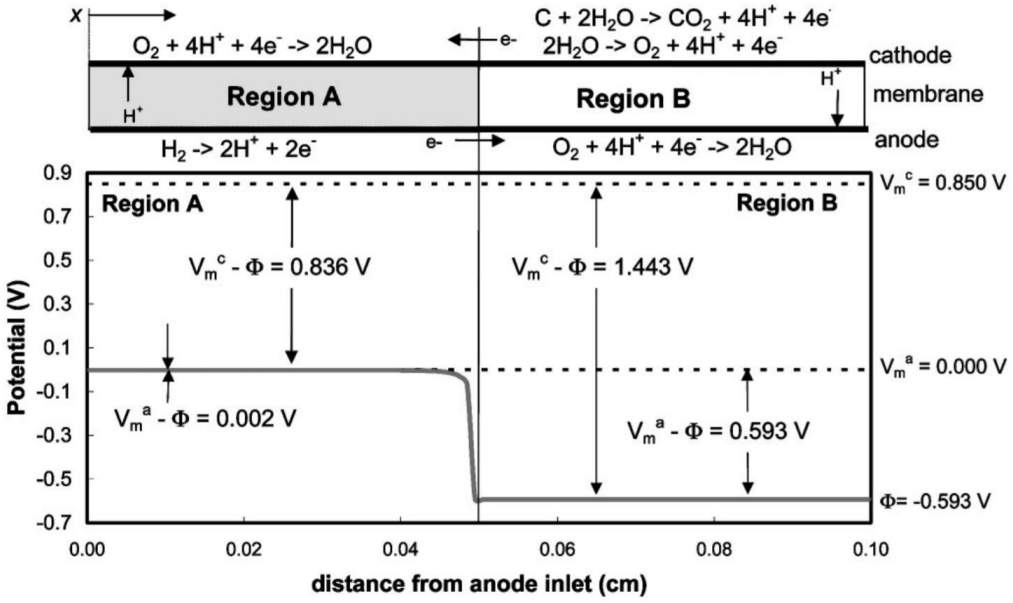

Figure 1-9. Schematic diagram illustrating the "reverse current" mechanism.

A subtler form of fuel starvation was proposed in a paper by Reiser *et al*.[68] They suggest that transient conditions, or *localized* fuel starvation, can induce local potentials on

the air electrode significantly higher than 1 V and, thereby, induce corrosion of the carbon supports that results in permanent loss of electrochemically active area. The cell potential can remain in the range of expected conditions even as this condition persists, and this "reverse" current mechanism can induce damage to the cathode without being directly observable.

The mechanism suggests that the highly conductive bipolar plates of the fuel cell allow for sufficient redistribution of current in the plane of the current collectors that all regions of the cell experience the same potential difference. In the regions of the cell where fuel is present on the anode, the fuel cell behaves normally; the fact that the hydrogen reaction is so facile implies that the potential in the fuel-rich regions will stay close to its equilibrium voltage and is capable of delivering high currents until the hydrogen is consumed. In the regions of the cell where there is no fuel present, there is no proton or electron source at lower potentials, so the electrodes must shift to significantly higher potentials to maintain the potential difference imposed by the active part of the cell while still conserving current. Thus, a reverse current is established, and current is driven from the positive electrode to the negative electrode in the fuel-starved region, opposite the direction of normal current flow in the active portion of the cell. The only reactions that can sustain this current in the fuel-starved region are oxygen evolution and carbon corrosion on the positive electrode, and oxygen reduction from crossover on the negative electrode. This mechanism is shown schematically in **Figure 1-9**. This problem can be induced not only by poor cell-to-cell flow distributions but also by local blockages, by differences in channel depth tolerances, and by water blockage, if water vapor condenses in the anode channels and fills the channels. A good example of this is given by Patterson

and Darling.[69] This phenomenon has been visualized by neutron imaging and suggests that improper water management can cause major problems with fuel distribution and, consequently, damage to the cathode catalyst layers.[70]

1.4.3.3 Load Cycling

A fuel cell, particularly one that must meet the challenging dynamic load of an automotive application, will undergo many rapid changes in load over the course of its lifetime. As the fuel cell cycles from high to low current, its cell potential will also vary, generally between 0.6 and 1.0 V. For cells operating with relatively pure hydrogen as a fuel, the anode will stay fairly close to the reversible hydrogen potential, due to the facile nature of the hydrogen oxidation reaction.[71]138 This implies that the cathode experiences potential swings as cell potential changes to match variable power demands. The variation of the cathode potential will change several properties of the electrode materials, notably the degree of oxide coverage of both platinum and carbon, and the hydrophobicity of the surfaces.

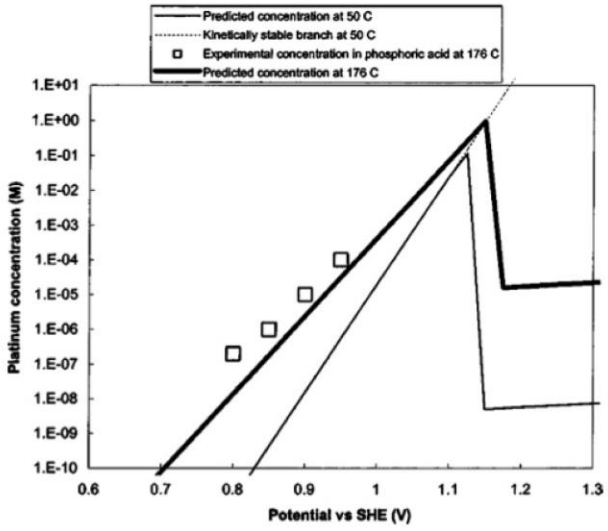

Figure 1-10. Equilibrium concentration of dissolved platinum vs electrode potential from a mathematical model.

A subtler distinction has to do with the fact that the oxide can actually serve to protect the platinum surface from dissolution at higher potentials. When the cathode potential rises rapidly to higher values, the platinum can dissolve at a rapid rate until a passivating oxide layer is formed. Patterson presented data on the rapid loss of electrochemically active area with potential cycling, and the phenomenon was subsequently modeled by Darling and Meyers, using simple models to describe the rates of platinum dissolution and of oxide formation and their subsequent movement through the cell.[72-73] Their model predicts that platinum is fairly stable at both low and high potentials, but there is a kinetically stable branch where platinum will dissolve rapidly when transitioning from low to high potentials. This is shown schematically in **Figure 1-10**. The general trend of platinum solubility was subsequently measured in liquid electrolytes, and the same trend was discovered, although the equilibrium concentrations differed greatly from the model behavior proposed.[74-75] These results are shown in **Figure 1-11**.[75]

To develop stable catalysts for fuel cell applications, the stability of the catalysts not only under constant potential conditions but also under potential cycling must be considered. Much more information, such as the nature of the oxide, the kinetics of its formation, and its ability to protect the catalyst from dissolution over the entire range of potentials, is needed to design catalysts that are robust to this degradation mode.

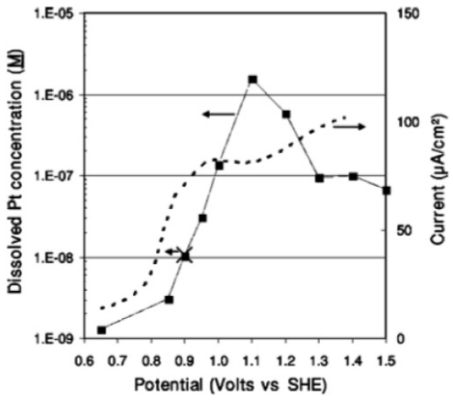

Figure 1-11. Measured dissolved platinum concentration in solution and initial dissolution rates in 0.57 M perchloric acid.[75]

1.4.3.4 Start/stop Cycling

Although the influence of localized starvation under normal operation can be mitigated to some extent through careful control of reactants and water management (design, operating conditions, and materials choices), maldistributions of fuel and current must be almost certainly inevitable during fuel cell operation of start-up and shutdown. Under conditions of a prolonged shutdown, unless the stack is continually provided with fuel, the anode chamber will eventually empty due to hydrogen crossover from the anode to the cathode, and result in an air-filled flow channel. In this case, when the stack start up next time, the starting flow of fuel will induce a transient condition in which fuel exists at the inlet but the exit is still fuel-starved. As a result, starting and stopping the fuel cell can induce considerable damage to the cell. This phenomenon has been modeled and reveals that an unprotected start can induce local potentials on the cathode in excess of 1.8 V relative to a hydrogen reference electrode.[64] This modeling study suggests that potential control (voltage clipping) is by far the most effective means of minimizing this effect. A

review of system-level strategies to minimize this mode of degradation has been reported by Perry *et al.*.[76]

1.5 The current state of the arts of PEM fuel cells for automotive applications

Fuel cell is one of the most promising technologies for the next generation of power supply using in automotive vehicles. Current fuel cell technologies, however, are limited by cost and fuel supply, as well as the inability to respond to fluctuations associated with operation conditions, fuel supply, and transient load. For the automobiles using fuel cell as the power system, hybrid strategies have been built to achieve high fuel efficiency and high-power output. Batteries or capacitors are always integrated with the fuel cell. The energy storage elements would supplement the fuel cell when the power demand exceeded the power delivered by the fuel cell. However, the design of the energy management program for the hybrid electric system is very complicated due to the complexity of the hybrid system. Moreover, the energy storage devices occupy the limited room in the vehicle and also increase the cost.

Materials with higher capacitance, e.g., metal hydrides and manganese oxide, have been integrated within the anodes and cathodes of alkaline fuel cells, respectively, affording the devices with battery-like response capability. However, metal hydrides and manganese-oxide-like oxides are unstable in acidic electrolytes. Similarly, although V_2O_5 with high capacitance was used as an energy-storage material in SOFCs to afford the response function, vanadium oxides are unstable in acidic or basic electrolytes. Hydrate RuO_2 exhibits high capacitance (> 700 F/g), electron conductivity, proton conductivity and catalytic activity, and also chemically stable in acidic environment, but it is too expensive.

1.6 Material selection criteria and design principles

To develop effective energy-storage materials applying in the fuel cell application, it is important to follow the essential characteristics of fuel cells, which rely on chemical transformations accompanied by synergic translocations of electrons and ions (e.g., protons) between the anodes and cathodes. The effectiveness of the transformation process is generally governed by transport of fuels (in fuel cells), kinetics of electrochemical reactions, and transport of ions and electrons. In this context, in addition to long-cycling stability and high storage capacity, the electrodes should possess:

(1) High stability in electrolyte. The prerequisite for the application of metal oxides in electrochemical devices is that metal oxides cannot dissolve in electrolyte. For example, titanium oxide, tungsten oxide, molybdenum oxide and ruthenium oxide, *etc.* are stable in acidic media, while manganese oxide and perovskite oxides are stable in alkaline media. However, some amphoteric metal oxides such as Al_2O_3, V_2O_5 and ZnO cannot be used in both media, while many alkaline metal oxides such as MgO, CaO and CuO should be avoided in acidic media.

(2) High resistance against electrochemical corrosion: metal oxides should be electrochemically stable under the working conditions, or metal nanoparticles supported on them will peel off from them and agglomerate, leading to the degradation of catalytic performance.

(3) Good electronic conductivity. Doping of other metal ions can increase the conductivity of an insulating oxide, while mixing with carbon black or carbon nanotubes (CNT) to form oxide–carbon nanocomposites can improve their electronic conductivity markedly.

(4) Good proton conductivity.

(5) High specific surface area

1.7 Research Objective

The goal is to develop a high-performance energy-storage material, as well as the integration of such materials as electrodes to afford fuel cells with a dynamic response function. Towards these goals, two major tasks will be executed:

Task 1: Development of energy-storage materials for PEM fuel cells: Materials with different structures and compositions will be synthesized. Systematic studies will be conducted to relate the structure and composition to proton conductivity, electron conductivity, and energy-storage performance (storage capacity, power performance, and cycling stability). This obtained knowledge will then be utilized to guide our material design and synthesis, leading to optimized energy-storage performance.

Task II: Design and Fabrication of Membrane Electrolyte Assemblies (MEA). Electrodes, MEA, and single cell will be fabricated and tested. Electrodes will be fabricated and tested for catalytic activity and electrochemical performance; charge and discharge capability of MEA and the capability to respond to fluctuations will also be tested. Finally, fuel cells will be assembled to construct a prototype device with a response function.

Task III: The mechanism of PEM fuel cell degradation and the fundamental working principle of the hybrid cell will be studied. The voltage of the cell or the potential of the anode will be recorded during the transient operations to analyze the function of WO_3 layer. The *ex-situ* experiments such like H_2 pump test and rotating disk test will be conducted as well.

Chapter 2. Synthesis and Characterization of Tungsten Oxide for Energy Storage

2.1 Introduction

Only a handful of materials with meaningful capacitance are known to be acid-stable, mainly including conductive polymers and transition-metal oxides, such as WO_3, RuO_2, and PbO_2. Conductive polymers are generally unstable at elevated temperatures; PbO_2 is acid-stable, while electrochemical reduction converts the PbO_2 into soluble species in acid (or insoluble $PbSO_4$ in lead-acid batteries). Hydrate RuO_2 exhibits high capacitance (> 700 F/g), electron conductivity, proton conductivity and catalytic activity, but it is too expensive.7 Although Mo-based oxides may exhibit a bronze structure similar to WO_3, such materials are less acid-stable with low energy-storage capacity. To the best of our knowledge, WO_3 is the only candidate that may be used for energy storage in PEM fuel cells, but it has not yet been explored.

WO_3 has been one of the most extensively studied materials for electrochromic devices, information displays, sensor devices and smart windows. In addition, WO_3 has a high potential for the use in electrochemical devices. WO_3 is a transition metal oxide with wide-ranging applications. Interest in WO_3 can be dated back to the 17th century when the properties of $LiWO_3$ and the techniques for the synthesis of WO_3 and $NaWO_3$ were first studied.

WO_3 crystals are generally formed by corner and edge sharing of WO_6 octahedra. The following phases are obtained by corner sharing: monoclinic, orthorhombic, tetragonal, and cubic WO_3. In addition to the aforementioned crystal phases, another vital phase for WO_3 is hexagonal (*h*-WO_3). Observation of this phase was first reported by Gerand et al.

in 1979 and was originally obtained from the slow dehydration of tungstite. **Figure 2-1** presents a diagram of the crystal structure of *h*-WO_3. The crystal is again obtained from WO_6 octahedra, but with the form of three- and six- membered rings in the a, b-plane. These three- and six-membered rings result in the appearance of trigonal cavities and hexagonal windows, respectively. In the c-axis, these octahedra stack by sharing the axial oxygen and form 4-coordinated square windows. The lattice constants reported for *h*-WO_3 are a =7.298 Å and c =3.899 Å.[77]

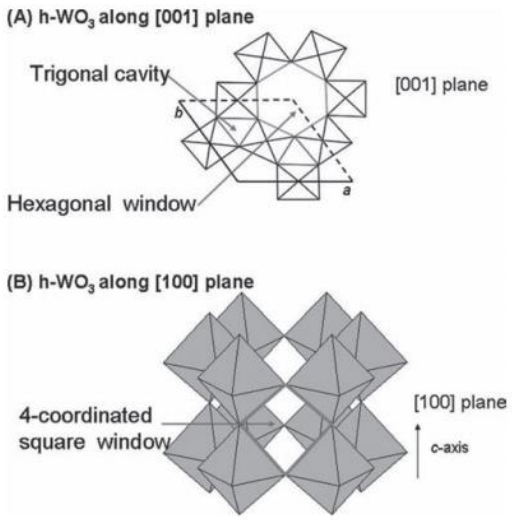

Figure 2-1. (A) The structure of h-WO_3 is shown with the c-axis perpendicular to the plane; (B) The structure of *h*-WO_3 with the c-axis parallel to the plane.

WO_3 is an n-type semiconductor with high electronic resistance (~10^{-5} S/cm), and non-stoichiometric oxides are electronic conductive, attributable to their oxygen-vacancy defects (e.g., $WO_{2.75}$ exhibits electronic conductivity as high as 10 S/cm). [78] In the presence of Pt and hydrogen, WO_3 can be readily reduced to non-stoichiometric oxides at room temperature.[79] Mesoporous WO_3 with a high surface area (140 m^2/g) and high electronic conductivity (~ as high as 20 S/cm) were also reported.[80-82] Hydrous tungsten oxides

($WO_3 \cdot nH_2O$) show considerable proton conductivity. For example, layered $WO_3 \cdot 2H_2O$ exhibits proton conductivity of 0.15 mS/cm and 7 mS/cm, respectively, at 25 °C and 150 °C under saturating water pressure, but rapidly drops to 0.1 mS/cm at 20% water saturating pressure at 110 °C. [83]

WO_3 can undergo a reversible redox reaction,

$$WO_3 + xH^+ + xe^- \leftrightarrow H_xWO_3$$

forming electron-conducting hydrogen tungsten bronze, H_xWO_3.[84] Based on a single-electron reaction, the theoretical capacity of WO_3 is estimated to be 115 mAh/g. WO_3 thin films,[85] mesoporous WO_3,[86] and WO_3/carbon composites,[87] mainly with monoclinic and orthorhombic structures, have been explored for energy storage in acid electrolytes, but with low capacity (< 70 mAh/g) and slow rate performance; this poor performance is probably due to their low proton conductivity and the resulting sluggish electrode kinetics.[88]

WO_3 has been extensively explored as a fuel cell co-catalyst with enhanced activity and tolerance for CO poisoning.[84] Pt-WO_3 exhibits higher activity than Pt for hydrogen and methanol oxidation reactions. An activity trend of Pt-Ru-WO_3 > Pt-Ru > Pt-WO_3 > Pt was also observed in ethanol oxidation reactions. [84] WO_3 was also explored as a fuel cell catalyst support, exhibiting much improved stability compared to Vulcan XC-72R.[89]

The promotional effect of WO_3 was attributed to several aspects:

(1) Uniform dispersion of noble metal nanoparticles on WO_3. This depends to some extent on the different preparation methods. (2) “Hydrogen spillover effect”. This means the formation of hydrogen tungsten bronze and the subsequent oxidation of hydrogen on hydrogen tungsten bronze, which ensures that the Pt active sites can function more

efficiently as a dehydrogenation catalyst and that poisons are more readily desorbed from the catalyst surface. (3) A strong resistance to poisoning by intermediates such as CO. The presence of WO_3 could lead to the easy formation of adsorbed water or OH_{ad} and thus effectively oxidize the intermediate poisons.

Since then, various tungsten oxides have been synthesized using various preparation methods and used in various fuel cell applications such as HOR, MOR, EOR, FAOR and ORR.

The tungsten bronzes, M_xWO_3, where M is any one of several metals, and $0<x<1$, possess all the characteristics of a potential electrocatalyst for acidic fuel cells. They are acid stable, electrically conductive, and can exist with a variation in oxygen stoichiometry, indicating that they can gain and lose oxygen readily. In the decades 1960s and 1970s, research focused on M_xWO_3 for their possible use as electrode materials for the oxygen reaction reduction (ORR) and hydrogen oxidation reaction (HOR) in fuel cells, and the results were conflicting. M_xWO_3 (M=Na, K, Ba, Pb, Tl, U, Cd) served as catalysts for the ORR, although they were inactive as anode catalysts. These systems probably can exist with a wide variation in oxygen content. They therefore can readily adsorb oxygen and lose it to the solution after it has been reduced.

2.1.1 Synthesis of WO_3 with different crystal structure

Many different approaches for the synthesis of nanostructured WO_x have been implemented using both vapor- and liquid-phase-based methods. Hydrothermal treatment is a facile, cost-effective and well-studied liquid-phase technique, which has the capability of producing WO_x of different nanomorphologies. In most cases, the hydrothermal synthesis of nanostructured WO_x starts with the preparation of a tungstic acid solution

(H_2WO_4) as the precursor. This solution is then kept at an elevated temperature (120–300 °C) for a certain period of time, allowing the nucleation and growth of crystallites. The precipitation of WO_3 from a tungstate ion solution using concentrated acid is a well-known synthetic route described as follows[77]:

$$WO_4^{2-} + 2H^+ + nH_2O \leftrightarrow H_2WO_4 \cdot nH_2O$$

$$H_2WO_4 \cdot nH_2O \leftrightarrow WO_3 + (n+1)\ H_2O$$

Crystal structure and hydrate state of $WO_3 \cdot nH_2O$ are key factors that affect their proton-electron conductivity and energy-storage performance. WO_3 with different structures (e.g., hexagonal, monoclinic, and orthorhombic structure) and hydrate states (e.g., $WO_3 \cdot nH_2O$, $0.3<n<2$) will be synthesized. Briefly, sodium tungstate and capping agent ($(NH_4)_2SO_4$, Na_2SO_4) will be dissolved in DI water, followed by the addition of acid (e.g., H_2SO_4 solution) to adjust the solution pH in the range of 0 to 3. The mixtures will be subjected to hydrothermal treatments at different temperatures (e.g., 90 to 200 °C) and times (e.g., hours to days).

Ions (Na^+, K^+, and NH_4^+) play significant roles in controlling the crystal structure of the formed WO_3 products. For example, Na^+ and NH^{4+} lead to the formation of $WO_3 \cdot nH_2O$ with orthorhombic and hexagonal structures, respectively. A series of experiments will be done to reveal how capping agents influence the crystal structure and morphology of WO_3 nanoparticle.

Reaction time and pH can significantly affect water content (n) in $WO_3 \cdot nH_2O$. As-synthesized $WO_3 \cdot nH_2O$ will be subjected to extensive characterization, such as electron microscopy (crystal morphology and structure), nitrogen adsorption-desorption (pore structure and surface area), XRD (crystalline structure), and TGA (water content).

2.1.2 Synthesis of h-WO_3 with controlled morphology and nanostructure

The hexagonal tungsten trioxide (*h*-WO_3) has attracted much interest because of its unique tunnel structure.[90] It is well known that one-dimensional (1D) nanoscaled materials, such as nanotubes, nanowires and nanorods, have attracted intensive interest due to their novel physical properties and potential wide-field applications. The synthesis of 1D nanostructures and their assembly into ordered superstructures or multifunctional architectures offer great opportunities for exploring their novel properties and, furthermore, fabricating nanodevices.[91]

The different morphologies and nanostructures of *h*-WO_3 can be selectively fabricated by varying the experimental parameters under hydrothermal conditions, such as the pH value of solution, different capping agents, and the concentration of ions. The urchinlike and nanoplates *h*-WO_3 can be synthesized in the presence of Rb_2SO_4.[92] When the concentration of Rb_2SO_4 is low, urchinlike product can be obtained, while the nanoplates would emerge when the amount of Rb_2SO_4 increase.[92] The ribbonlike assemblies of *h*-WO_3 can be selectively prepared in the presence of K_2SO_4.[92] Nanorods can be synthesized in the presence of NaCl[93-94], Na_2SO_4[91] or $(NH_4)_2SO_4$[94-95] when precisely adjust the solution to certain pH value.

In this experiment, Na_2SO_4 and $(NH_4)_2SO_4$ will be chosen as capping agent to prepare *h*-WO_3 nanorods. The concentration of capping agent, pH value of solution, reaction temperature and time will be optimized to obtain *h*-WO_3 nanorod with appropriate diameter and length.

2.2 Synthesis and characterize of WO_3 with controlled crystalline structure

WO_3 is known as a polymorphous material that exists as a function of temperature, as triclinic, monoclinic, orthorhombic and tetragonal forms, as well as the metastable phases of hexagonal and cubic. Compared with the metastable forms, WO_3 with monoclinic and other crystalline phases are more stable at high temperature, making it sense to synthesize WO_3 with different phases for fuel cells operated at different temperatures. In this study, WO_3 with monoclinic, orthorhombic, hexagonal, or cubic phases were synthesized via hydrothermal method.

2.2.1 Structure and Morphology Characterization

Figure 2-2 shows the XRD patterns of the as-prepared samples, confirming the successful synthesis of the WO_3 with hexagonal (PDF#33-1387), orthorhombic (PDF#54-1012), monoclinic (PDF#43-1035), and cubic (PDF#44-0363) structure. The XRD pattern of the orthorhombic phase is very similar to that of the hexagonal phase, except for the diffraction peak at 18.0^o which is typical of the orthorhombic phase. In comparison with other WO_3 samples, the intensity of peaks of the hexagonal WO_3 prepared with Na+ is much stronger, which indicates higher crystallinity and larger particle size. For the synthesis of WO_3 with cubic structure, however, as-synthesized sample contains a component of hexagonal structure. The diffraction peaks at 15.0, 29.0, 30.3, 35.1, 38.4, and 46.1^o are in concordance with the (111), (311), (211), (400), (331), and (511) lattice planes of the cubic WO_3, respectively.

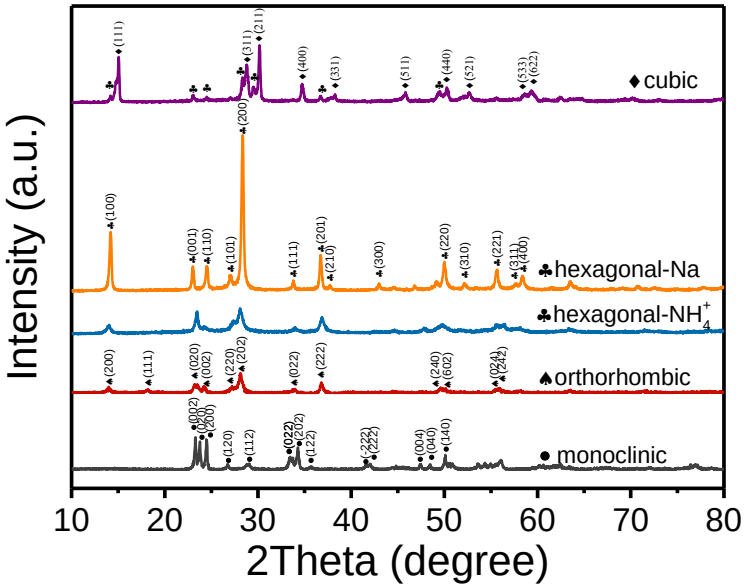

Figure 2-2. XRD patterns of the as-prepared WO_3 samples with monoclinic, orthorhombic, hexagonal or cubic phase.

It is well known that the crystalline structures of WO_3 hydrates are highly related to their water content. TGA measurements were conducted for each sample to determine the water content of each WO_3 hydrate. **Figure 2-3** shows TGA profiles of these samples, suggesting the weight loss of these samples is generally occurs at temperature below 400 °C. It is believed that such weight lost is mainly due to removal of the H_2O within the crystals, therefore, the composition of the water within these samples are calculated based on the weight lost and labeled accordingly. As expected, WO_3 with hexagonal or cubic phase contain more water than those with other structures, because such hexagonal and cubic structure can accommodate more water molecules within their 1D or 3D channels, which are formed from octahedral WO_3 building blocks.

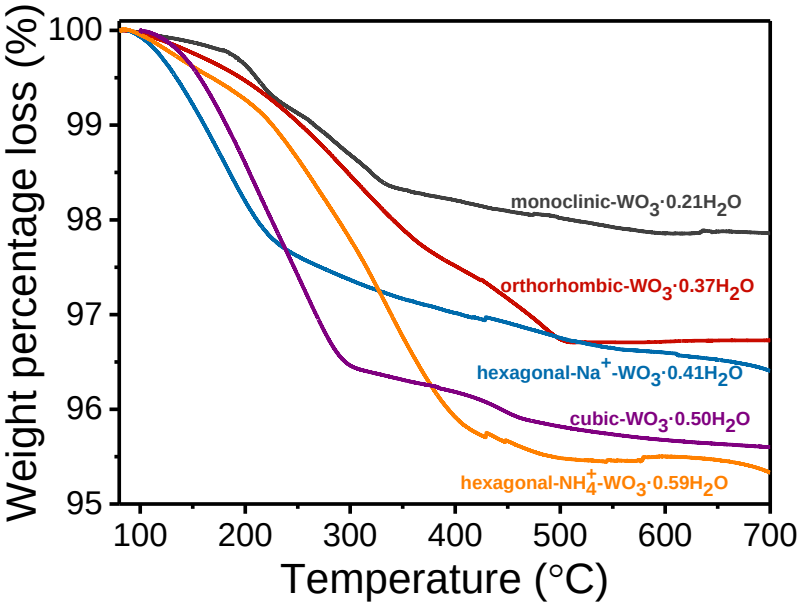

Figure 2-3. TGA profiles of the as-prepared WO_3 samples with monoclinic, orthorhombic, hexagonal or cubic phase and their water content.

Figure 2-4 shows SEM images of the as-prepared samples. The hexagonal WO_3, made with Na^+ or NH_4^+, exhibit a nanorod shape, which indicates a preferred growth of the WO_3 along the *c*-aix. The preferable growth may due to the presence of Na^+ or NH_4^+ cations and the counter ions, such as SO_4^{2-}, which requires further studies. The nanorods made from Na^+ show length ~ 1-2 μm and diameter ~ 200 nm, while those made from NH_4^+ show much shorter length (300-400nm) and smaller diameter. It's consistent with the results of XRD tests. The difference may be attributed to the different electrostatic interactions and size of the cations. For comparison, the cubic phase WO_3 exhibit a particle shape accompanied by the hexagonal WO_3 nanorods. Both the orthorhombic and monoclinic WO_3 show particular shape with well-developed morphology. Particularly, the monoclinic

ones show well-developed crystal edges and corners, indicating better developed crystalline structure.

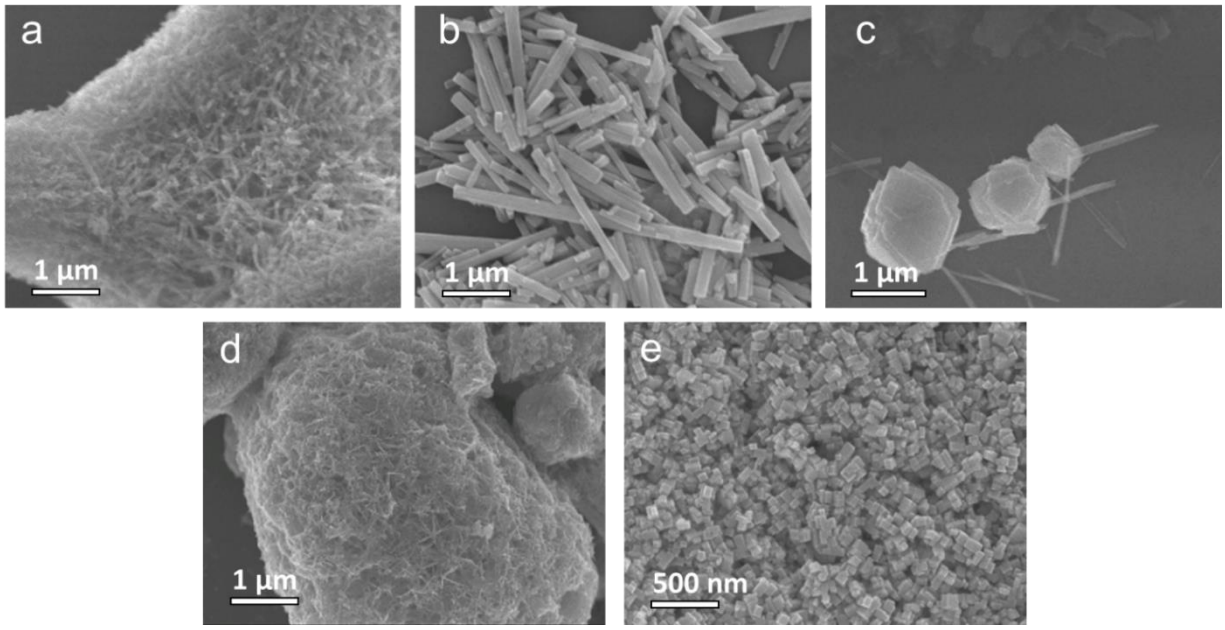

Figure 2-4. SEM images of (a) hexagonal WO_3 with NH_4^+, (b) hexagonal WO_3 with Na^+, (c) cubic WO_3, (d) orthorhombic WO_3, and (e) monoclinic WO_3.

2.2.2 Thermal Stability and Electrochemical Storage Capability

The as-synthesized WO_3 samples were then heated in air up to 500 °C and subjected to further XRD studies to examine crystal structure. These samples, with and without the heat treatments, were also subjected to electrochemical tests, to examine their electrochemical energy storage capability. These studies will provide the necessary knowledge of the thermal stability of the WO_3 samples. The cubic WO_3 was excluded due to impurity.

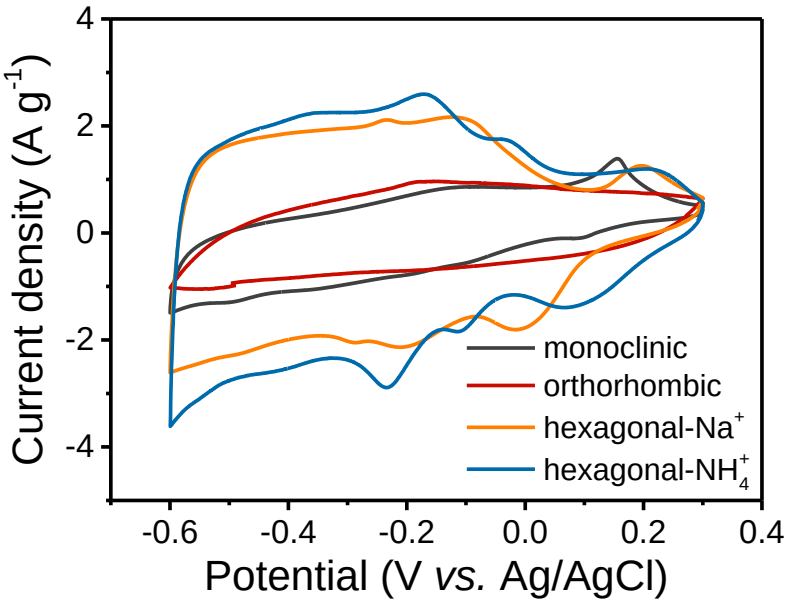

Figure 2-5. Cyclic voltammogram (CV) curves tested at 5 mV/s of fresh WO_3 samples in different crystal structures

Cyclic voltammograms of fresh WO_3 samples in different crystal structures measured at 5 mV/s are shown in **Figure 2-5**. Two hexagonal WO_3 samples show typical pseudo-capacitive behavior. Two pairs of well-defined redox peaks account for the reversible proton insertion into the WO_3 crystals from surface sites and through channels. The positions of the redox peaks on two hexagonal WO_3 are not conformity which due to differences in particle size and morphology of the two samples. Redox peaks are observed for the cubic WO_3 as well. Since there is impurity of hexagonal WO_3 inside the cubic WO_3 sample, the redox peaks may be related to the redox reaction of hexagonal WO_3. The sharp cathodic peak at -0.6 V is related to the H_2 evolution reaction occurs on the cubic phase WO_3. For monoclinic and orthorhombic WO_3, there is no apparent redox peak and only little capacitance is shown in the figure, indicating poor pseudo-capacitance of these two

phases. Capacities calculated from the voltammograms of these five WO_3 samples are 33, 32, 95, and 86 mAh/g for monoclinic, orthorhombic, hexagonal prepared with NH_4^+, and Na^+ phase respectively. The thermal stability and the electrochemical performance after heat treatment for each WO_3 phase are introduced in the following.

1. WO_3 with hexagonal structure

Figure 2-6(a) shows XRD of hexagonal WO_3 synthesized using NH_4^+ ions as the templates under heat treatment at 200 °C, 300 °C, 400 °C, and 500 °C for 4 hours It is clearly that the hexagonal structure is stable up to 300 °C. The phase translation from hexagonal to monoclinic comes up at 400 °C, which several characteristic diffraction peaks of monoclinic phase can be observed in the XRD patterns of the sample treated at 400 °C. Further increasing the temperature converts the hexagonal structure into a monoclinic phase entirely.

Electrochemical tests suggest that these samples exhibit typical CV curves of hexagonal WO_3, only the 400 °C treated sample shows decreasing capacitance due to the phase transition (**Figure 2-6**(b)). The electro-storage capacity and the rate performance of samples were measured by charge-discharge tests. In conformity with CV results, the capacitances of samples treated at 200 and 300 °C are similar with the fresh sample, which are about 80 mAh/g, at low charging/discharging rate (5 A/g). In **Figure 2-6**(c), the calcined samples show superior rate performance than the fresh sample, more than 50 mAh/g capacity persists at fast charging/discharging rate of 20 A/g. In the other hand, the storage capacity of the sample treated at 400 °C drops dramatically.

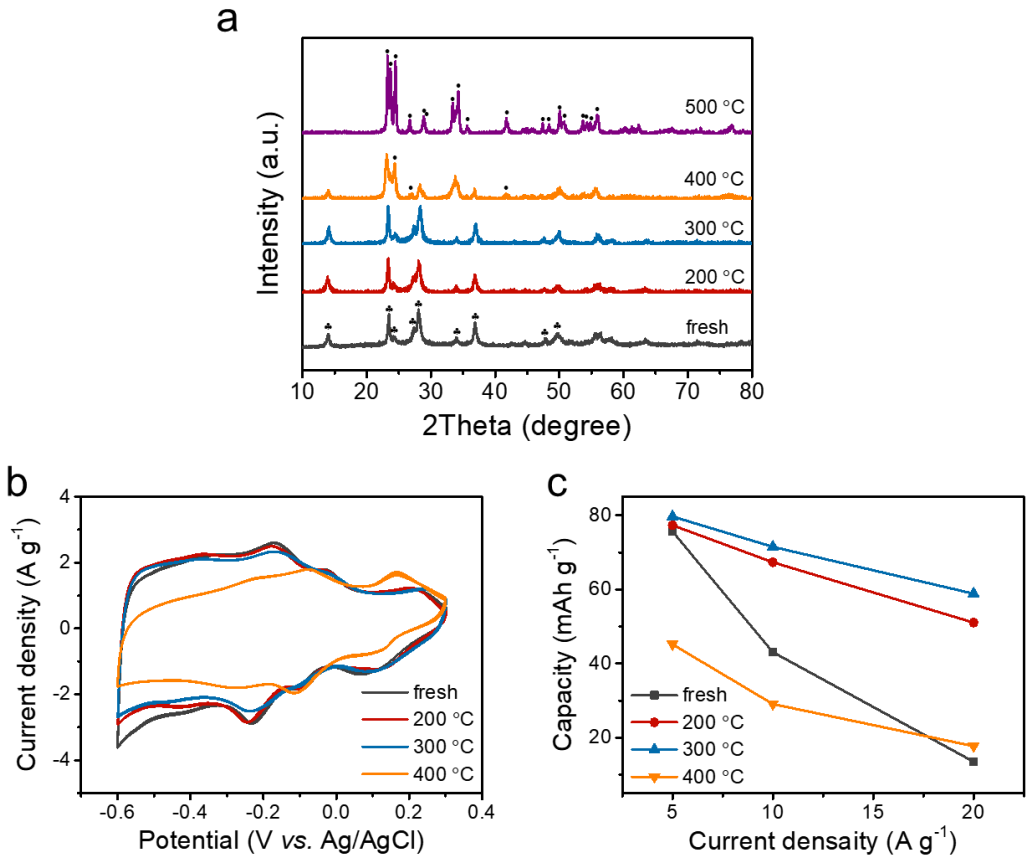

Figure 2-6. (a) XRD patterns, (b) Cyclic voltammogram (CV) tested at 5 mV/s, and (c) capacity dependence of as-prepared and heat treated hexagonal WO_3 synthesized with NH_4^+ ions.

Figure 2-7(a) shows XRD of hexagonal WO_3 synthesized using Na^+ ions as the template under heat treatment at 200 °C, 300 °C, 400 °C, and 500 °C for 4 hours. It is apparently that the hexagonal structure is able to maintain up to 400 °C. Further increasing the temperature converts the hexagonal structure into a monoclinic phase.

Electrochemical tests suggest that these samples exhibit typical CV curves of hexagonal WO_3. Capacitances of these samples are around 40-60 mAh/g, which decreases with increasing the heat-treatment temperature to 200 °C (**Figure 2-7**(c)). Further increasing the treatment temperature reduces the capacitance. Capacitances of such

samples are lower than those synthesized using NH_4^+ as the templating ions (**Figure 2-6**(c)). The samples also show improving rate performance after heat treatment. Although the sample heat treated at 400 °C was identified as a hexagonal phase by the XRD, the CV curve for this sample shows significant hydrogen evolution current at voltage window from –0.4 V to -0.6 V, which may indicate a phase transition to monoclinic, yet could not observe by XRD.

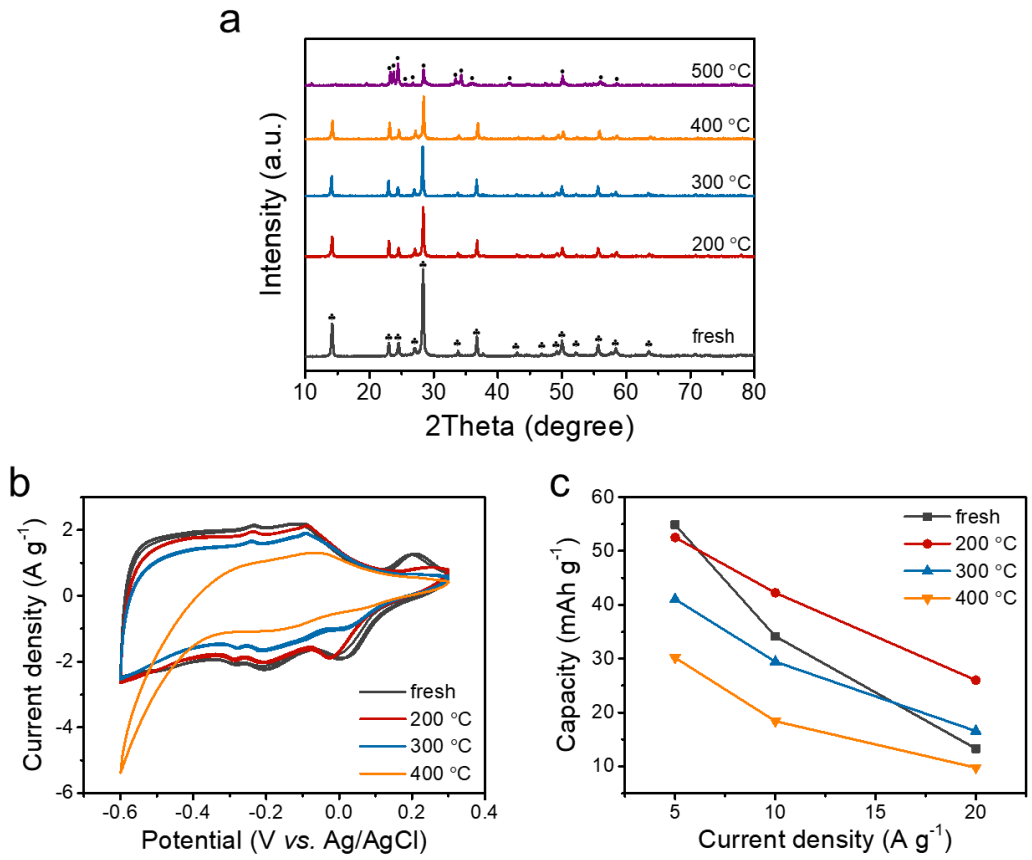

Figure 2-7. (a) XRD patterns, (b) Cyclic voltammogram (CV) tested at 5 mV/s, and (c) capacity dependence of as-prepared and heat treated hexagonal WO_3 synthesized with Na^+ cations.

2. WO_3 with Monoclinic Structure

Figure 2-8(a) shows XRD of monoclinic WO_3 samples after heat treatment at 200 °C, 300 °C, 400 °C, and 500 °C for 4 hours. The monoclinic phase up to 500 °C according to XRD results. Shapes of CV curves display in **Figure 2-8**(b) are similar only the capacitance shrinks after heat treatment. As shown in **Figure 2-8**(c), at a charging/discharging rate of 20 A/g, only less than 10 mAh/g capacities remain for all the samples. Therefore, although monoclinic WO_3 is much more stable at high temperature, their energy storage capability is reduced.

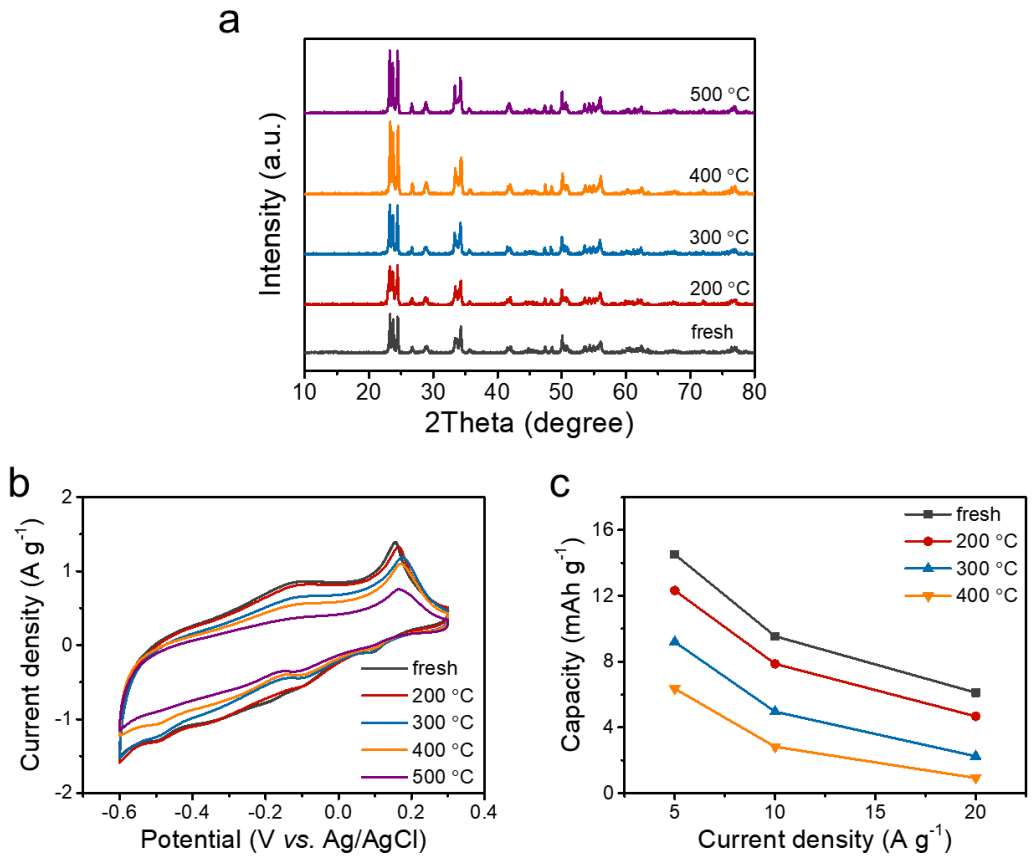

Figure 2-8. (a) XRD patterns, (b) Cyclic voltammogram (CV) tested at 5 mV/s, and (c) capacity dependence of as-prepared and heat treated monoclinic WO_3 samples.

3. WO_3 with Orthorhombic Structure

Figure 2-9(a) shows XRD of orthorhombic WO_3 synthesized under heat treatment at 200°C, 300°C, 400 °C, and 500 °C for 4 hours. It was found that these crystals are unstable upon heat treatment, transit to un-identical phase at 200 °C, and finally convert to the monoclinic phase at 500 °C. Electrochemical tests suggest that these samples possess capacitance around 50-70 mAh/g, which shows similar dependence with the heat-treatment temperature as the other phase of WO_3 (**Figure 2-9**(c)).

Generally, orthorhombic phase WO_3 is a thermodynamically stable phase, the observed phase transition should be contributed from the amorphous component formed from the hydrolysis of APT, which are subsequently converted to WO_3 with hexagonal, orthorhombic, cubic, or their mixed phases. It is difficult to fully identify their phase in this stage. We will synthesize orthorhombic WO_3 by other approaches, such as by using the highly soluble precursor ammonium metatungstate (AMT) or $NaWO_4$, which will be reported in the next report period.

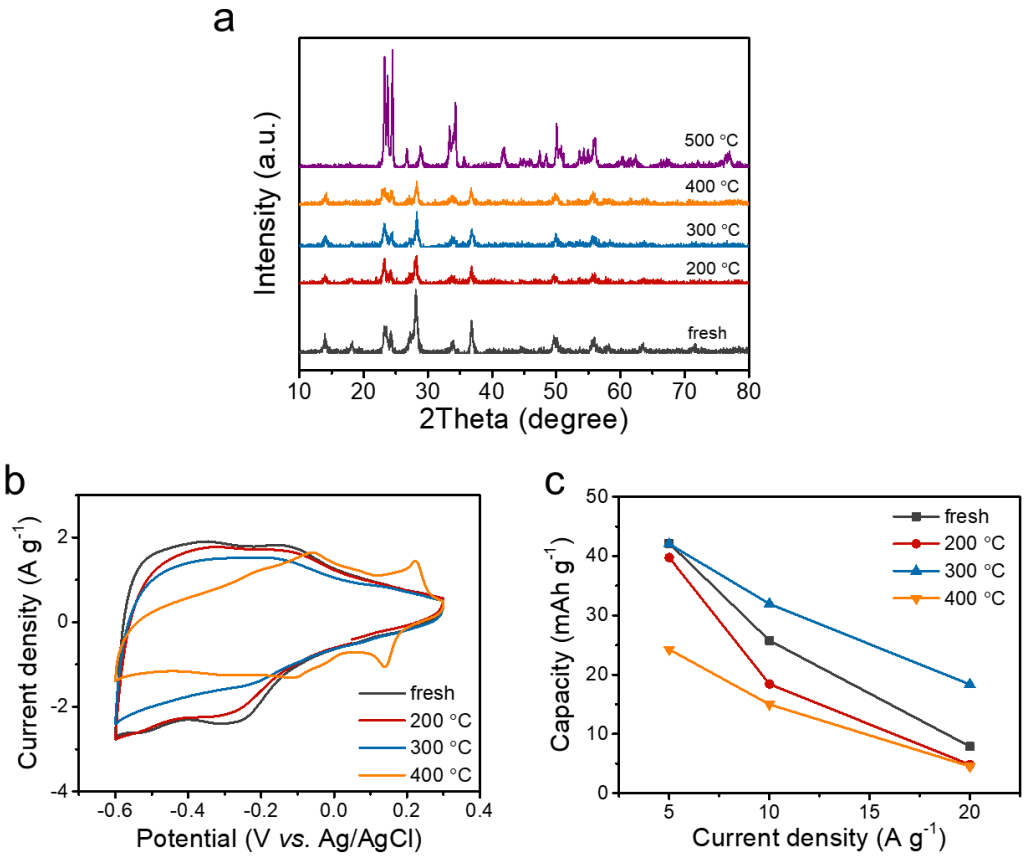

Figure 2-9. (a) XRD patterns, (b) cyclic voltammogram (CV) tested at 5 mV/s, and (c) capacity dependence of as-prepared and heat treated orthorhombic WO_3 samples.

All things considered, the hexagonal WO_3 exhibits the best energy storage and rate performance, and fairly thermal stability at same time among WO_3 with different crystal structures. Hexagonal WO_3 is chosen as the active material for this research. The effect of synthetic conditions of *h*-WO_3 will be discussed in the following section.

2.3 Effect of synthetic conditions of h-WO_3

2.3.1 Effect of Cations

Cations may play significant effect on the crystal structure formation. To understand their effect, we examined the effect of Na^+ and NH_4^+ ions. In order to

investigate their influence, three experiments were carried out as **Table 2-1**. Reaction solutions were prepared by adding Solution 2 to Solution 1, while the concentration for each component, reaction time (12h) and temperature (95 °C) remained the same. The obtained powder was washed with deionized water for 3 times and dried at 70°C for 12h. **Table 2-2** shows the crystal structure, water content, specific capacity, and yield of these reactions. Clearly, the presence of NH_4^+ is essential to direct the formation of WO_3 with hexagonal structure. Sample 1 (without NH_4^+) leads to the formation of orthorhombic structure, while Sample 2 and 3 (with NH_4^+) leads to the formation of hexagonal structure.

Table 2-1. The formulation used to test the effect of Na^+ and NH_4^+ ions on the crystal structure.

Sample	Solution 1	Solution 2
1	Na_2WO_4	H_2SO_4
2	Na_2WO_4	$(NH_4)_2SO_4$, H_2SO_4
3	Na_2WO_4, $(NH_4)_2SO_4$	H_2SO_4

Table 2-2. Crystal structure, water content, and capacity and yield of the samples prepared in the presence of Na^+ or NH_4^+ ions.

Sample	Crystal Structure	Crystal Size (nm)	Water Content ($WO_3 \cdot xH_2O$)	Specific Capacity ($mAh \cdot g^{-1}$)	Yield (%)
1	Orthorhombic	-	-	-	-
2	Hexagonal	7.2 ± 0.1	0.64	88.77	53.97
3	Hexagonal	7.9 ± 0.2	0.53	86.82	50.59

Figure 2-10 illustrates a possible mechanism relating to the NH_4^+-directed formation of WO_3 with hexagonal structure. Hydrogen bonding between the WO_3 octahedrons and the NH_4^+ ions directs the tungsten building blocks into a hexagonal assembly as illustrated in **Figure 2-10**. Subsequent condensation reaction between these building blocks in the acidic environment results in the formation of hexagonal WO_3 containing water molecules in the channels. Such finding is extremely important in guiding the synthesis, as well as further material development. For example, it may become possible to use amines with large molecular size to direct the formation of WO_3 with large pore structure for other applications, ranging from catalysts to energy storage and conversion.

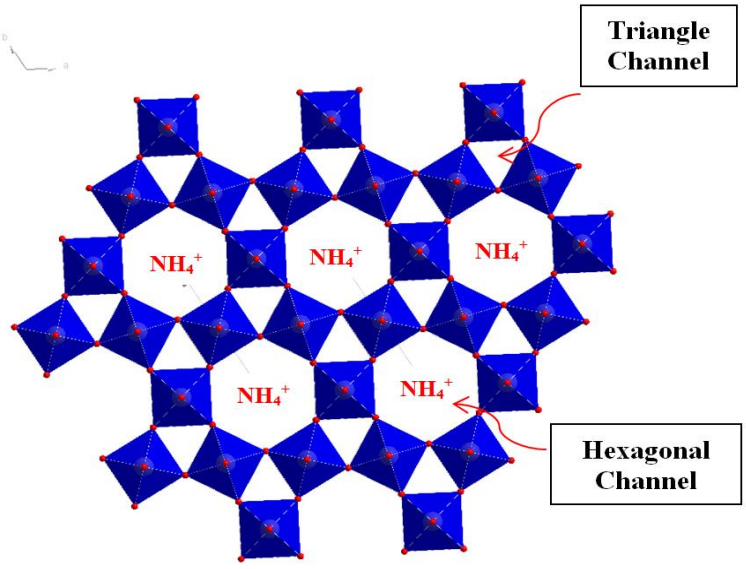

Figure 2-10. Schematic illustration of the formation of hexagonal WO_3 directed by NH_4^+ ions.

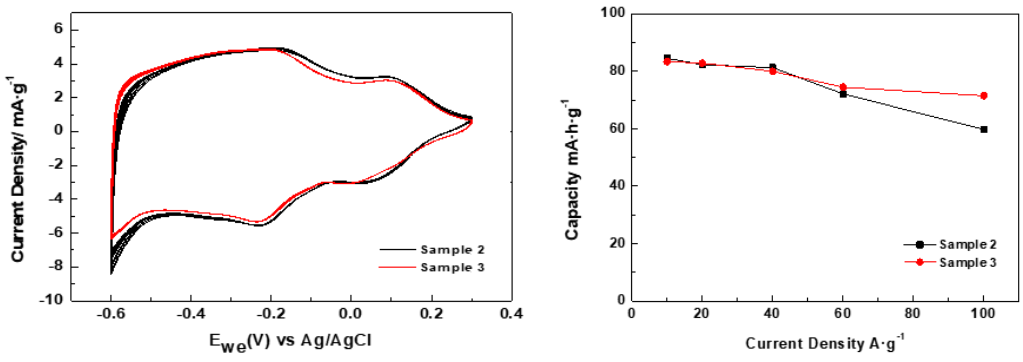

Figure 2-11. Cyclic voltammogram (CV) (LEFT) and capacitance dependence (RIGHT) of Sample 2 and Sample 3.

It was found that as-synthesized orthorhombic WO_3 (Sample 1) exhibit intense hydrogen evolution and could not be charged to -0.6 V vs Ag/AgCl. The storage performance of Sample 2 and Sample 3 were also compared in **Figure 2-11**. It seems that Sample 3 (premixing Na_2WO_4 with $(NH_4)_2SO_4$ followed by adding H_2SO_4) exhibits a relatively high over potential for hydrogen evolution than Sample 2 (premixing H_2SO_4 with $(NH_4)_2SO_4$ followed by adding to Na_2WO_4). Such phenomena suggest that small amount of orthorhombic WO_3 may be formed within the Sample 2. Therefore, based on this study, we identify an important synthesis parameter leading to better WO_3 performance.

2.3.2 Effect of pH

As discussed early, the formation of WO_3 crystals is based on the condensation reaction of WO_3 octahedrons in acidic solution. Similar to other inorganic condensation reactions, pH may play essential roles in the resulted structure. To examine this effect, we also synthesized a series of samples (95 °C for 24 hours reaction) using different amount of acid. This was achieved by using the same volume of H_2SO_4 (4M, 5M, and 6M, respectively) for the synthesis (see the synthesis section).

Table 2-3 shows the initial pH values of six reacting solutions, as well as the crystal structure, water content, capacity and yield of the WO_3 resulted from these reactions. At low pH values (Initial pH = -0.74), predominating species $W\text{-}OH_2^+$ rapidly condense with each other, leading to the formation of WO_3 with orthorhombic structure (**Figure 2-12**). Therefore, under this reaction condition, the structure-directing effect of NH_4^+ is less effective. At higher pH (Initial reacting solution pH = 0, 0.37, 1.96, 2.86), as formed WO_3 exhibit the hexagonal structure, suggesting that a higher pH leads to slower condensation reaction, which allowing the NH_4^+ ions to direct the formation of hexagonal structure. In particular, since the isoelectric point of WO_3 is ~ 2.5, Sample **5** has even slower condensation reaction rate, which is consistent with its low yield (~ 3.5%). At pH above the isoelectric point, no product was obtained.

Table 2-3. Crystal structure, water content, specific capacity and yield of the samples prepared with different pH values.

Sample	pH H_2SO_4 added	Initial Solution pH	Crystal Structure	Crystal size (nm)	Water Content *x* ($WO_3 \cdot xH_2O$)	Specific Capacity ($mAh \cdot g^{-1}$)	Yield (%)
1	-1	-0.74	Orthorhombic	23.5±2.6	1.03	54.79	95.16
2	-0.5	0	Hexagonal	13.7±0.6	0.45	80.64	67.16
3	-0.3	0.37	Hexagonal	8.5±0.2	0.48	77.52	67.17
4	0	1.96	Hexagonal	7.9±0.2	0.53	86.83	53.97
5	0.3	2.86	Hexagonal	7.9±0.3	0.65	88.90	3.49
6	0.5	5.57	No product	-	-	-	-

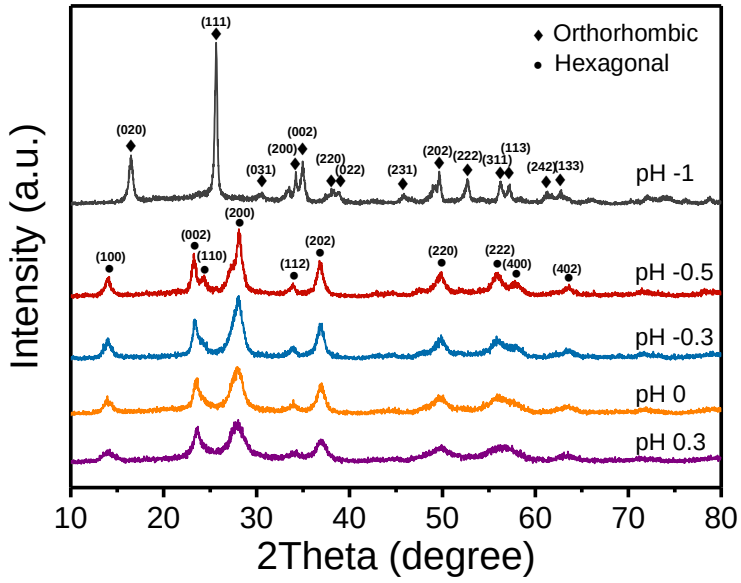

Figure 2-12. XRD results of WO_3 samples synthesized at different pH values.

The crystal sizes and water content for the hexagonal structure samples are similar, expect Sample **2** synthesized at lower pH (pH= 0) shows somewhat larger crystal size (~ 13.7 nm), consistent with a high condensation reaction rate. **Figure 2-13** compares the energy storage performance of each sample. Compared to the samples with hexagonal structure, orthorhombic WO_3 exhibits smaller specific capacity, less obvious redox peaks, and significant hydrogen evolution at -0.6 V vs. Ag/AgCl. For the hexagonal WO_3 synthesized with different pH, significantly higher capacitance and obvious redox peaks are observed; the hydrogen evolution potentials seem to be similar. Nevertheless, Sample **5** seems exhibit relatively intense hydrogen evolution.

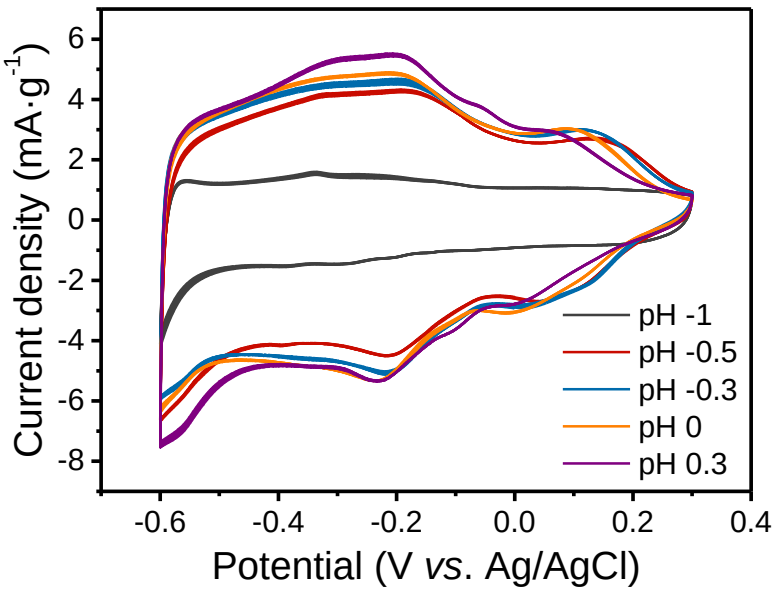

Figure 2-13. Cyclic voltammogram (CV) curves of the samples synthesized at different pH values.

Figure 2-14 further compares the specific capacitance of the hexagonal-structured samples at different current densities by galvanostatic charge/discharge studies. Sample **4** (initial reacting solution pH = 1.96) shows the best rate performance and specific capacitance. Based on the pH studies, we conclude that a reacting condition with initial pH ~ 2.0 will be the optimum pH to synthesize WO_3 with high energy-storage performance at relatively high yield.

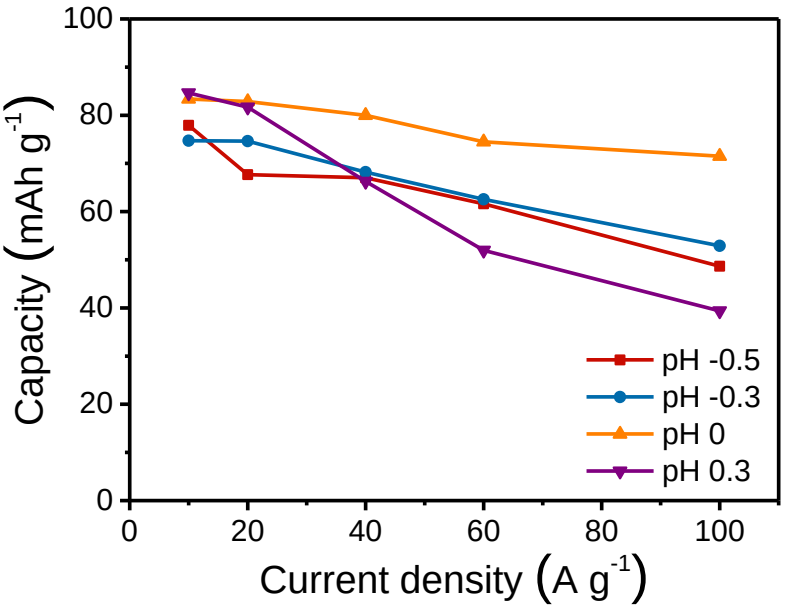

Figure 2-14. Specific capacitance of the samples synthesized at different pH values.

2.3.3. Effect of Reaction Time

Another factor that impacts on the growing of WO_3 crystals is reaction time. To examine this effect, a series of WO_3 samples were synthesized at 95 °C for different time (3hr, 6hr, 12hr). **Table 2-4** shows the crystal structure, capacity and yield of the as-synthesized samples. All the WO_3 samples have the hexagonal structure (**Figure 2-15**). The yield increases with reaction time.

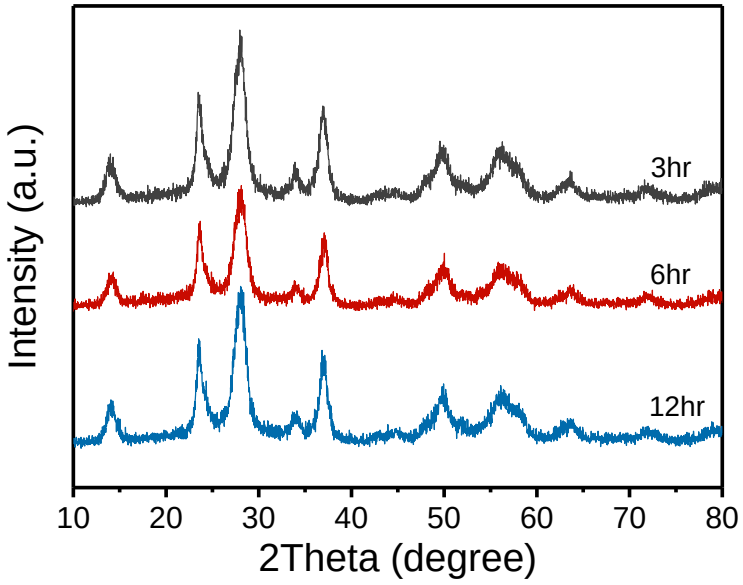

Figure 2-15. XRD results of WO_3 samples synthesized under different reaction time.

Table 2-4. Crystal structure, crystal size, specific capacity and yield of the samples prepared by different synthesis time.

Reaction Time	Crystal Structure	Crystal size (nm)	Specific Capacity ($mAh \cdot g^{-1}$)	Yield (%)
3h	Hexagonal	8.2±0.1	46.671	39.92
6h	Hexagonal	10.2±0.7	70.170	49.11
12h	Hexagonal	8.5±0.2	83.395	58.09

Figure 2-16 shows the CV curves (Left) and capacitance-current density dependence (Right) of as-synthesized samples. All the three samples exhibit similar CV curves and capacitance, but redox peak at -0.2V of the sample synthesized for 3hr shrinks after few cycles, suggesting a less stable structure. Therefore, long enough reaction is necessary to

synthesize WO_3 with stable performance. Their difference in energy-storage performance can be observed much clearly in the galvanostatic charge/discharge tests. The sample synthesized by a longer time has higher specific capacity and good rate performance. At the high current density, the capacity delivered by the sample synthesized for 3hr decreased to only about 20 mAh g^{-1}.

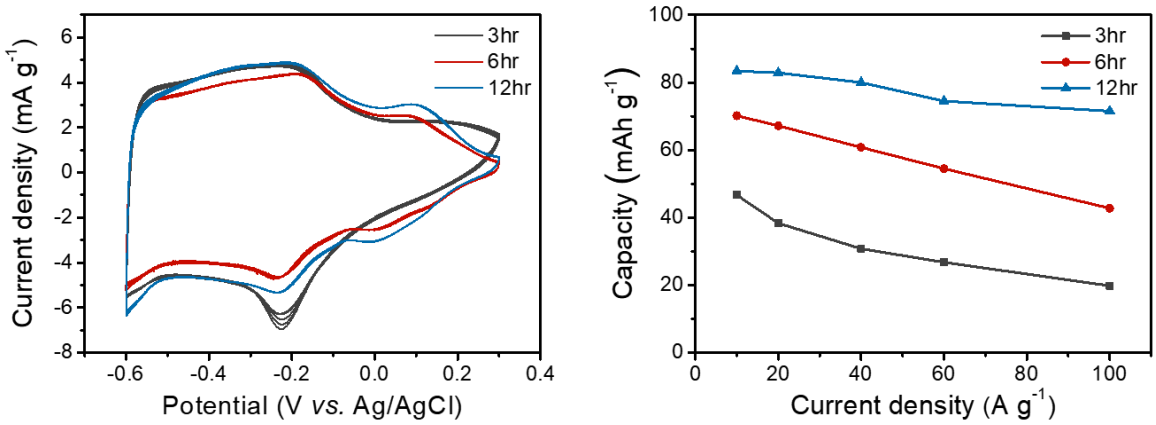

Figure 2-16. Cyclic voltammogram (CV) (Left) and capacitance dependence (Right) of various samples synthesized with different reaction time.

This study suggests that prolonging reaction time could contribute to better crystal structure formation, which leads to improved electrochemical performance and higher yield. However, extending the synthesis time would consume more energy.

2.4 The electric conductivity of WO_3

The conductivity of WO_3 was measured in the temperature range from 80 °C to 360 °C under dry H_2 or N_2. The pellet tested under N_2 undergone a pretreatment in H_2 at 80 °C for 1 hour. 0.1 wt% Pt/WO_3 sample also prepared and tested to investigate the effect of the catalyst on conductivity. The sample was prepared by mixing certain ratio of Pt black with WO_3 powder and grounding until uniform.

As shown in **Figure 2-17**(b), as synthesized WO_3 exhibit semiconductive behavior with a proton conductivity ~ 1.0 mS/cm at 20 °C and an electronic conductivity in the order of 10^{-5} mS/cm. In the presence of Pt, WO_3 is rapidly converted into conductive non-stoichiometric oxides when it is exposed to H_2 at room temperature. As shown in the **Figure 2-17(a)**, the impedance spectra of 0.1 wt% Pt/WO_3 in H_2 exhibits the feature of the electronic conductor. The electronic conductivity of 0.1 wt% Pt/WO_3 is quantitatively presented in **Figure 2-17(c)** in Arrhenius form. Under H_2 atmosphere, 0.1 wt% Pt/WO_3 sample reveals an electronic conductivity of ~ 0.3 S/cm at 80 °C and a metallic conducting behavior, of which the resistance increases with temperature in the range of 80 °C to 180 °C. When the temperature rises to 200 °C, the conductivity declines sharply and hits the minimum at 260 °C (~ 50 mS/cm). Continue to raise the temperature, the conductivity rebounds to the initial level. The conductivities measured in N_2 have the same tendency with that in H_2 but slightly lower in the value. The reduction of conductivity during 180 °C to 260 °C can be attributed to the loss of the water molecules within the WO_3 channels. After the dehydration, protons refill into the channels and then form the stable hydrogen tungsten bronze.

To confirm this conjecture, a 0.1 wt% Pt/WO_3 sample was measured in a heating-cooling cycle. The temperature was increased stepwise from 80 °C to 360 °C. After having maintained the sample at 360 °C, the temperature was decreased stepwise in the cooling process from 360 °C to 80 °C. Then another heating cycle was carried out up to 360 °C. **Figure 2-18** shows the results of the two heating cycles. After the first heating cycle, the Arrhenius plots of cooling and second heating are both linear, revealing a metallic conducting behavior. Although the conductivity plot of the second heating cycle is slightly

lower than that of the cooling cycle, it still remains at the level of ~ 0.3 S/cm. Pure WO_3 samples exhibit similar tendency in H_2 with those containing Pt catalyst, although a higher temperature and longer time is needed to convert it to a metallic conductor.

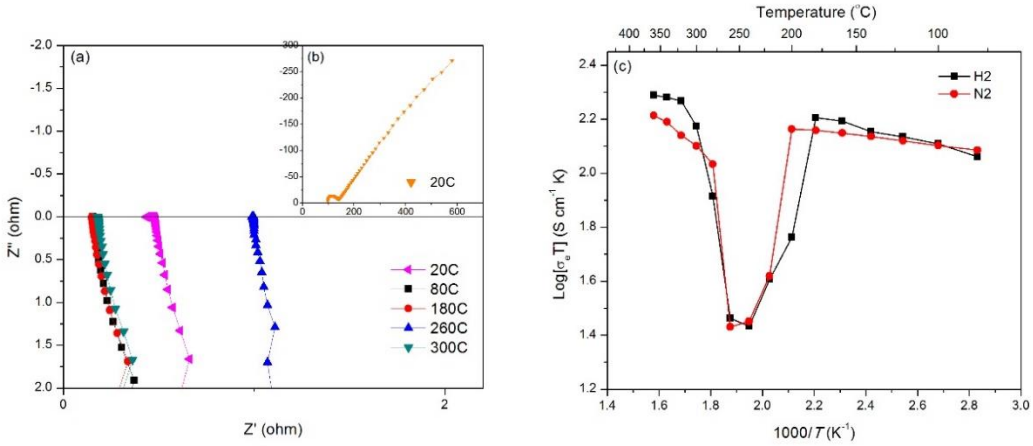

Figure 2-17. Typical impedance spectra of 0.1 wt% Pt/WO_3 measured (a) in H_2 and (b) in the air; (c) Conductivity of 0.1 wt% Pt/WO_3 under H_2 or N_2.

Note that tungsten bronzes generally exhibit electronic conductivities in the order of mS/cm^{-1} scale, which is two-order lower than the conductivities we obtained. Although it is difficult to distinguish the proton and electronic contribution, based on the conductivity results obtained from the literature, it is reasonable to conclude that the mixed conductivity is mainly contributed from the proton conductivity. It is reasonable that protons react with WO_3 forming H_xWO_3, creating reacting pathways for proton transport. Further studies are needed to de-convolute the contribution, which will be conducted as the future research. In the aspect of electronic conductivity of the electrodes, it is relatively easy to increase the conductivity by adding electronic conductive agent, such as carbon and metallic agents.

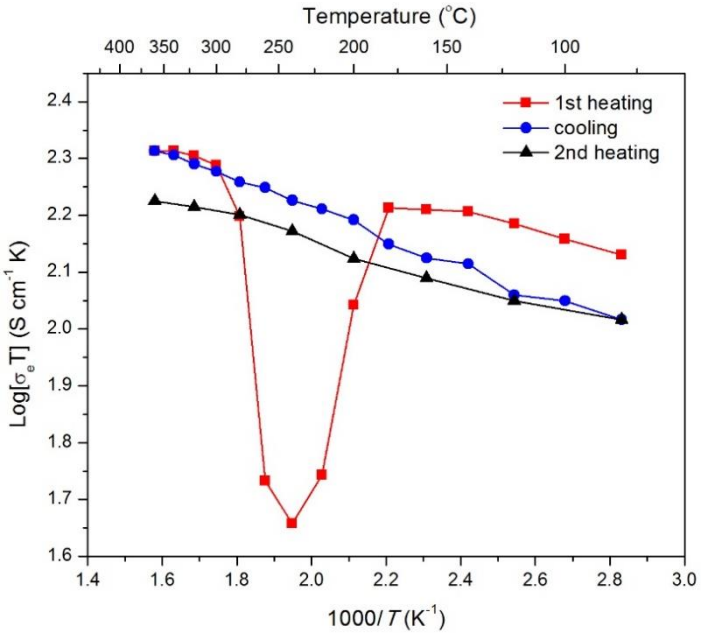

Figure 2-18. The conductivity of 0.1 wt% Pt/WO_3 under H_2 during two heating cycles.

2.5 Design and synthesis of WO_3/carbon composites

The WO_3 and carbon composite were synthesized through a one-pot hydrothermal process using aqueous WO_3 precursor with carbon sources. Briefly, designed amount of $Na_2WO_4 \cdot 2H_2O$ and $(NH_4)_2SO_4$ were dissolved in 50 mL DI water and 3 M H_2SO_4 was added to adjust the pH value to 1.5. Then XC-72 carbon or carbon nanotubes (CNT) was introduced and dispersed by sonication. The desired weight ratio of carbon species in WO_3/carbon composites was 90%. The precursor solution was transferred to 100 ml Teflon autoclave and underwent hydrothermal process at 180°C for 12h.

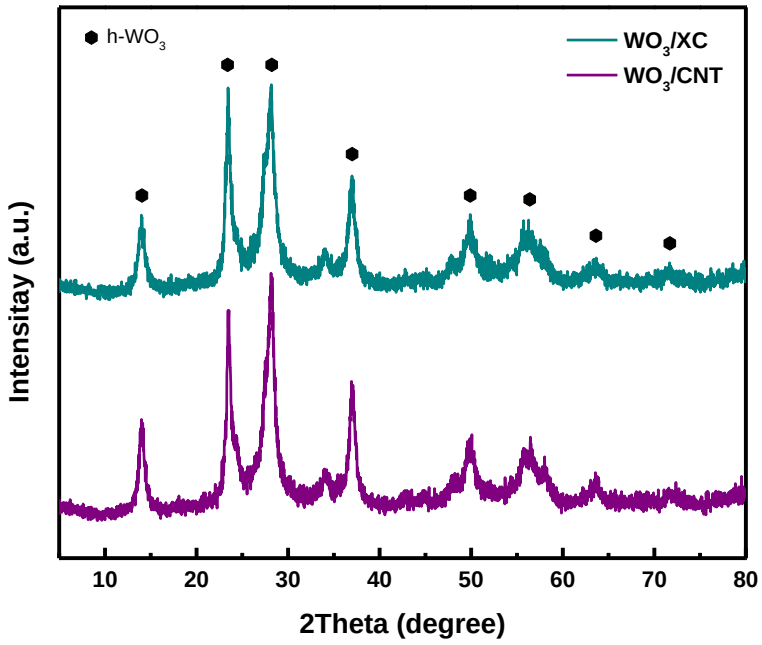

Figure 2-19. XRD patterns of the WO_3 and carbon composites.

Figure 2-19 shows the XRD patterns of the as prepared WO_3/XC and WO_3/CNT composites. WO_3 in both samples exhibit hexagonal structure. **Figure 2-20** displays TGA profiles of the samples in air. As we can see, the curves of the two samples are almost overlapped below 400 °C. According to our previous studies, the weight loss below 400 °C is mainly due to removal of the H_2O within the WO_3 crystals. After temperature increased up to 600 °C, all the carbon in the composites were burned off and only WO_3 left. The weight loss of the WO_3/XC and WO_3/CNT are about 14% and 13%, respectively. Accordingly, the weight percentage of the WO_3 in the above two samples are 86% and 87%.

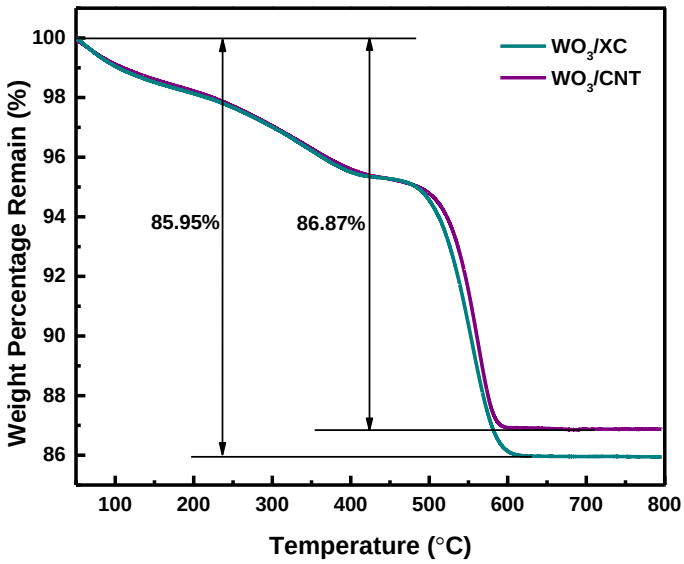

Figure 2-20. TGA curves of the WO_3 and carbon composites.

Figure 2-21 shows the SEM images of the as prepared samples. The particles of XC is about 20-40 nm in diameter, showing a poor attachment of the WO_3 nanorod. In contrast, the CNT and WO_3 nanorod intertwine into networks. It can be expected that such structure ensures short diffusion length, continuous conductive pathway, and intimate interface contacts between the WO_3 and the CNT, which could endow the electrodes with excellent energy storage ability.

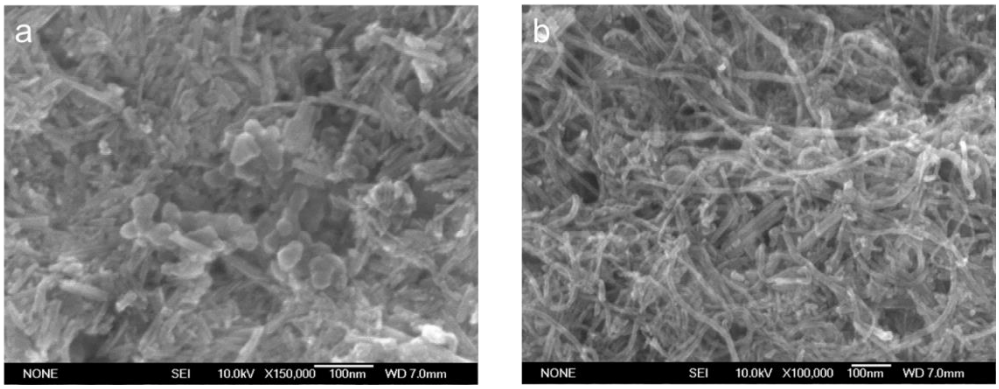

Figure 2-21. SEM images of the (a)WO_3/XC and (b)WO_3/CNT composites.

We further synthesized the composites of WO_3/CNT with different CNT contents. CNT will provide better electronic conductivity, which will enhance the overcall storage capability of the composites. However, CNT themselves could provide effective energy store capability, therefore, it is necessary to control the ratios between WO_3 and CNT in order to optimize their storage performance. Towards this goal, composites of WO_3 and CNT containing 70%, 80% or 90% of WO_3 were synthesized through a one-pot hydrothermal process.

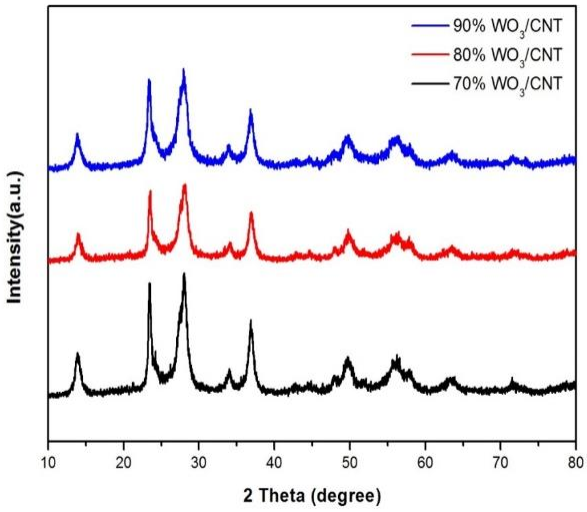

Figure 2-22. XRD patterns of the as-prepared WO_3/CNT samples.

Figure 2-22 shows the XRD patterns of the as-prepared WO_3/CNT composites. The WO_3 in all the samples exhibits similar hexagonal structure (see the previous reports for the indexing of the diffraction peaks). **Figure 2-23** displays the TGA profiles of the samples in air. The weight loss below 400 °C is mainly due to the removal of the H_2O within the WO_3 crystals. After the temperature was increased to 600 °C, the carbon

moieties were burned off and only the WO_3 was left. The weight loss of the WO_3/CNT composites is 33.04%, 22.52% and 15.53%, respectively. Accordingly, the weight percentage of the WO_3 in the composites is 67.0%, 77.5% and 84.5%, respectively.

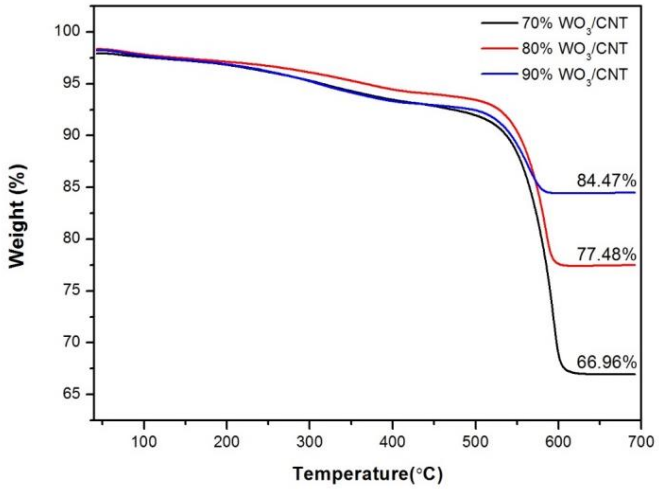

Figure 2-23. TGA profiles of the as-prepared WO_3/CNT samples.

Figure 2-24 shows the SEM images and EDS mapping of the as-prepared samples, showing an intertwine structure formed by the CNTs and WO_3 nanorods. As shown in the EDX mapping images of C, O and W elements, the distribution of the W moiety is consistent with that of the C and O moieties, indicating that uniform distribution of the W moiety within the composites. Such composite structure will provide continuous conductive pathways, leading to excellent energy storage capability. Above results suggest that we have successfully synthesized the composites with different CNT/WO_3 ratios, which can be used for MEAs with energy storage capability.

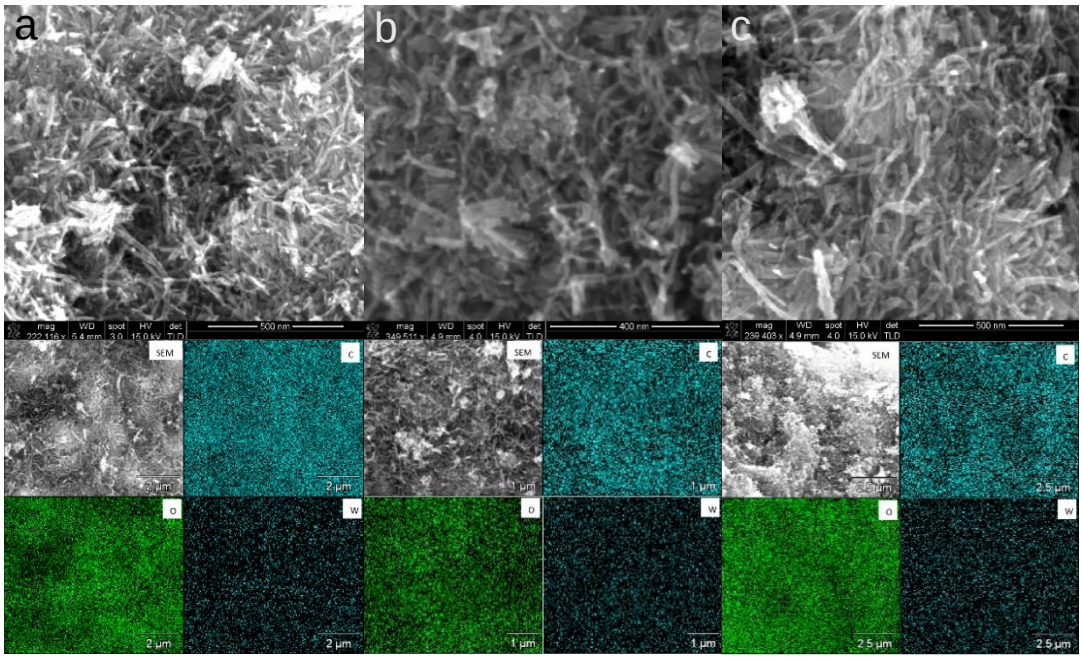

Figure 2-24. SEM images and EDS mapping of the as-prepared WO_3/CNT samples: (a) 70 % WO_3/CNT; (b) 80 % WO_3/CNT; (c) 90 % WO_3/CNT.

Since the water electrolysis reaction would occur on the carbon materials in the aqueous electrolyte at low potential, the electrochemical performance of WO_3/carbon composites will characterize in the fuel cell configuration in the next chapter.

2.6 Conclusions

In summary, we have synthesized WO_3 with hexagonal, monoclinic, cubic, or orthorhombic structure. Take the thermal stability and electrochemical performance into consideration, WO_3 with hexagonal structure is the best material for this study. The synthesizing conditions of *h*-WO_3 were optimized. With the present of Pt, WO_3 was proved to react with H_2 rapidly to form hydrogen tungsten bronze by the electric conductivity measurement. WO_3/carbon composite materials were prepared in the aim of improving the electrochemical performance of WO_3 sample.

2.7 Experiment methods

2.7.1 Material Synthesis

Monoclinic: Monoclinic WO_3 was prepared by a hydrothermal method. Briefly, 4.2 g $Na_2WO_4 \cdot 2H_2O$ was dissolved in 50 mL DI water. Then 3 M H_2SO_4 was added into the solution dropwise under stirring to adjust the pH value of solution to 0. The precursor solution was then placed to 100 ml Teflon autoclave and underwent hydrothermal process at 180°C for 24h.

Orthorhombic: Orthorhombic WO_3 was prepared by hydrolyzing ammonium paratungstate (APT) using 6 M HNO_3. Briefly, 2.61g APT was added into 50mL DI water and then 6M HNO_3 was added into the solution dropwise under stirring to adjust the pH value of solution to -0.5. The precursor was transferred to 100 mL autoclave and react at 95°C for 18h.

Hexagonal: Hexagonal WO_3 was synthesized using NH_4^+ or Na^+ as the templating agent. For the former case, 4.2g $Na_2WO_4 \cdot 2H_2O$ and 1.65g $(NH_4)_2SO_4$ were dissolved in 50 mL DI water. Then H_2SO_4 was added into the solution dropwise under stirring to adjust the pH value of solution. Then the precursor solution was placed to 100 ml Teflon autoclave and underwent hydrothermal process at 180°C for different time. For the latter case, hexagonal WO_3 was synthesized followed the same procedure but replacing the $(NH_4)_2SO_4$ with 1.78g Na_2SO_4.

Cubic: Cubic WO_3 was synthesized using a hydrothermal method. 4.2g $Na_2WO_4 \cdot 2H_2O$ and 17.75g Na_2SO_4 were dissolved in 50 mL DI water. Then 3 M H_2SO_4 was added into the solution dropwise under stirring to adjust the pH value of solution to

1.5. The precursor solution then placed in 100 ml Teflon autoclave and underwent hydrothermal process at 180 °C for 24h.

WO_3/carbon composites: A designed amount of $Na_2WO_4 \cdot 2H_2O$ (≥ 99% purity) and $(NH_4)_2SO_4$ (≥ 99.0% purity) were dissolved in 50 mL DI water, and 3 M H_2SO_4 was added to adjust the pH value to 1.5. XC-72 carbon or CNTs were then dispersed in the solution by sonication to achieve a desired weight ratio. The solution was then transferred to a 100 ml Teflon autoclave and reacted at 180°C for 12 h. The resulting WO_3/carbon composites were washed with DI water and dried for further use.

2.7.2 Characteristics of physical and electrochemical properties

Transmission electron microscopy (TEM) images were taken on a FEI Tecnai G2 F20 microscope operated at an accelerating voltage of 200 kV. X-ray diffraction (XRD) measurement was performed on a Rigaku X-2000 diffractometer using Cu Kα radiation with a Ni filter. The tube voltage and the tube current were maintained at 40 kV and 100 mA, respectively. The sample was scanned from 10º to 80º (2θ) at a scan rate of 5º min^{-1}. Thermogravimetric analysis (TGA, TA Instruments, U.S.A.) was conducted in an air environment. During the measurement, samples were initially held at 100 ºC for 15 min to remove trapped water, and subsequently heated to 700 ºC at a heating rate of 5 ºC min^{-1}.

The electrochemical measurements of the composite were conducted on a BioLogic VMP-300 multipotentiostat workstation (Bio-Logic Science Instruments, France). The electrolyte solution was 0.5 M H_2SO_4. Ag/AgCl and platinum foil were used as the reference electrode and the counter electrode, respectively. To fabricate the electrodes, WO_3 sample, carbon black and PVdF (Kynar) binder were mixed in a mass ratio of 9:0.5:0.5 and homogenized in N-methyl-2-pyrrolidone (NMP) to form slurry. The

homogenous slurry was coated on Ti foil substrates and dried at 90 ºC for 6 h under vacuum. As-formed electrodes were then pressed under a pressure of 2 MPa.

For the electric conductivity measurement, the samples were pressed into pellets under a pressure of 6×10^3 kg cm^{-2}. Silver wires were applied on both sides of the obtained pellets using silver paste. The pellet samples were set in a quartz tube, and then hydrogen or nitrogen were supplied through the quartz tube at atmospheric pressure. Conductivity measurements were performed by means of ac impedance spectroscopy using a Solartion 1287 impedance analyzer in the frequency range from 10MHz to 1Hz with an applied voltage of 10 mV. The conductivity as a function of temperature was measured by stepwise increase the temperature from room temperature to 360 °C.

Chapter 3. Demonstration and Optimization of the Hybrid Fuel Cell

3.1 Introduction

The performance and durability of PEM fuel cells are highly influenced by the cell structure design and operating conditions. PEM fuel cells can be operated at varying conditions of cell temperature, total pressure, partial pressure of reactants, and relative humidity.

One of the advantages of the PEMFC is its low operating temperature (ca. 60–90 °C); the temperature is usually controlled through an external cooling flow. Since the cell performance is sensitive to its temperature, many authors have analyzed this influence.[96-101] At higher operating temperature, the kinetics of HOR, ORR will be much faster than at low temperature. And the proton transport, as well as the mass transport of H_2 and O_2 will enhanced. However, operating PEM fuel cells at high temperature, especially over 95 °C, for long time will shorten the lifespan of devices. Catalysts, carbon materials, membranes and bipolars are degrade in higher rate at high temperature. Moreover, the water management at high temperature is more difficult.

Water management is one of the most important aspects of a PEMFC, especially to maintain a good proton conductivity. Many papers are devoted to understanding the mechanisms of water transport inside the membrane,[102-104] while others explored the link between water management and cell performance .[96-98, 100-101, 105]

Another operating variable that affects the performance of the PEMFC is the operating pressure of the reactants.[94-96]

The MEA configuration is other important factor to determine the performance of the fuel cell device. As known, GDL is one critical component of fuel cells, which performs several important tasks: 1) allowing transport of the reactant gas from the flow channels to the catalyst layer, 2) draining out liquid water from the catalyst layers to the gas-flow channels, and 3) conducting electrons, and 4) and helping to maintain the membrane with certain humidity. To fulfill these purposes, an ideal GDL should process good electronic conductivity, optimal porosity and pore structure, as well as a balanced wettability.

It is our goal to coat a sufficient amount of WO_3/CNT onto the carbon paper to form the energy-storage electrodes with sufficient energy-storage capacity and power, while maintains the essential transport characteristics needed as the GDL for fuel cells.

In this chapter, the feasibility of WO_3 materials in the PEM fuel cell application will be demonstrated by WO_3-oxygen battery test first. Then the MEA structure and operating conditions for the PEM fuel cell with WO_3 electrode integrated will be optimized.

3.2 Fabrication and Characterization of the WO_3-oxygen battery

Figure 3-1 schematically presents the structure and operation principle of the re-chargeable WO_3-oxygen battery. The charging of the WO_3-oxygen battery is enabled by fed hydrogen into the Pt/C electrode. The hydrogen is oxidized on the Pt/C electrode, working as the dynamic hydrogen reference electrode (DHE). The proton released from hydrogen is transferred toward and stored in the WO_3 electrode. WO_3-oxygen battery is discharged when supplying oxygen to the Pt/C electrode. The charged WO_3 electrode will be oxidized and release protons and electrons. The electrons pass through the electrical circuit to the cathode. Combining with the protons and electrons, the oxygen is reduced to water on the Pt/C electrode.

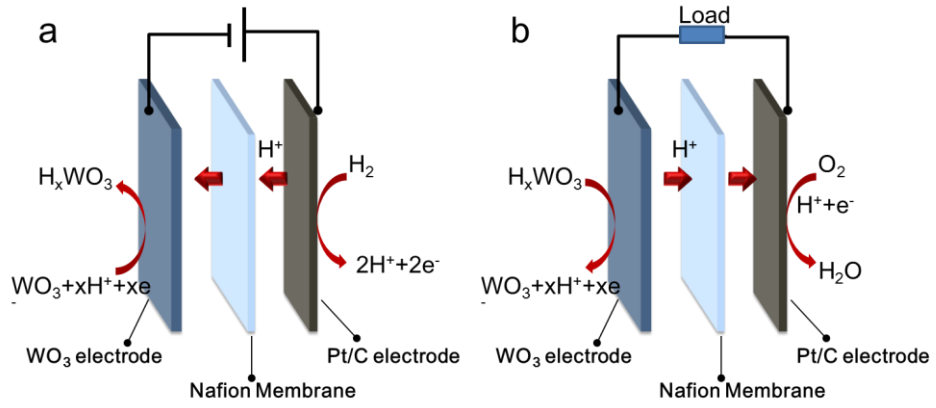

Figure 3-1. Schematic illustration of the configuration and general working mechanism of (a) discharging process (b) charging process for the rechargeable WO_3-oxygen battery.

To explore the energy storage capability of the WO_3 electrodes, all the electrodes were first charged to constant potential and then discharged at different rates. Here, the terminal charging potential of -0.3 V (vs. DHE) was investigated, for the reason to avoid the side reactions such as water electrolysis caused by carbon species in the electrode.

Figure 3-2 shows the galvanostatic discharging curves of the WO_3-oxygen battery based on a WO_3/XC electrode that was pre-charged to -0.3V *vs.* DHE. The open circuit voltage is about 1.23 V, which is of 300 mV lower than the theoretically expected values of 1.53V. This is mainly caused by the mixed potential of the Pt/PtO catalyst surface.[106] The voltage decreases with the consuming of the active material under different discharge current densities. The time for the WO_3-oxygen battery to supply electrical energy at different discharge current densities are shown in **Figure 3-2**(a). It can be seen that this device is able to supply the electrical energy for 1473 s at a discharge current density of 10 mA cm^{-2}. Even when the output current density increases to 200 mA cm^{-2}, the device could provide a backup power for 21s. However, the WO_3/XC electrode shows poor rate performance. For example, at a relatively low current density of 10 mA cm^{-2}, the WO_3

electrode could deliver a discharge current capacity of 84 mAh g^{-1}, while the capacity was only 40 mAh g^{-1} at a current density of 200 mA cm^{-2} (**Figure 3-2**(b)). This is possibly due to the inefficient electron and ion transport, also the low utility of the active material in the thick electrode.

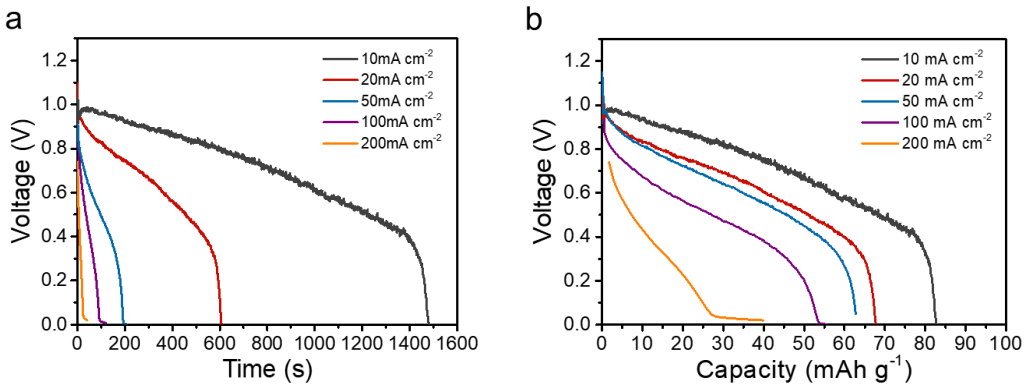

Figure 3-2. Galvanostatic discharging curves of WO_3-oxygen battery based on a WO_3/XC electrode (charged to -0.3 V *vs.* DHE) at different current densities.

To further enhance the performance of the WO_3-oxygen battery, WO_3/CNT composite was applied as the active material to fabricate electrode. **Figure 3-3** shows the galvanostatic discharging curves of WO_3-oxygen battery based on a WO_3/CNT electrode. As we can see, the WO_3/CNT electrode can deliver a capacity of 60-70 mAh g^{-1} at the current densities of 10 mA cm^{-2} (0.2 A g^{-1}) to 200 mA cm^{-2} (4.6 A g^{-1}), exhibiting improved rate performance comparing to WO_3/XC composite. It can be ascribed to the fast electron transport inside the network of WO_3 and CNT particles.

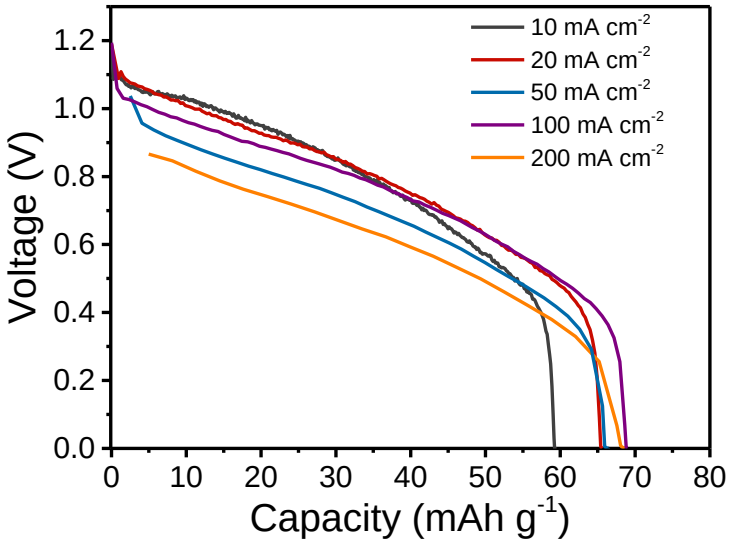

Figure 3-3. Galvanostatic discharging curves of WO_3-oxygen battery based on a WO_3/CNT electrode (charged to -0.3V *vs.* DHE) at different current densities.

The ratio of the carbon specie inside the active material need to optimize as well, since too much carbon adding into the composite will increase the electrode volume and the cost. WO_3-oxygen batteries fabricated by WO_3/CNT composites with different WO_3 to CNT rations were measured. **Figure 3-4** shows the galvanostatic discharging curves of WO_3-oxygen batteries at different discharging rates. The cells exhibit typical capacitive discharging behavior. The cell fabricated with 90%WO_3/CNT exhibits poor rate performance due to low electric conductivity. With increasing the content of CNT in the composites, the supercapacitor made from 80%WO_3/CNT exhibits improved rate performance, which delivers a specific capacity of 80 mAh/g at a discharging rate of 200 C. However, since CNT provides much less capacity than WO_3, further increasing the content of CNT would not benefit the overall performance of WO_3/CNT electrode.

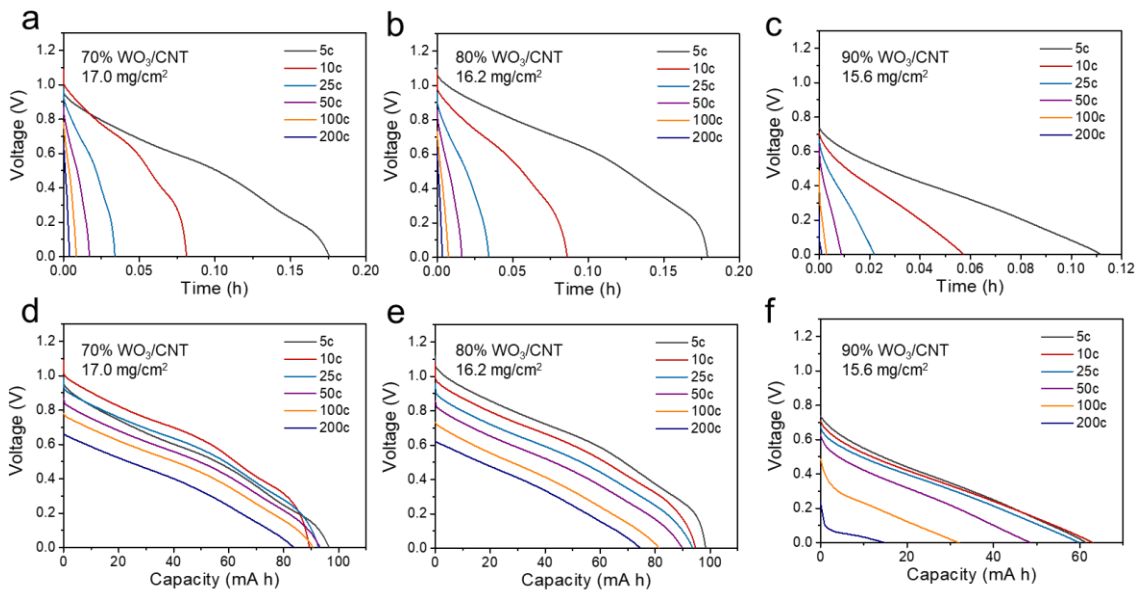

Figure 3-4. Galvanostatic discharge curves of WO_3-oxygen batteries made from WO_3 /CNT composites with WO_3 content of (a, d) 70%, (b, e) 80% and (c, f) 90%. Cells were charged to -0.3 V prior to the discharging.

To further evaluate the performance of WO_3-oxygen batteries under the operating condition of the PEMFC (i.e. anode side potential of ~ 0 V), the WO_3-oxygen batteries were pre-charged to 0 V (*vs.* DHE), and the galvanostatic discharging curves are shown in **Figure 3-5**. The optimized cell could still deliver a specific capacity between 33 mAh/g to 45 mAh/g.

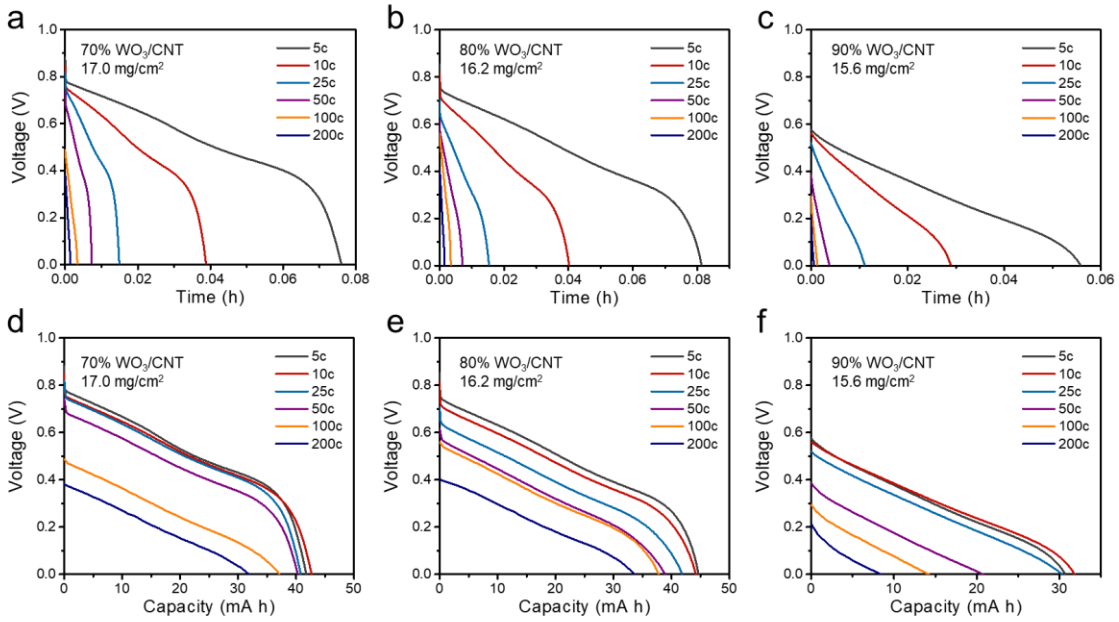

Figure 3-5. Galvanostatic discharge curves of WO_3-oxygen batteries made from WO_3 /CNT composites with WO_3 content of (a, d) 70%, (b, e) 80% and (c, f) 90%. Cells were charged to 0 V prior to the discharging.

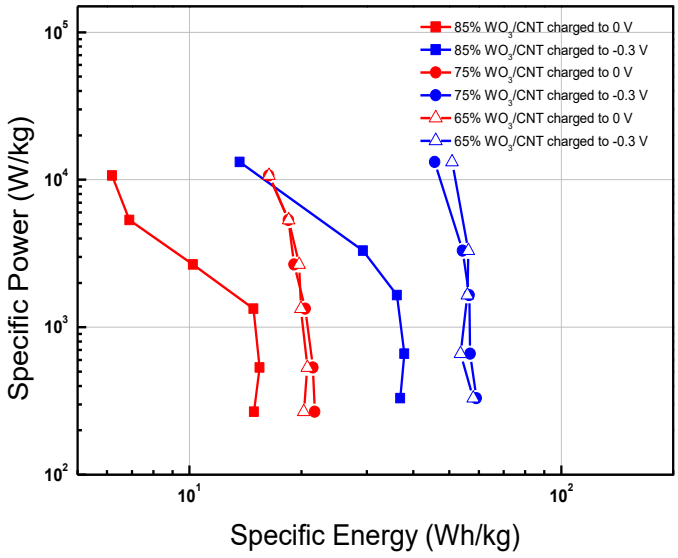

Figure 3-6. Ragone plots of the WO_3-oxygen batteries with different WO_3 content in the composites of WO_3 and CNT.

To further quantify the performance of the WO_3-oxygen batteries, Ragone plot of the supercapacitors is provided in **Figure 3-6**. As shown, supercapacitors fabricated with 80%WO_3/CNT and 70%WO_3/CNT samples (charged to -0.3 V) possess similar performance, with energy densities between 45 Wh/kg to 58 Wh/kg and power density up to 13 kW/kg. The performance of the supercapacitor is greatly improved through optimizing the ratio of WO_3 and CNT. The optimal weight ratio of WO_3 in the composite is determined to be 80% in this study.

The excellent electrochemical performance of WO_3 material in the WO_3-oxygen battery indicates the feasibility of WO_3 to be utilized in the fuel cell application. The intertwined network of WO_3 and CNT further improves the charge transport of the WO_3 electrode. The 80%WO_3/CNT composite was determined as the optimized sample.

3.3 Optimization of the structure and operating conditions of the hybrid cell

Two configurations of the PEMFC with the WO_3 electrode were proposed as shown in **Figure 3-7**. For the structure 1#, a separate layer of WO_3 takes place of microporous layer to coat on the carbon paper. The catalyst layer on the anode side is sprayed directly onto membrane. For structure 2#, the WO_3 material is mixed with Pt/C catalyst and coated onto carbon paper. Both cells were measured at 30 and 50 °C and compared with a conventional control cell. The WO_3 loading in the hybrid cell-1 and hybrid cell-2 are 4.8 and 5.2 mg cm^{-2} respectively.

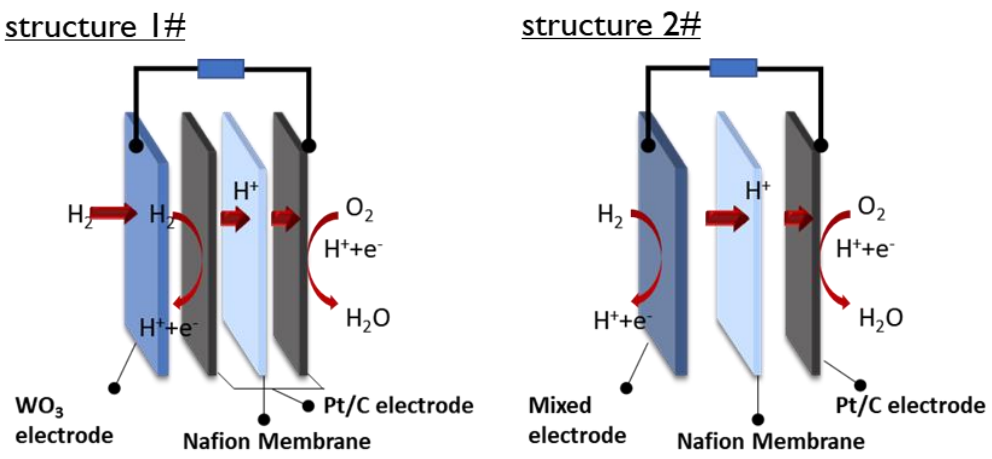

Figure 3-7. The configuration of two different MEA structures for the hybrid fuel cell.

Figure 3-8 shows polarization curves of hybrid cells. At 30 °C, hybrid cell-1 shows comparable performance with the control cell, the maxim power density can reach 1 W cm^{-2}. Surprisingly, the performance of hybrid cell-2 is much worse than other cells. The limiting current of hybrid $cell^{-2}$ is only 300 mA cm^{-2}, which is only 10% of the current density can be delivered by other two cells. When increasing temperature to 50 °C, all the cells show enhanced performance. The voltage of hybrid cell-1 is slightly lower than the control cell. Although performance increased, the power output of hybrid cell-2 is still far behind the other two cells.

The poor performance of hybrid cell-2 can be contributed to inefficient utilization of the catalyst. When same amount of Pt/C catalyst used in the anode for all the cells, the hybrid cell shows severe voltage loss in the low current region, indicating the catalytically active surface area in hybrid cell-2 is much less than the other cells. Furthermore, for hybrid cell-2 the Pt/C particles are dispersed in the thick WO_3 layer rather than directly placed on the membrane. Once the H_2 dissociate on the Pt, protons have to transport through the WO_3

layer and membrane to react with O_2 at the cathode. The much longer diffusion length causes the increasing of the series resistance. Therefore, the first configuration of the hybrid cell is chosen for the following study.

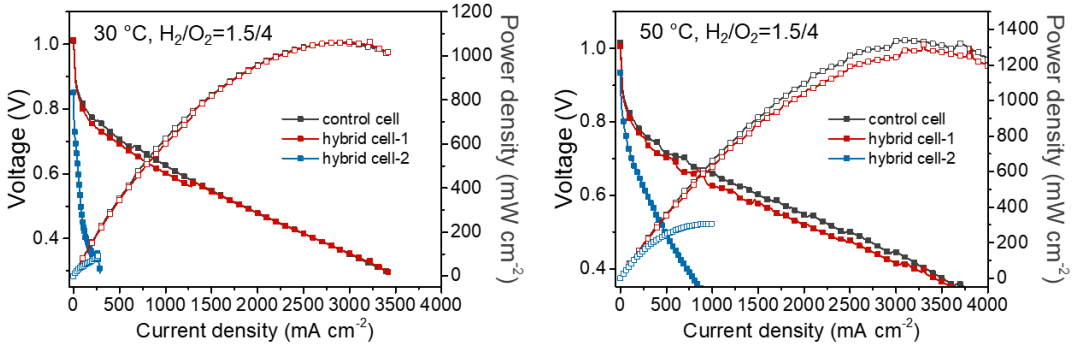

Figure 3-8. Polarization curves of the control cell and hybrid cells with different MEA structures measured at 30 and 50 °C.

The incorporation of the energy storage electrodes may also increase the series resistance, which deteriorates the power performance. It is therefore necessary to optimize the loading of the WO_3 to ensure effective fuel cell performance and response capability.

Figure 3-9 shows the polarization curves of these devices at different operating temperatures. **Figure 3-9**(a) shows the performance of a control cell, which is enhanced when temperature is increased from 30 °C to 50 °C. The performance of the cell remains similar when the temperature further increased to 80 °C. The hybrid PEMFCs show similar behavior when the temperature is increased from 30 °C to 50 °C. With the temperature increased to 80 °C, the performance of the hybrid PEMFCs with WO_3 loading 4.8 mg/cm^2 and 14.3 mg/cm^2 drops when the discharging current density is higher than 2500 mA/cm^2.

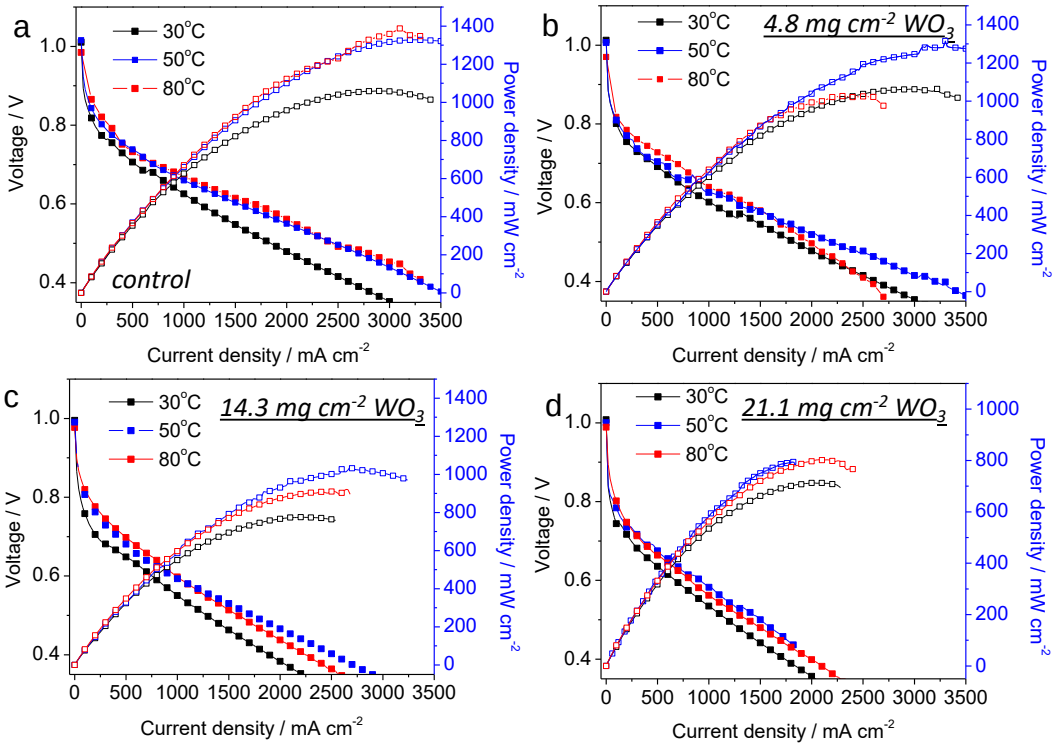

Figure 3-9. Influence of temperature on the performance of control PEMFC (a) and hybrid PEMFC with different WO_3 loadings of 4.8 mg cm^{-2}(b), 14.3 mg cm^{-2}(c) and 21.1 mg cm^{-2}(d). The anode was fed with 100 mL min^{-1} H_2. The cathode was supplied with 100 mL min^{-1} O_2.

Operation temperature affects the reaction kinetics, proton conductivity, and gas diffusion of the devices. Increasing the temperature from 30 °C to 50 °C favors faster reaction kinetics, proton conduction and gas diffusion, which lead to improved device performance. Further increasing temperature to 80 °C should further increase the reaction kinetics and transport kinetics. However, it was found that the performance at 80 °C is similar to that at 50 °C. This may be attributed to the reduced degree of saturation of the feeding gas, which retards the transport of protons. As a result, the performance of the device remains similar as that operated at 50 °C. For the hybrid devices, similar trend was

observed. The dropping performance observed at 80 °C and at high discharge current density is possibly due to the decreased proton conductivity.

The polarization curves of hybrid PEMFCs with different WO_3 loadings at different operating temperatures are shown in **Figure 3-10**. At 30 °C, the cell with 4.8 mg/cm^2 WO_3 loading shows similar performance with that of the control cell. With increasing WO_3 loadings, the corresponding peak power densities of the hybrid PEMFCs decreases from 1059, 776 and 715 mW cm^{-2} for WO_3 loading of 4.8, 14.3 and 21.1 mg cm^{-2} respectively. The hybrid PEMFC with a low WO_3 loading of 4.8 mg cm^{-2} could achieve performance comparable to the control cell (i.e., at 30 and 50 °C), which is possibly attributed to the reduced electrode thickness and series resistance compared with electrodes of higher WO_3 loadings. The cells exhibit improved power density with increasing temperature to 50 °C; the effect of the WO_3 loading on the performance is similar as that in 30 °C.

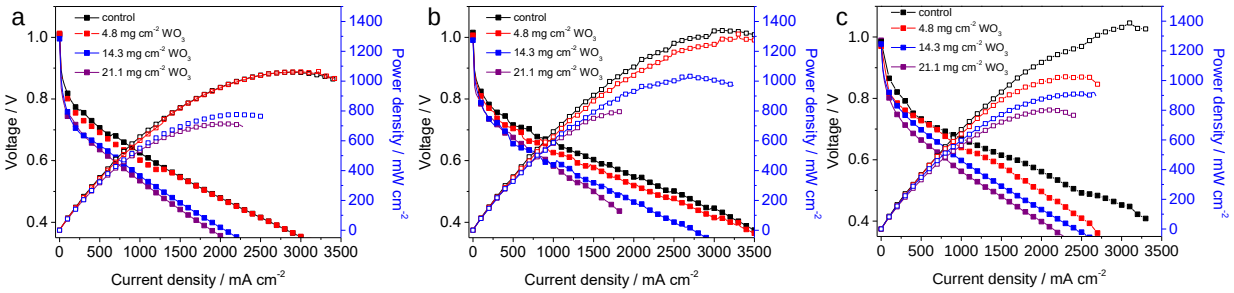

Figure 3-10. Influence of WO_3 loadings on the performance of hybrid PEMFCs at operating temperatures of (a) 30, (b) 50 and (c) 80 °C. The anodes were fed with 100 mL min-1 H_2. The cathode was supplied with 100 mL min^{-1} O_2.

3.4 Conclusions

The feasibility of WO_3 material in the PEM fuel cell application was proved by the WO_3-O_2 battery experiment. 80% WO_3/CNT composite shows excellent electrochemical

performance in the fuel cell configuration. After optimization of the MEA structure and the cell operating conditions, the hybrid fuel cell with WO_3 loading of about 5 mg cm^{-2} exhibits comparable performance with the conventional fuel cell.

3.5 Experimental methods

3.5.1 Fabrication of WO_3 electrodes and MEAs

WO_3 electrode on carbon paper:

The WO_3/carbon composites were assembled onto carbon paper (Toray TGH-060) current collector. Briefly, 90% of the WO_3/carbon composite, and 10% Nafion dispersed in ethanol were mixed to form slurries. The homogenous slurries were sprayed on the carbon fiber paper.

MEA fabrication for WO_3-oxygen battery

As illustrated in **Figure 3-11**, Nafion® 212 membranes were used as the ion conducting layers. To prepare catalyst layer of the cathode, a homogeneous ink was formed from the desired amount of commercial Pt/C(40 wt%, JM) and the Nafion solution with ethanol as solvent. The ink was deposited on the membrane by spraying procedure. The Pt loading in the cathode was 0.4 mg cm^{-2} for all the MEAs. The MEAs were made by sandwiching catalyst coated membrane between WO_3 electrode and one gas diffusion layer (GDL), and then applying a pressure of 20 MPa for 2 min at 130 ^oC.

Fabrication of fuel cells

Catalyst ink was prepared by ultrasonically blending a commercial Pt/C catalyst (40 wt.% Pt, JM) with a Nafion solution (5 wt.%, Dupont) and ethanol for 2 h, which was sprayed onto both sides of the proton exchange membranes (Aquivion® R79-02S) with a Pt loading of 0.05 mg cm^{-2} and 0.4 mg cm^{-2} in the anode and cathode, respectively. Hybrid

MEAs were fabricated by sandwiching the catalyst-coated membranes between a WO_3 composite electrode and a prefabricated GDL, and then hot-pressed together at 130 ºC under 0.1 MPa for 1 min. Control MEAs were fabricated using a GDL with microporous layer instead of the WO_3 electrode at the anode side.

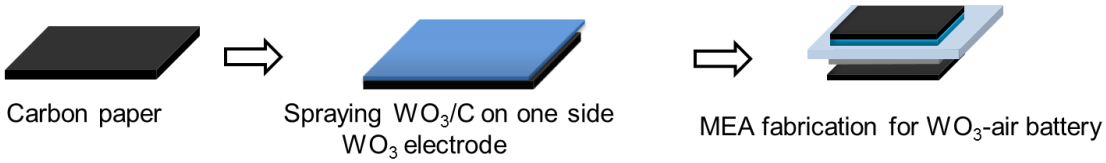

Figure 3-11. Fabrication process of MEA for the WO_3-oxygen battery.

3.5.2 Measurements of WO_3-O_2 battery and PEM fuel cells

Electrochemical measurements of the WO_3-O_2 battery were carried out on a Solartron 1860/1287 Electrochemical Interface (Solartron Analytical). The charging process was conducted by supplying the Pt/C cathodes with hydrogen (0.1 L min^{-1}) and the WO_3 anode with nitrogen (0.1 L min^{-1}). The cells were charged to 0 V (*vs.* DHE) using a constant current of 0.2 A g^{-1}. The inlet gas of cathode was then switched to oxygen (0.1 L min^{-1}). The cells were discharged at different rates.

Steady-state performance of PEM fuel cells were measured in a 5 cm^2 single cell at 30 °C, 50 °C and 80 °C using fuel cell test stations (Fuel Cell Technologies, Inc.). The anodes were fed with H_2 at a stoichiometry of 1.5. The cathode was supplied with O_2 at a stoichiometry of 4. The fuel (hydrogen) and the oxidant (oxygen) were humidified by bubbling through distilled water to achieve 100% humidity. The cell resistance was measured by a current interrupt technique during steady-state and dynamic response tests.

Chapter 4. Transient Performance and Lifetime Test of the Hybrid Fuel Cell

4.1 Introduction

PEMFCs rely on continuous electrochemical reactions of hydrogen and oxygen, which involve fuel transport, disassociation of hydrogen into electrons and protons, transport of electrons and protons, and their subsequent reactions with oxygen in cathodes that produce water and generate power. The transport of fuel is related to cell architecture, fuel-flow control, water and heat management, and other factors.[107-109] Fuel starvation often occurs during transient operation, which not only deteriorates power output, but also shortens the lifetime.[62, 110-112] Even with a sufficient supply of hydrogen, a delayed supply of protons also occurs in order to meet high-power demand, resulting in transient polarization that causes power-output delay lasting up to tens of seconds.[112] In addition, during the start-up process, oxygen diffused from cathodes to anodes increases anode potential and triggers degradation of cathodes, further shortening the lifetime of PEMFCs.[113-115]

Regardless of fuel starvation of start-up, the origin of the performance degradation is the rising of the anodic overpotential. Once the anodic potential increases, side reactions will occur at anode or the cathodic potential will also rise, ultimately led to the failure of the cell. We envision that PEMFCs with significantly enhanced transient performance and prolonged lifetime could be made by integrating anodes with a thin layer of tungsten oxide (WO_3). **Figure 4-1** illustrated our design, which adapts a traditional membrane-electrode-assembly (MEA) architecture that comprises two gas diffusion layers (GDLs), two Pt/carbon catalyst layers, and a proton exchange membrane. In the anode, a thin layer of

WO_3 with a hexagonal crystalline structure is integrated between the GDL and the Pt/carbon catalyst layer. Hexagonal WO_3 is a highly stable proton-electron mixed conductor, of which a high capacity of protons could be stored in a highly reversible and rapid manner at -0.4 to 0.6 V *vs.* reversible hydrogen electrode in an acidic environment.[116-117]

During a normal operation, H_2 passes through the GDL and the WO_3 layer, and is converted to protons and electrons in the catalyst layer (Reaction **i**). The protons and electrons are then transported crossing the proton-exchange membrane and external circuit, respectively, reacting with O_2 in the cathode in a manner similar to that of the traditional PEMFCs (Pathway **1,** Reaction **ii**). As-generated protons and electrons also react with the WO_3 and are stored in the form of H_xWO_3 (Pathway **2,** Reaction **iii**). In response to fuel starvation or high-power demand, H_xWO_3 is converted back to WO_3, releasing electrons and protons to compensate the fuel shortage (dash lines, Pathway **3**). The WO_3 layer is then recharged spontaneously through the Reaction **iii**, reloading with electrons and protons for the next compensating cycle. In addition, H_xWO_3 also reacts with O_2 diffused to the anode, forming WO_3 and H_2O (Reaction **iv**). Such O_2 scavenger stabilizes anode potential, protecting the cathodes from degradation and prolonging the lifetime of PEMFCs. Moreover, hydrogen-disassociation reaction (**i**) occurs with low activation energy. As described by the Butler-Volmer equation, the rate of disassociation increases proportionally to (at low overvoltage) or exponentially with the anode overvoltage (at high overvoltage).[118] In response to power demand, discharge of the WO_3 layer increases anode potential and promotes the disassociation reaction, providing more protons to avoid the power-output delay. In this context, the WO_3 layer not only serves as a rapid-response

hydrogen reservoir and oxygen scavenger, but also constitutes a regulator for hydrogen-disassociation reaction, dynamically modulating anode overvoltage and disassociation of hydrogen according to power demand.

In this chapter, the stabilizing function of WO_3 layer to the anode potential will be validated using a H_2 pump cell first. Then the transient performance, durability and the lifetime of the hybrid cell will be measured.

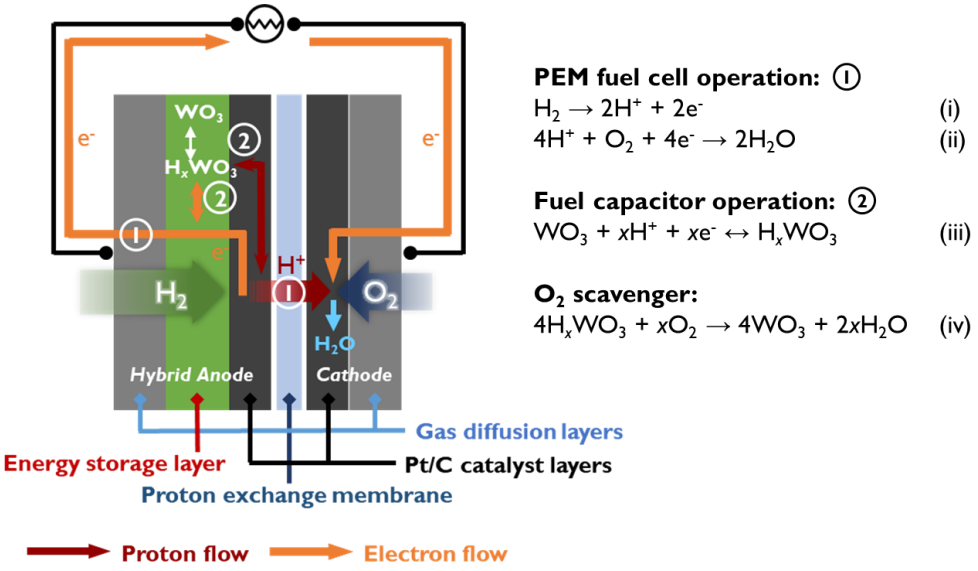

Figure 4-1. Schematic of a membrane electrode assembly (MEA) for the hybrid PEMFC with a WO_3-based multifunctional anode.

4.2 kinetic study of the hybrid cell

The overpotential of the anode was investigated by the H_2 pump test. The H_2 pump cell was assembled by a WO_3/CNT electrode, a carbon electrode, and catalyst-coated membrane. The catalyst loadings of two sides were both 0.5 mg cm^{-2}. One electrode operates as the working electrode while the other serves as the counter electrode. By simply swapping the working and counter electrodes, a single cell can be used to measure both the

hybrid electrode (with WO_3/CNT) and a control electrode (only Pt/C) with minimal interference.

The H_2 pump test was conducted at 30 °C, with H_2 flow rates of 10 and 20 mL min^{-1} at working electrode and counter electrode, respectively. The feeding gases were humidified at 35 °C to keep the electrolyte membrane from drying out. The current was scanned at different sweep rates. The measurement was terminated when the voltage of the cell was higher than 0.3 V in order to protect the cell. The conventional Pt/C electrode and the hybrid electrode were tested using the same cell by reversing the connecting of electrodes.

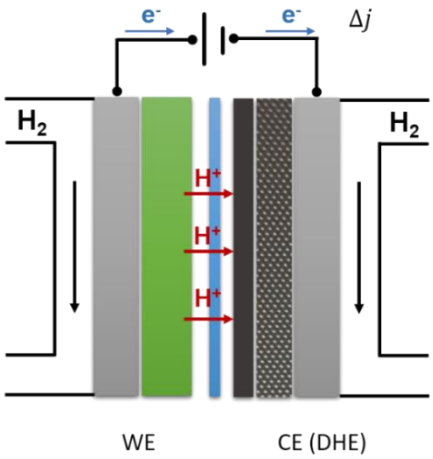

Figure 4-2. Schematic diagram of the H_2 pump cell.

Assuming minimal polarization of the counter electrode in the presence of excessive H_2, the voltage of the cell under designed current is considered as the overpotential of the working electrode. The polarization curves of the hybrid electrode and Pt/C electrode is shown by solid and dash lines, respectively (**Fig. 4-3**(a)). The overpotential increases linearly with the current density until reaching the limiting current;

over certain point the overpotential rapidly increases to 0.3 V. At a sweep rate of 1 mA s^{-1}, the limiting current of the Pt/C electrode is 120 mA cm^{-2}, while the hybrid electrode can output a maximal current density of 200 mA cm^{-2}. At higher sweep rate of 10 mA s^{-1}, the hybrid electrode can even afford a high limiting current of ~ 400 mA cm^{-2}. This also indicates that hybrid electrode can deliver much higher energy compared with control electrode before termination of the test (**Fig. 4-3**(b)).

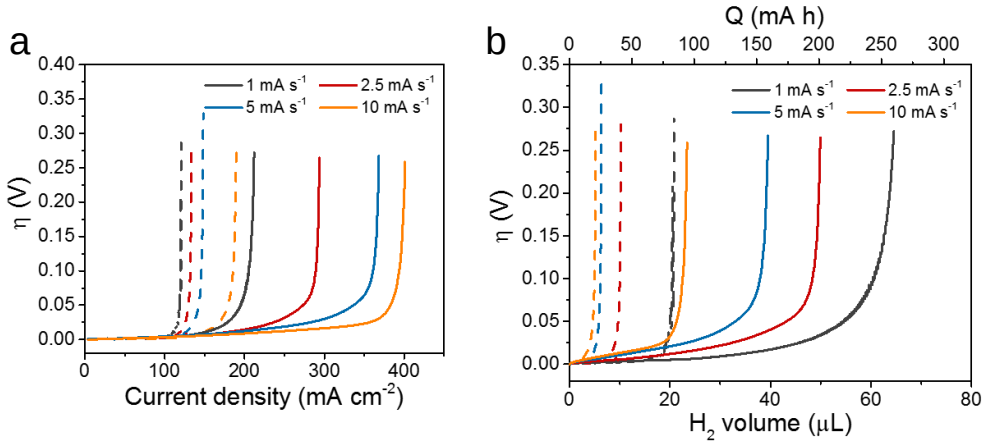

Figure 4-3. (a) The potential-current curves (iR corrected) and (b) equivalent energy of the hybrid electrode and the Pt/C electrode under different current scan rates at 30 °C.

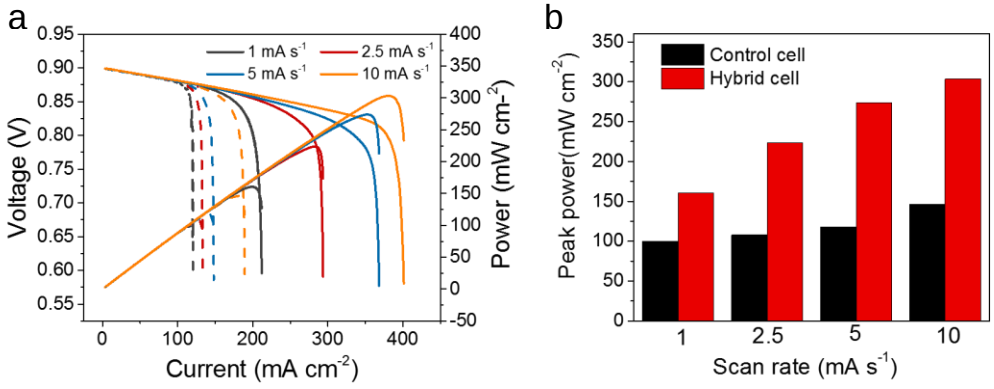

Figure 4-4. (a) Simulated polarization curves of hybrid and control fuel cells assuming a constant cathodic potential of 0.9 V and (b) corresponding peak power at different scan rates.

Under a given flow rate of H_2 fuel, the hybrid electrode can afford a higher current density; in other words, the hybrid fuel cell can deliver a higher peak power before fuel starvation occurring, as shown in **Fig. 4-4**(a). Specifically, the peak power of the simulated hybrid cell is over 50-100% excessing that of control cell (**Fig. 4-4**(b)). Such capability enables the hybrid electrode to operate at a higher current density compared with control cell under identical fuel flow rate. As shown in **Figure 4-5**(a), under an output of 160 mA cm^2, the overpotential of the Pt/C electrode reaches 0.3 V in 300 s due to fuel starvation. In comparison to the control electrode, the potential of the hybrid electrode is less than 30 mV at 600 s. The results suggest that during the occasion of H_2 starvation, the hybrid electrode with WO_3/CNT can maintain a low overpotential of the anode for a longer time. After ending the test, the open circuit potentials (OCV) of both electrodes recover to ~ 0 V in ~ 5 s (**Figure 4-5**(b)), suggesting the recharging process of WO_3/CNT should also be less than 5 s.

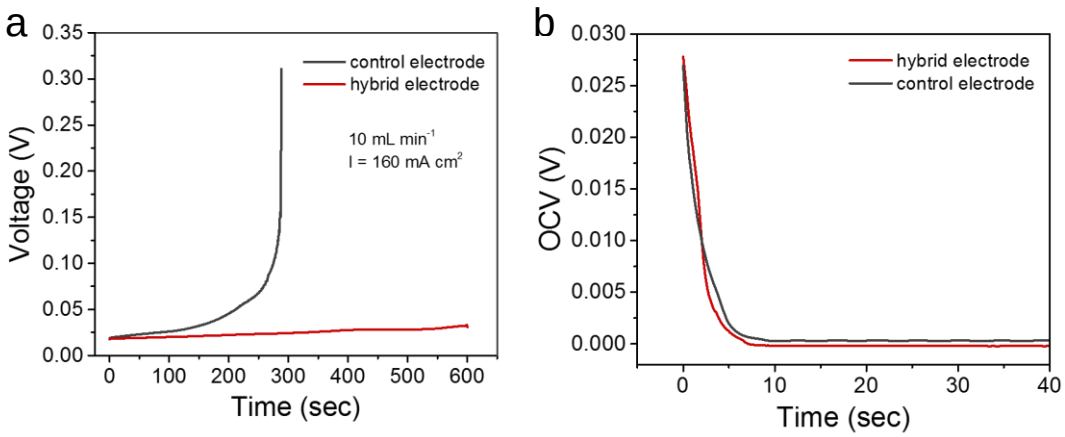

Figure 4-5. (a) The potential-time curves of the hybrid electrode and the Pt/C electrode under a current density of 160 mA cm^2 at 30 °C and (b) OCV of both electrodes after ending the test.

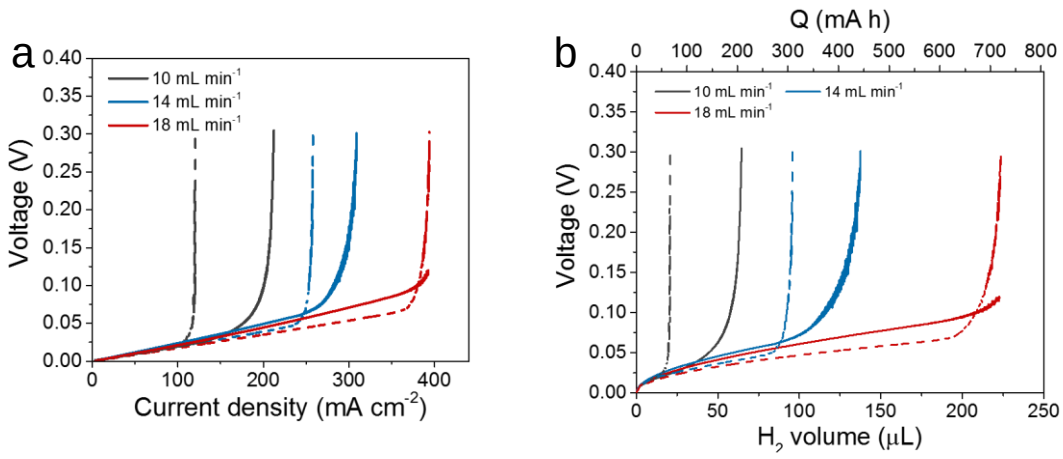

Figure 4-6. (a) The potential-current curves and (b) equivalent energy of the hybrid electrode (solid) and the control Pt/C electrode (dash) under different current scan rates at 30 °C. Red solid line ends when reaching the current limit of the instrument.

As expected, the limiting current is highly related to the flow rate of H_2, i.e., the supply of fuel (**Figure 4-6**). As the H_2 flow rate increases, hybrid electrode always delivers higher limiting current density than control electrode. Considering the identical fuel supply condition, a higher limiting current is equivalent to a higher utilization ratio of H_2 fuel, which is crucially important for practical fuel cell device. The capability of the hybrid electrode to sustain higher current can be translated into the capability to deliver higher power output of the hybrid fuel cell under the dynamic working condition, which is attributed to the energy storage capability of WO_3/CNT and synergic effect between WO_3 and Pt catalyst.

4.3 The durability of fuel cell against fuel starvation

The H_2 starvation tests were performed as following: the cell was discharged at a constant current density of 200 mA cm^{-2} for 210 s using the external direct-current power source (1287A Potentiostat Galvanostat) at an operating temperature of 50 ^oC. At the end

of the 200 s, the H_2 supply was turn off by a three-way valve and the anode was purged with N_2. The cell voltage was recorded against time as shown in **Figure 4-7**. It was observed that the control cell voltage rapidly dropped to the negative value followed a steady decrease with time. The results indicate the cell reversal occurs when the anodic potential increases and becomes more positive than the cathodic potential. Carbon oxidation as well as water electrolysis might occur as a result of H_2 starvation, leading to ultra-high anode polarization. Comparatively, the cell with WO_3 layer show a much smaller decay rate of the cell voltage than the control cell since the charged WO_3 could release the stored protons and electrons when the hydrogen was exhausted.

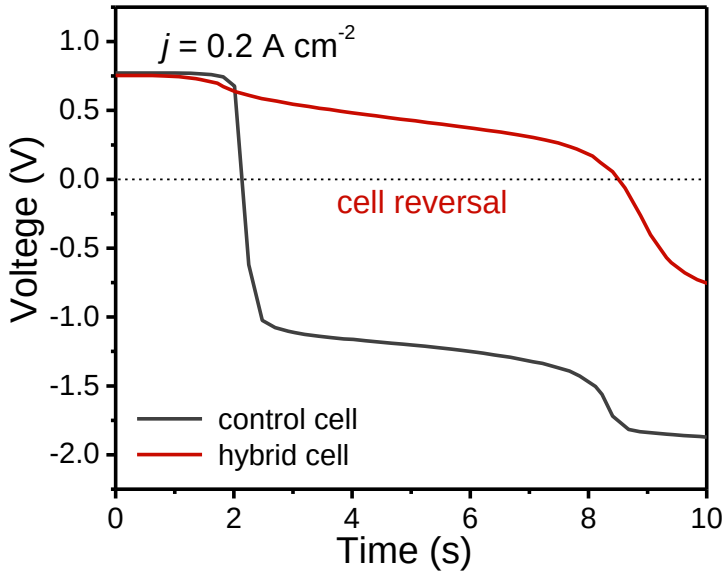

Figure 4-7. The time dependent changes of cell voltage during the H_2 starvation experiment.

Figure 4-8 shows the I-V curves of the control cell and the cell with WO_3 after different experimental periods during the H_2 starvation tests. The peak power density of

the control cell decreased by 12.7% after the first H_2 starvation test and continued dropping by 46.9% after the second H_2 starvation test. In contrast, the cell with WO_3 layer exhibit ultra-high stability with almost no degradation of the performance. The typical TEM images of the anodic catalyst samples from the two cells are displayed in **Figure 4-9**. A severe aggregation of the platinum nanoparticles is observed for the control cell, while the catalyst nanoparticles distributed uniformly on the carbon support of the cell with WO_3 layer. The results suggest that WO_3 layer functions as a buffer layer that could effectively alleviate the anodic polarization and protect the electrocatalysts from degradation.

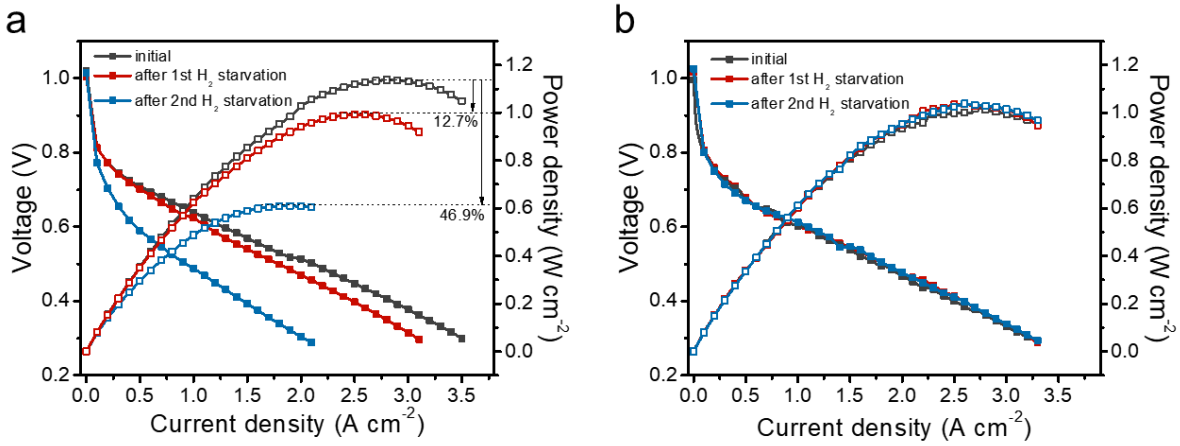

Figure 4-8. The change of I-V performance of (a) the control cell and (b) the cell with WO_3 layer before and after H_2 starvation tests.

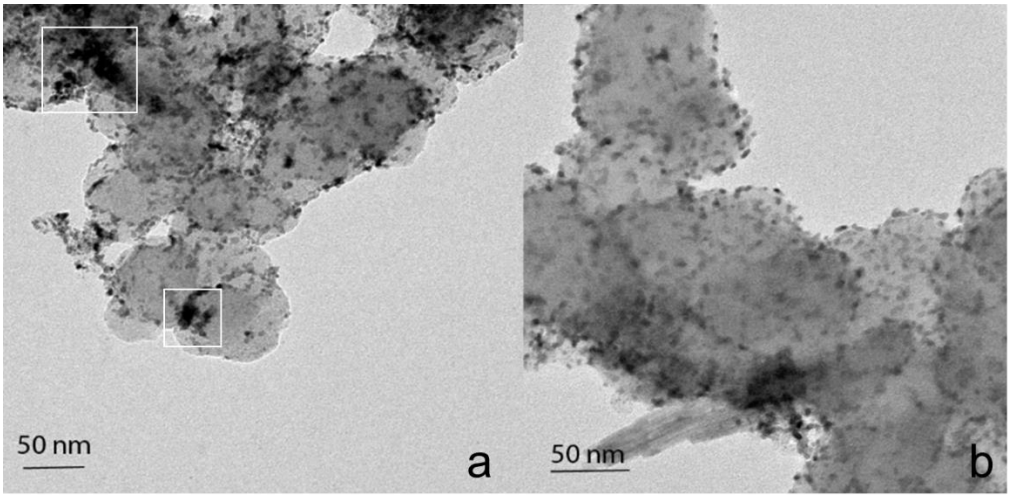

Figure 4-9. Typical TEM images of the anodic electrocatalysts from (a) the control cell and (b) the cell with WO_3 layer after the H_2 starvation tests.

4.4 The durability of fuel cell against start-up process

Previous studies have shown that the formation of hydrogen/air boundaries during unprotected start-up and shut down process will cause extremely fast degradation to the cathodic electrocatalysts and consequently decrease the life time of fuel cells. To simulate this operating condition, the cells were maintained at a constant voltage of 0.8 V for a period of 220 s. At the end of 200 s, the H_2 supply was cut off by a three-way valve and an air flow of 20 mL min^{-1} was introduced to the anode. I-V curves were recorded after every simulated start-up process. The output current of cells were recorded during tests as shown in **Figure 4-10**.

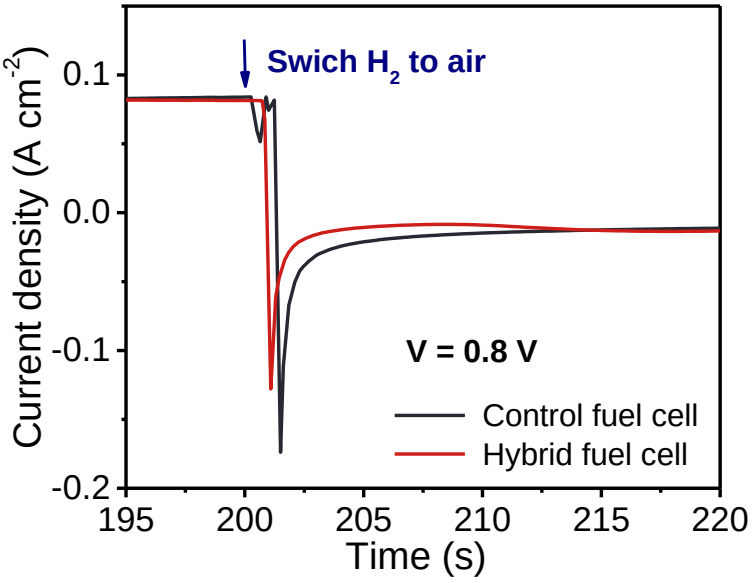

Figure 4-10. The time dependent changes of current density of cells during the start-up experiment.

The change of I-V performance of the control cell and the hybrid cell with WO_3 layer before and after start-up tests were shown in **Figure 4-11**. The performance of the control cell decreases gradually with repeated start-up tests. In contrast, the cell with WO_3 layer exhibits overlapped IV-curves. The potential distribution and the possible involved reactions during the start-up tests for the control cell and the cell with WO_3 layer are proposed as displayed in **Figure 4-12**. It can be seen that, during the formation of the hydrogen/air boundry at the anode, the partitial potential at the cathode would be as high as 2.0 V, leading to carbon corrosion and electrocatalysts degradation. However, with intergrating the WO_3 layer into MEAs, the air in the anode would react with the charged WO_3 and thus be consumed.

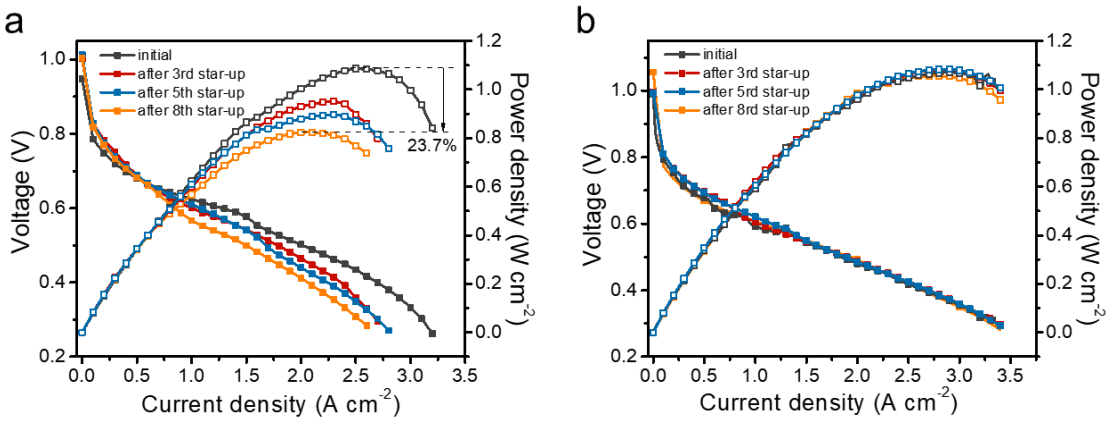

Figure 4-11. The change of I-V performance of (a) the control cell and (b) the cell with WO_3 layer before and after start-up tests.

As shown in **Figure 4-13**, once the air intrused into anodic compartment, the voltage of control cell drops rapidly. Considing the test cell as a air-contained region in a large cell, as the region (3) shown in **Figure 4-12**, when the cell was underwent a careless start-up process, reverse current was detected. On the other hand, the anode potential of the hybrid cell was more stable and no reverse current occurred duringn strat-up. The improved durability against start-up process could attribute to the WO_3 layer that eliminates formation of the hydrogen/air and maintains the anode at a low overpotential.

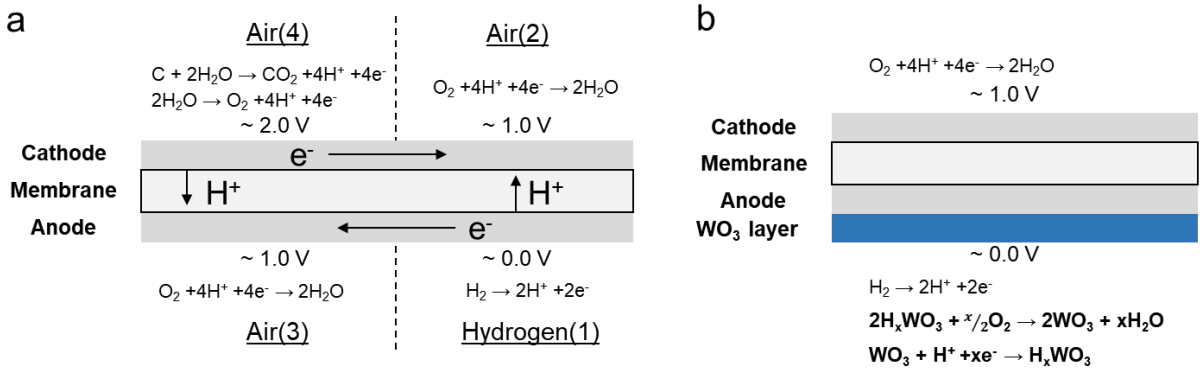

Figure 4-12. The potential distribution and the possible involved reactions during the start-up tests for (a) the control cell and (b) the cell with WO_3 layer.

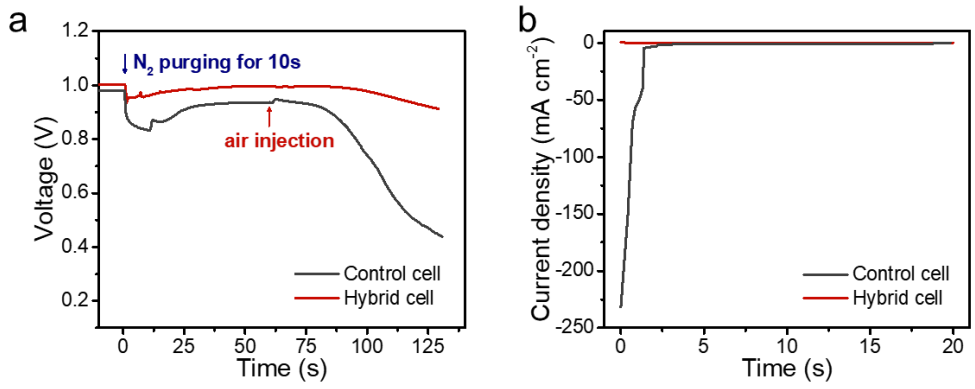

Figure 4-13. Change of the cell voltage during the oxygen intrusion tests.

4.5 The durability of fuel cell against load cycling

To investigate the dynamic response capability, both hybrid cell and control cell operating at constant current of 50 mA cm^{-2} suddenly jump to high current outputs of 2, 3 and 4 A cm^{-2} with H_2 stoichiometry of 1.5. At 30 °C, notable undershoot of voltage is observed in control fuel cell, which is more severe at higher current density (**Figure 4-14**(b)). In a sharp contrast, hybrid cell shows flat voltage profile with no observable undershoot at all of the testing currents. Although both cells deliver similar steady-state power output, voltage undershoots in control fuel cell during the transient period of a few tens of seconds result in significant delay of output power. **Figure 4-14**(c) shows the extra power output delivered by hybrid cell compared with control cell, and the average extra power during a given transient period is further summarized in **Figure 4-14**(d). For example, hybrid cell offers average extra power of 276, 210, 179, 160 mW cm^{-2} over 5, 10, 15 and 20 s, respectively, when jumping to 4 A cm^{-2}. In other words, during the first 5 s of the transient period, hybrid cell provides ~ 23% extra power over control cell at maximal power output.

At an elevated temperature of 50 °C, similar phenomenon of improved dynamic performance is also observed for hybrid cell. Minor undershoot of the hybrid cell might be related to the water management as noted in the polarization curve (see **Figure 4-15**(a)), which would be addressed by optimizing electrode structure and/or operation condition in the future. Despite the less severe undershoot of control cell due to improved mass transport at 50 °C, hybrid cell can still maximally deliver ~ 68 mW cm^{-2} extra power during the first 5 s of transient period (**Figure 4-15**(c) and (d)).

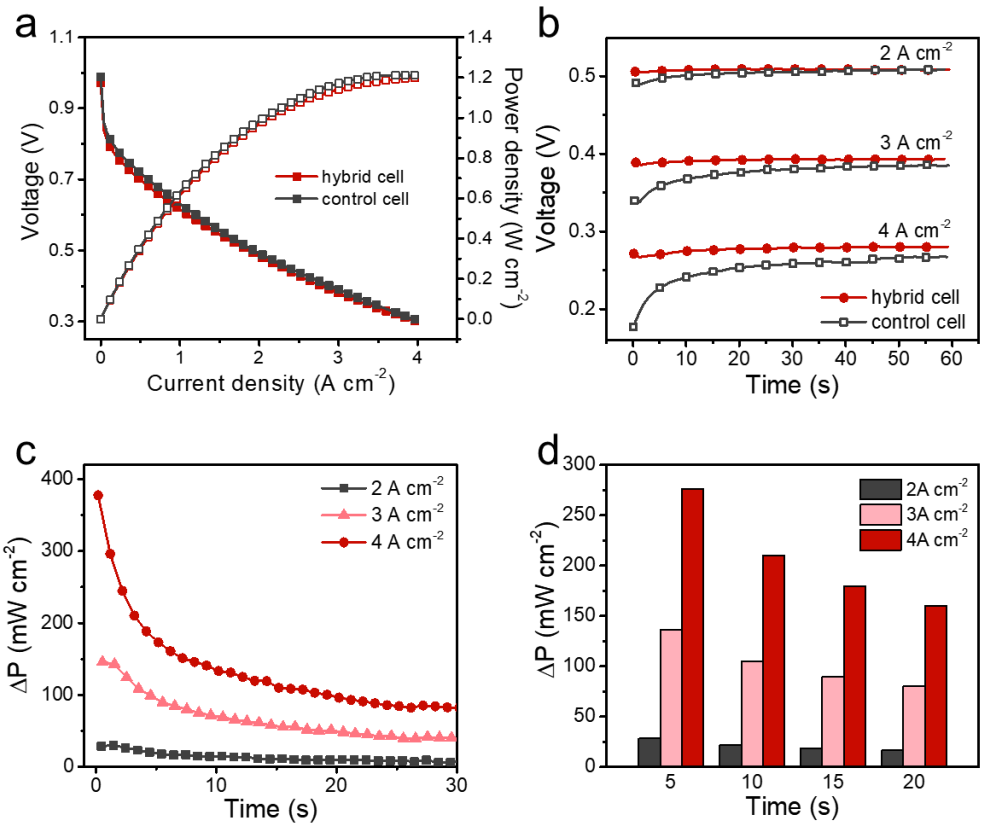

Figure 4-14. (a) Polarization curves of the hybrid cell and control cell at 30 °C; (b) The voltage and power of the control cell and the hybrid cell in response to increasing current outputs from 0.05 A cm^{-2} at 30 °C; (c) The difference of power density delivered by the hybrid fuel cell and the control cell (ΔP) in response to an increase of current density at 30 °C; (d) The average ΔP delivered at a time scale of 5 s, 10 s, 15 s, and 20 s, respectively at 30 °C.

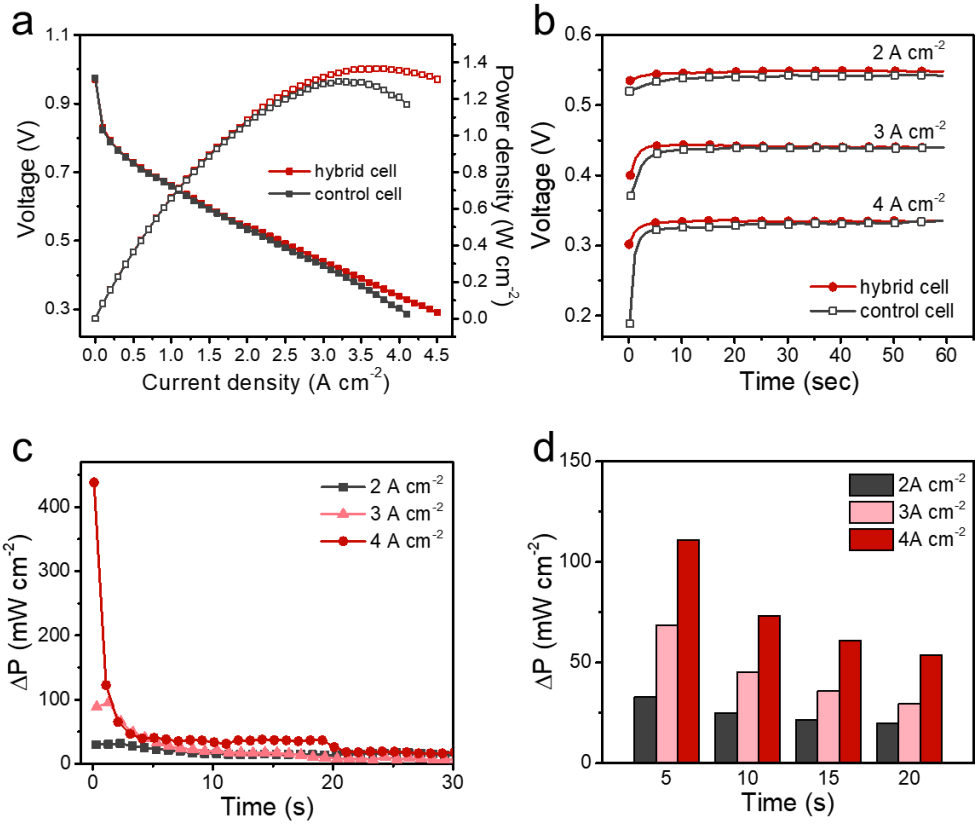

Figure 4-15. (a) Polarization curves of the hybrid cell and control cell at 50 °C; (b) The voltage and power of the control cell and the hybrid cell in response to increasing current outputs from 0.05 A cm^{-2} at 50 °C; (c) The difference of power density delivered by the hybrid fuel cell and the control cell (ΔP) in response to an increase of current density at 50 °C; (d) The average ΔP delivered at a time scale of 5 s, 10 s, 15 s, and 20 s, respectively at 50 °C.

To further simulate the acceleration and deceleration process in vehicles, the cells were subjected to oscillating current output between 50 mA cm^{-2} and 1000 mA cm^{-2} with a holding time of 30 s and 120 s, respectively. Previous results have shown the active surface area of fuel cell electrocatlyst decreases faster when the potential varies in compasion to constant potential. Moreover, under dramastic loading changes, corrosion of the carbon support due to fuel starvation can also acclerate the aggragation of the

electrocatlayst particles, which will ultimately lead to the loss of the performance. The I-V performance of the cells during different cycles were recorded as shown in **Figure 4-16**. In comparison to the decayed I-V curves with cycles for the control cell, the hybrid cell again exhibits unchanged I-V curves, demonstrating the improved durability.

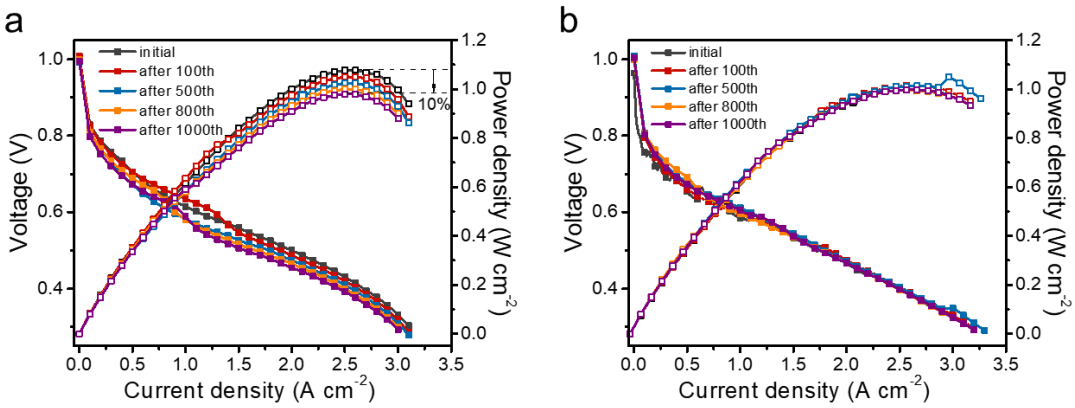

Figure 4-16. The change of I-V performance of the control cell (a) and the cell with WO_3 layer (b) before and after load cycling tests.

4.6 Long Cycle

To further evaluate the performance and lifetime of cells operating under conditions close to the real-world circumstance of automotive applications, the endurance tests were carried out following the EU harmonised test protocols for PEMFC-MEA testing in single cell configuration. These protocols are set out by the Joint Research Center, the European Commission's in-house service in aim to provide a testing methodology to enable a fair comparative assessment of the performance of MEAs under operating conditions foreseen in future automotive applications. This methodology focuses on the stressors related to "operating conditions" and "load cycling" which exert on the MEA performance in single cell configuration.

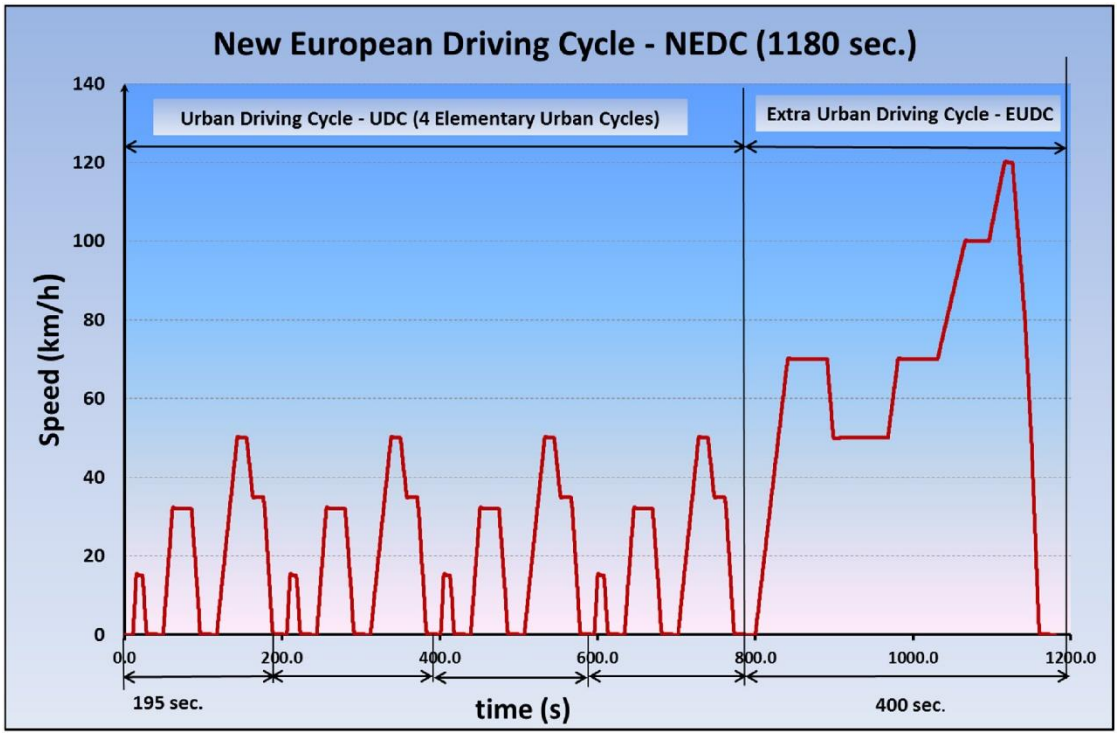

Figure 4-17. NEDC profile according to EU directive 98/69/CE.

The "load cycling" in this methodology is designed to simulate varying power demands during vehicle operation. The load cycle is used to assess fuel cell durability during a relatively long period by exposing the cell to the same load cycle repetitively. The fuel cell cycle is based on the "New European Driving Cycle" (NEDC) displayed in **Figure 4-17**. The NEDC cycle is used for type approval of light-duty vehicles and features periods of acceleration, deceleration and constant speed. It consists of four repetitions of a low speed urban cycle of 195 seconds each followed up by a part which simulates a highway driving cycle of 400 seconds duration. That is equivalent to a theoretical distance of approximately 11 km driven in about 20 min.

In aim to reproduce the NEDC cycle on the fuel cell test benches, the speed profile is transformed to the current profile for a PEM single fuel cell as shown in **Figure 4-18**,

which is called thereafter the Fuel Cell Dynamic Load Cycle (FC-DLC). The current density ratio is defined as the ratio of current density to maximum current density of the testing PEMFC single cell.

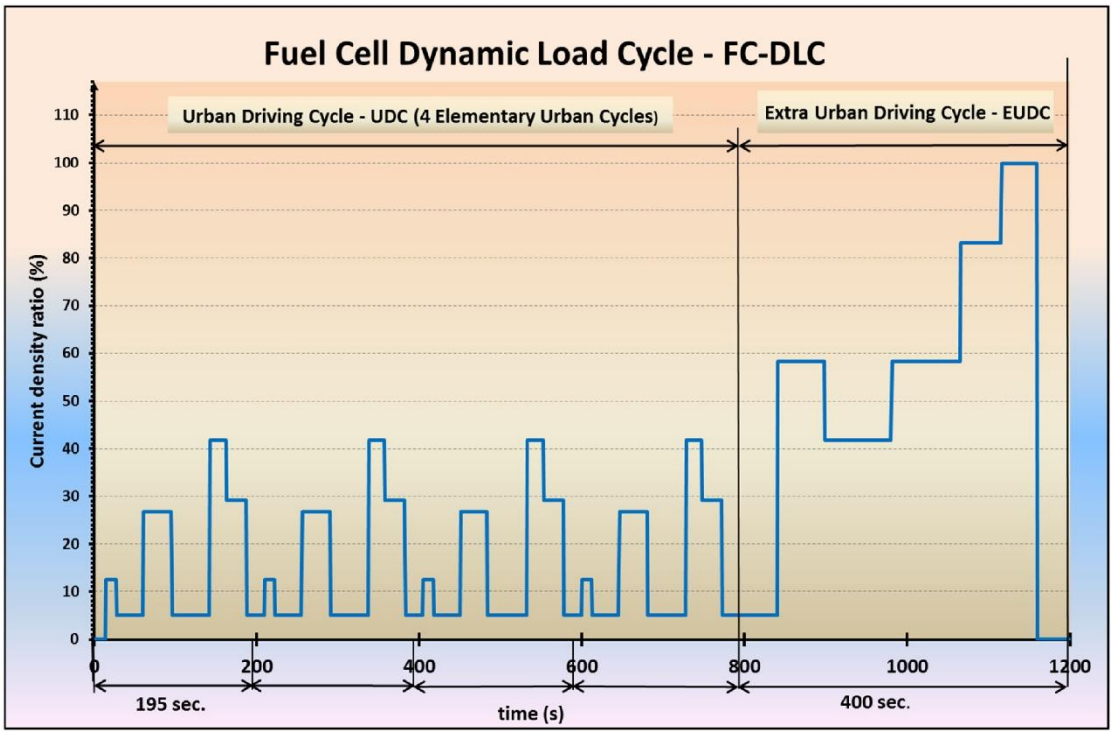

Figure 4-18. Fuel cell dynamic load cycle.

The dynamic load cycling endurance test comprises a total of 1400 cycles which correspond to one year of usual vehicle use equivalent to approximately 15,400 km of driving. The test is divided into 28 test blocks, for each test block containing 50 consecutive cycles. At the beginning and the end of each test block, polarization curves and the cell voltage at 0.1, 0.8 and 1.8 A/cm^2 are recorded to observe and evaluate the degradation of the cell. The cell voltages at 0.1, 0.8 and 1.8 A/cm^2 are representative for activation polarization losses at the kinetic regime, ohmic resistance losses at the linear regime, and concentration polarization at mass transfer limitation regime respectively.

A set of the control cell and the hybrid cell were assembled for the endurance testing. The WO_3 loading on the anode of the hybrid cell was 5.34 mg/cm^2. The operating temperature of the testing was set to 50 °C according to the previous results of the optimization of operating conditions. The initial performance of the cells was evaluated by the polarization curve measurements as shown in **Figure 4-19**. These two cells display comparable capability at the kinetic regime and the linear regime. The hybrid cell shows a slightly lower voltage at high current densities owing to the more significant gas diffusion resistance at the anode.

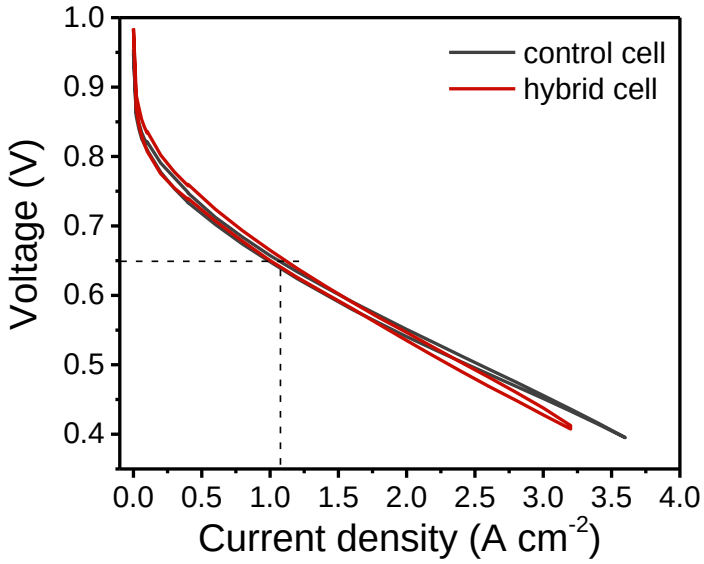

Figure 4-19. Polarization curves of the control cell and the hybrid cell before conducting the endurance testing.

The 100% current density of the cell to be used in the following endurance testing is defined by the average current density of the ascending and descending polarization curve measurements to yield a cell voltage of 0.65 V. Based on plots in **Figure 4-19**, the 100% current load value is 1.1 A/cm^2 for both cells. After determined the initial

performance and the 100% current density of testing cells, the two cells were started to run the fuel cell dynamic cycle as defined in **Table 4-1**. Between each test block, the testing cell was shut off and cooled down to ambient temperature. The cell was kept under ambient conditions for about 16.5 hours being equivalent to the total duration of consecutive 50 FC-DLC.

Table 4-1. The fuel cell dynamic cycle test points time/ load.

Step	Time (sec)	Dwell (sec)	Load (%)	Step	Time (sec)	Dwell (sec)	Load (%)
1	0	15	0.0	19	486	47	5.0
2	15	13	12.5	20	533	20	41.7
3	28	33	5.0	21	553	25	29.2
4	61	35	26.7	22	578	22	5.0
5	96	47	5.0	23	600	13	12.5
6	143	20	41.7	24	613	33	5.0
7	163	25	29.2	25	646	35	26.7
8	188	22	5.0	26	681	47	5.0
9	210	13	12.5	27	728	20	41.7
10	223	33	5.0	28	748	25	29.2
11	256	35	26.7	29	773	68	5.0
12	291	47	5.0	30	841	58	58.3
13	338	20	41.7	31	899	82	41.7
14	358	25	29.2	32	981	85	58.3
15	383	22	5.0	33	1066	50	83.3
16	405	13	12.5	34	1116	44	100.0
17	418	33	5.0	35	1160	21	0.0
18	451	35	26.7				

The voltage of the cell during the FC-DLC testing was recorded to monitor the health condition of the cell. During the whole endurance testing, these two cells didn't suffer failure such as leakage. **Figure 4-20** shows the typical profile of the cell voltage vs. time in one fuel cell dynamic load cycle. In conformity to the results in section 4.5, the voltage undershoot can be observed in the control cell when the output load suddenly increases. In comparison, the voltage response of the hybrid cell to the transient load is quicker and smoother.

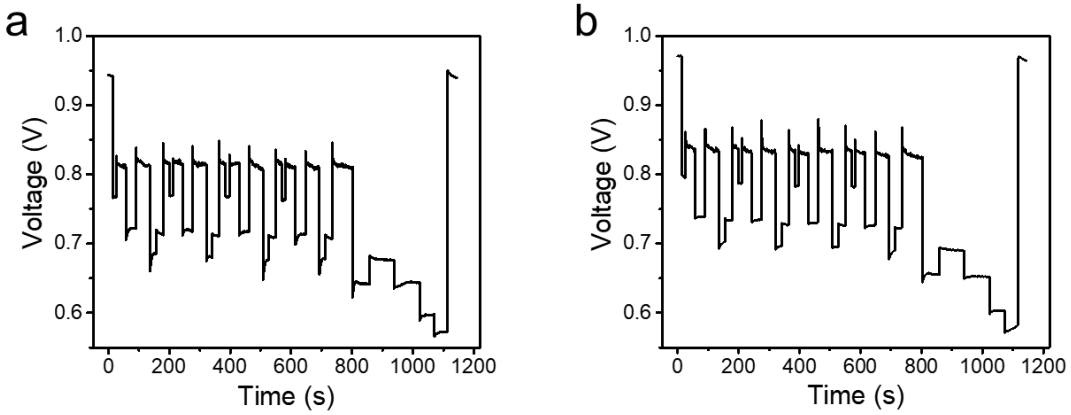

Figure 4-20. Typical profile of the cell voltage vs. time for a fuel cell dynamic load cycle of the control cell (a) and the hybrid cell (b).

The voltage profiles of TB1, 10, 20, and 28 for the control cell and the hybrid cell are shown in **Figure 4-21** and **4-22** respectively. In the first test block, both cells are shown noticeable voltage decline with cycling especially at high load output (**Figure 4-21**(a), **4-22**(a)). It's caused by the water accumulation in the fuel cell channel and gas diffusion layer. The condensed water produced during the cycling operation cannot be moved out from the cell entirely and therefore makes the resistance of the gas diffusion increase. The polarization curves measured before and after the first test block (**Figure 4-23**(a), **4-24**(a)),

as well as the constant current tests at different current densities (**Figure 4-25**(a), **4-26**(a)), reveal the degradation of the cell performance intuitively. For the control cell, the current density at 0.4 V dropped from 3.6 A/cm^2 to 2.5 A/cm^2. At a current density of 0.8 A/cm^2 and 1.8 A/cm^2, the reduction of the output voltage is about 70 mV and 100 mV respectively. These results indicate the ohmic resistance and the mass transport resistance increase after the dynamic load cycling.

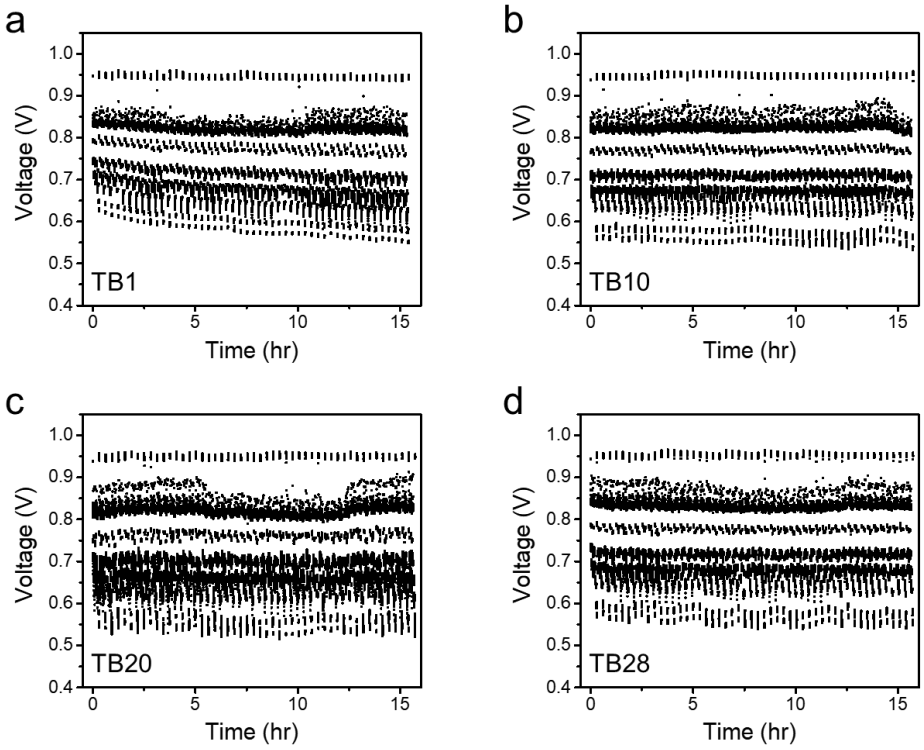

Figure 4-21. Voltage records of the fuel cell dynamic load cycle testing for the control cell of TB1, 10, 20, and 28.

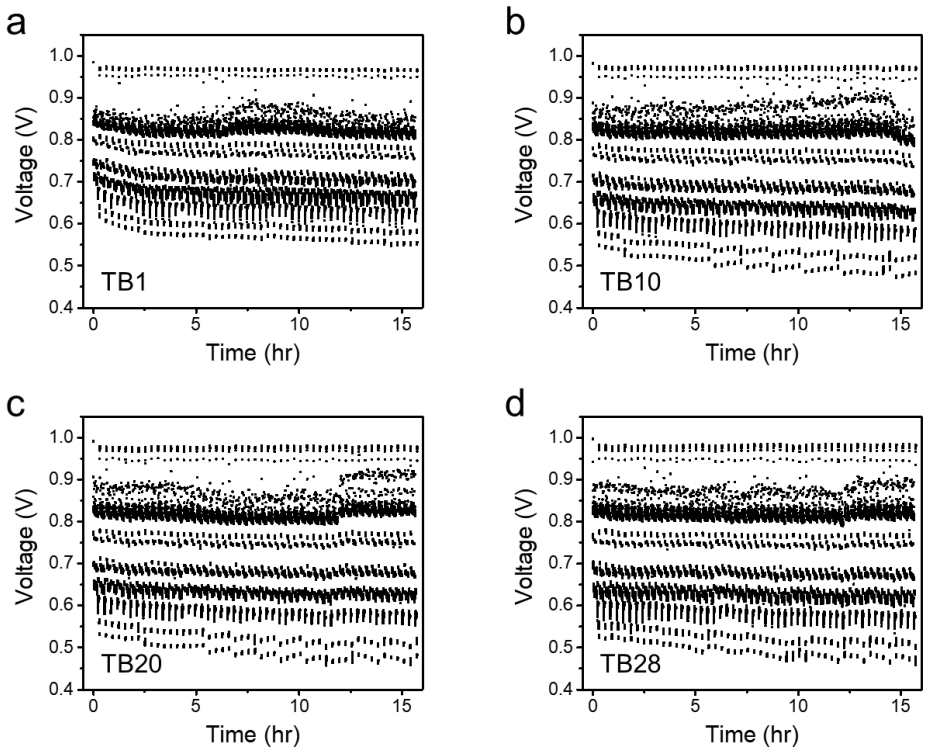

Figure 4-22. Voltage records of the fuel cell dynamic load cycle testing for the hybrid cell of TB1, 10, 20, and 28.

The hybrid cell shows the similar extent of degradation after the first test block. The output current at the cell voltage of 0.4 V decays to 2.4 A/cm^2. Not only at medium and high load range, but the cell voltage at 0.1 A/cm^2 reduced about 20 mV after the cycling. It indicates the degradation of the catalyst performance.

Not all of the degradation after the cycling is irreversible. Part of the degradation caused by cell drying out, flooding, or blocked gas channel can be recovered upon cell shutdown and consecutive restart.

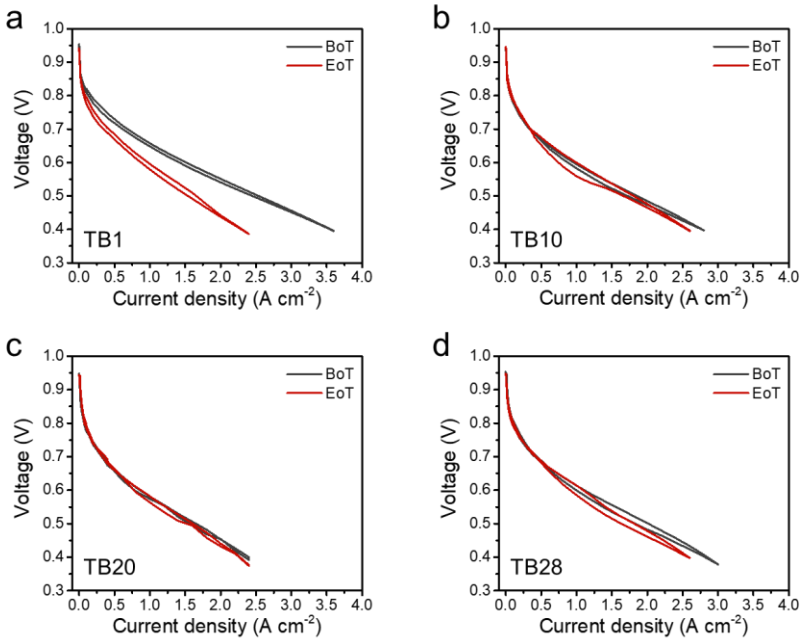

Figure 4-23. Polarization curves of the control cell tested at BoT and EoT of test block (TB) 1, 10, 20, and 28.

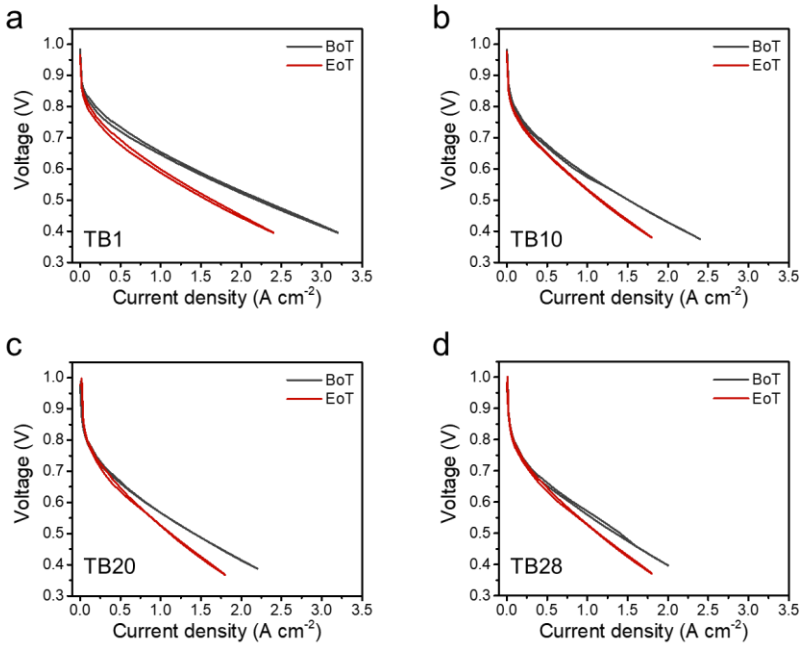

Figure 4-24. Polarization curves of the hybrid cell tested at BoT and EoT of test block (TB) 1, 10, 20, and 28.

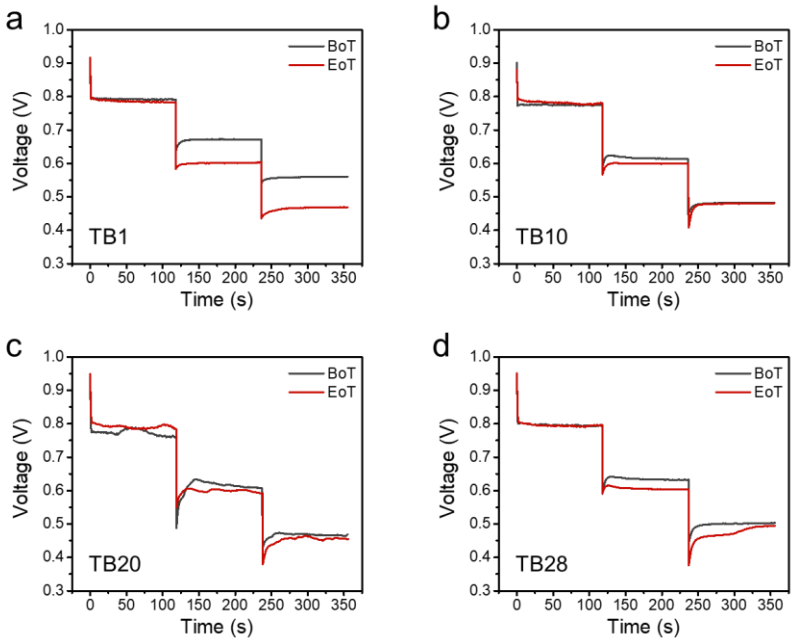

Figure 4-25. Cell voltage of the control cell at current density of 0.1, 0.8, and 1.8 A/cm^2 measured at BoT and EoT of TB1, 10, 20, and 28.

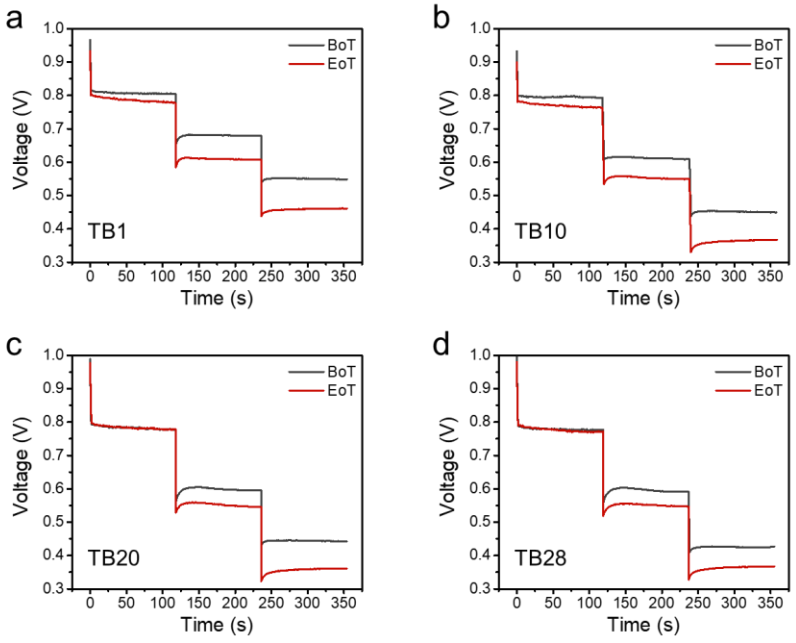

Figure 4-26. Cell voltage of the hybrid cell at current density of 0.1, 0.8, and 1.8 A/cm^2 measured at BoT and EoT of TB1, 10, 20, and 28.

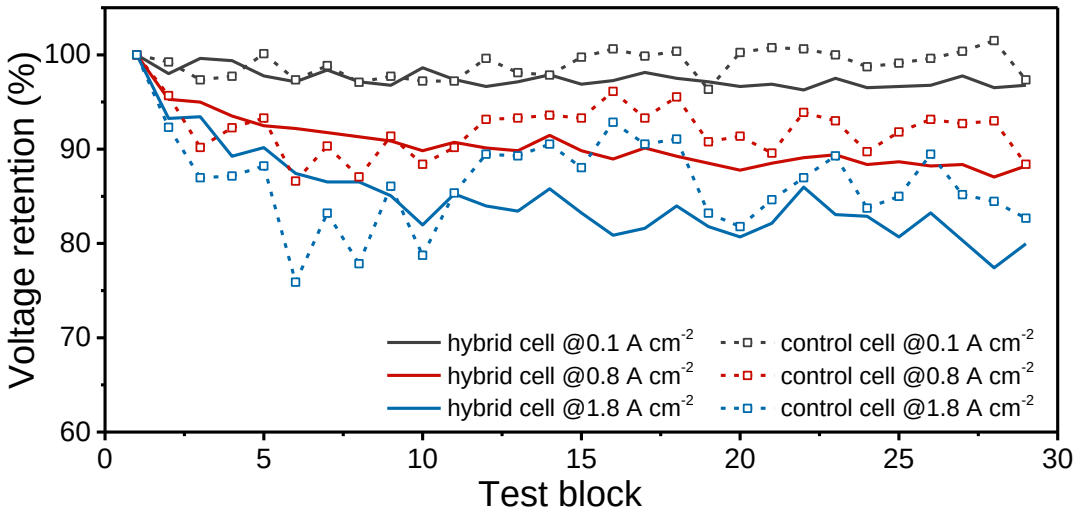

Figure 4-27. Voltage degradation over the entire fuel cell dynamic load cycling measurement of the control cell and the hybrid cell.

The degradation of the control cell and the hybrid cell over the entire endurance testing is shown in **Figure 4-27**. The retention ratios of the cell voltage after each test block to the initial voltage at different current densities are plotted versus the number of test block. In the early several test blocks, the voltage of the cells decreases significantly, especially at the medium and high output range. After that, the cell voltage descends gradually at a slower rate. Between test block 5 to test block 10, the control cell appears remarkable performance reduction and fluctuation. Thereafter, part of the voltage loss recovered in the next several test blocks. Overall, the performance of the control cell fluctuates severely and is easily affected by the operating conditions. On the contrary, the performance of the hybrid cell declines in a more stable and predictable fashion.

4.7 Conclusions

Novel PEMFCs through integrating anodes with a layer of WO_3/CNTs composite, which serves as a rapid-response hydrogen reservoir, scavenger for oxygen, sensor for power demand, and regulator for hydrogen-disassociation reaction. Such multifunctional anodes afford PEMFCs with significantly improved transient power and durability against fuel starvation and transient operation. Such PEMFCs can be fabricated at a similar cost to that of traditional PEMFCs yet provide a significant cost reduction at the system level. Scale production of the PEMFCs can be readily achieved by using existing PEMFC-manufacture infrastructure and technologies. This work enables the production of PEMFCs with improved power performance, durability, lifetime, and cost for automotive and other applications.

4.8 Experimental methods

H_2 pump cell test: To avoid the influence of cathodes during transient operation, symmetric cells were used for testing. The MEAs were prepared according to the same method as other cells. The Pt loadings on the anode and cathode were both 0.4 mg cm^{-2}. The hybrid cell was fabricated with a WO_3 composite electrode (WO_3 loading of ~4.9 mg cm^{-2}) as the anode, while the control cell was fabricated with a prefabricated GDL. During the scan current tests, 10 mL min^{-1} H_2 (100% humidified) was fed into the anodes and cathodes. The voltage of the cells was recorded by a Solartron 1860/1287 Electrochemical Interface (Solartron Analytical) under scan rates of 1 mA s^{-1}, 2.5 mA s^{-1} and 5 mA s^{-1}, respectively. The cut-off voltage of the test was set to 0.3 V to avoid oxidation of the anodes. For the transient-current tests, the cell voltage was monitored by a Solartron 1860 electrochemical interface, when the output current was switched from 0.2 A cm^{-2} to 2 A

cm^{-2}, while 50 mL min^{-1} of H_2 (100% humidified) was fed into both the anodes and cathodes. The cell resistance was measured by impedance spectroscopy (Solartron 1860/1287 Electrochemical Interface, Solartron Analytical) at open circuit; an AC signal of 10 mA was applied to the cell, and the frequency range of the impedance tests was limited from 10^5 Hz down to 1 Hz.

Fabrication of MEAs: The MEAs were made using the procedure as the follows. Briefly, catalyst ink was prepared by ultrasonically blending a commercial 40% Pt/C catalyst with a Nafion solution (5 wt%, Alfa Aesar) and ethanol for 2 h. The catalyst ink was sprayed onto both sides of the membrane with Pt loadings of 0.05 mg cm^{-2} and 0.4 mg cm^{-2} in the anode and cathode, respectively. MEAs were fabricated by sandwiching the catalyst-coated membranes between a WO_3 electrode and a pre-fabricated gas diffusion layer (GDL) (Toray TGH-060 carbon paper, 10 wt% poly-tetrafluoroethylene), and then hot pressed together at 130 °C under 200 kg cm^{-2} for 1 min. Control MEAs were fabricated using a pre-fabricated gas diffusion layer (GDL) instead of the WO_3 electrode as anodes. Single-cell tests were conducted in a 5 cm^2 PEMFC, the fuel (hydrogen) and the oxidant (oxygen) were humidified by bubbling through distilled water at dew point to achieve 100% humidity.

Dynamic response tests: while the cells were running under a steady state, the current outputs of the cells were abruptly increased from 0.05 A cm^{-2} to 2 A cm^{-2}, 3 A cm^{-2}, and 4 A cm^{-2}. The test was conducted by holding under each of the target current densities for 60 s. The anodes were fed with H_2 at a stoichiometry of 1.5. The cathode was supplied with O_2 at a stoichiometry of 4. The fuel (hydrogen) and the oxidant (oxygen) were humidified by bubbling through distilled water to achieve 100% humidity.

Simulated durability tests: three control cells were used (one for the starvation test, one for the acceleration/deceleration test, and one for the start-up test), while only one hybrid cell was used for the three tests. All tests were conducted at 50 ºC.

a. The simulated H_2 starvation tests were performed by switching the H_2 supply to N_2 flow (0.2 L min^{-1}) to a control cell and a hybrid cell while operated under a constant current density of 0.2 A cm^{-2} using the external direct-current power source (1287A Potentiostat Galvanostat). The cell voltage was recorded during the measurement, and each cycle lasted for 10 s after switching to N_2 flow. I-V curves were measured after each cycle, and the peak-power density was recorded.

b. The simulated acceleration and deceleration tests were conducted by oscillating the current output of a control cell and the hybrid cell between 50 mA cm^{-2} and 1000 mA cm^{-2} with a holding time of 120 s and 30 s, respectively. I-V curves were measured after certain cycles, and the peak power density was recorded.

c. For start-up tests, a control cell and the hybrid cell were kept at open circuit while fed with H_2 and O_2. The gas for the anodes was switched from H_2 to N_2 (30 mL min^{-1}) for 10 s to purge the anode compartment. Then, 1 mL of air was injected into the anodes, and the equilibrium OCV of the cells was recorded by the Solartron 1287 electrochemical interface. The cells were then maintained at a constant voltage of 0.8 V for a period of 20 s, and their current profiles were recorded. The simulated start-up process was conducted by maintaining a control cell and the hybrid cell at a constant voltage of 0.8 V. H_2 supply was then switched to an air flow of 20 mL min^{-1}. I-V curves after each two cycles were measured, and the peak power density was recorded.

Chapter 5. Exploration of WO_3-based material in fuel cell application

5.1 Introduction

In the previous chapters, the design of incorporating WO_3 as the energy-storage material into PEM fuel cells has been fully validated. It is worth noting that the extra power provided by the hybrid cell during transient conditions are much more than the capacitive energy can be delivered by WO_3 by itself, which inspires us that there may have synergetic effect between WO_3 and the Pt catalyst. WO_3 materials have also been considered as catalyst support or co-catalyst materials by many researchers. In this case, the electrocatalysis of WO_3 with Pt will be studied using rotating disk technology to explore the synergetic effect of WO_3, and also provide some guidance for design WO_3-based electrocatalyst.

In addition, we would like to expend the application of WO_3 into wider range of fuel cell technology, not only be restricted to the PEM fuel cell. PEM fuel cells are generally considered to be the most viable approach for mobile applications. However, these membranes require humid operating conditions, which limit the temperature of operation to less than 100 °C; they are also permeable to methanol and hydrogen, which lowers fuel efficiency. Solid, inorganic, acid compounds (or simply, solid acids) such as $CsHSO_4$ and $Rb_3H(SeO_4)_2$ have been widely studied because of their high proton conductivities and phase-transition behavior. For fuel-cell applications they offer the advantages of anhydrous proton transport and high-temperature stability (up to 250 °C). Some preliminary tests will be done to study the feasibility of WO_3 in high-temperature fuel cells.

5.2 Electrocatalysis of WO_3 with Pt

Platinum is up to now the most active electrocatalysts for both hydrogen oxidation reaction (HOR) and oxygen reduction reaction (ORR) in proton exchange membrane fuel cells (PEMFCs). However, the high price and rare resources of platinum make it impossible to use in large amount. To reduce the utilization of platinum, WO_3 is proposed as both the support and co-catalyst for PEMFCs.

To reveal the synergistic effect between WO_3 and Pt in the energy-storage electrode, catalyst-deficient thin film method using rotation disk electrode (RDE) was employed to determine the hydrogen oxidation reaction (HOR) kinetics on WO_3/Pt composite electrode. **Figure 5-1**(a) shows the HOR polarization curves of Pt black with a loading of 31.9 μg cm^{-2} at various rotating rates. The limiting current hardly changes with increasing rotating rates up to 3600 rpm. This suggests that the observed limiting currents are no longer diffusion-limiting current at low catalyst loadings. Instead, the observed limiting current is controlled by both HOR kinetics and hydrogen diffusion. Such catalyst-deficient electrode mimics the anode of fuel cell in the transient period under high current output, where low utilization of Pt might take place locally. To investigate the synergic effect between h-WO_3 and Pt, mixture of WO_3 and Pt is casted into the catalyst thin film with 31.9 μg cm^{-2} of Pt and 63.8 μg cm^{-2} of WO_3. HOR polarization curves of WO_3/Pt electrode shown in **Figure 5-1**(b) exhibit significantly enhanced catalytic activity. A well-defined current plateau forms at potentials over 30 mV (vs. RHE). The magnitude of the current plateau smoothly increases with the rotating rates, indicating the much faster HOR kinetics boosted by h-WO_3.

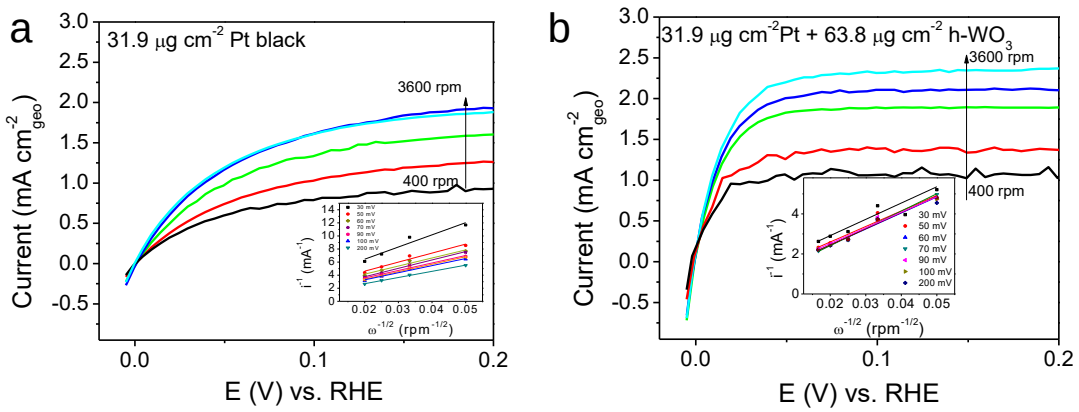

Figure 5-1. H_2 oxidation on Pt black (A) and the *h*-WO_3/ Pt black (B) in 0.5 M H_2SO_4 saturated with H_2 at various rotation rates. The inset shows Koutecky-Levich plots at different overpotentials.

To quantify the enhancement, we further calculate and compare the exchange current (*i*) of Pt electrode and WO_3/Pt electrode, which indicates the inherent HOR activity of the catalyst. To obtain the value of *i*, HOR kinetic currents (i_k) at various overpotential are firstly deduced from the intercept of the linear Koutecky-Levich plots (insets of **Figure 5-1**). **Figure 5-1** plots the i_k against the overpotential for both electrodes, where extrapolating the plots to x-axis gives the exchange current. The exchange current of HOR on WO_3/Pt is 0.54 mA, which is 2.57 times of that on Pt black. It is well-known that WO_3 alone does not exhibit HOR activity. Therefore, the enhanced kinetics could be explained by the rapid transport of dissociated protons-electrons and/or hydrogen atoms to h-WO_3, also known as hydrogen "spill-over" effect, that promotes desorption of product from the surface of Pt catalyst.

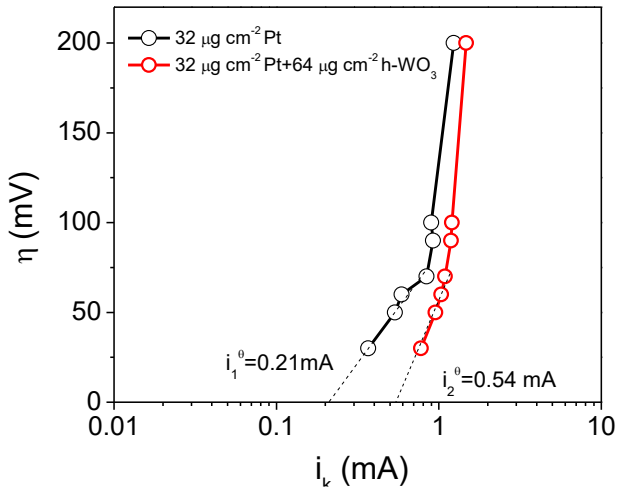

Figure 5-2. Tafel plots for HOR on Pt black and the mixture of Pt black and *h*-WO_3.

Above studies suggest that noble metal may exhibit synergic catalytic effect with WO_3, which make it possible to reduce the amount of Pt used.

5.3 Compatibility of WO_3 with various electrolyte materials of fuel cell

CsH_2PO_4, as a solid acid proton conductor based on tetrahedral oxyanion groups, has received attention widely because of its superior proton conductivity at elevated temperature. The crystalline structure of the powder was confirmed by X-ray diffraction. **Figure 5-3** shows the XRD pattern of CsH_2PO_4 powder measured at room temperature. All the diffraction peaks can be identified as the monoclinic phase of CsH_2PO_4. No impurity was found according to XRD result.

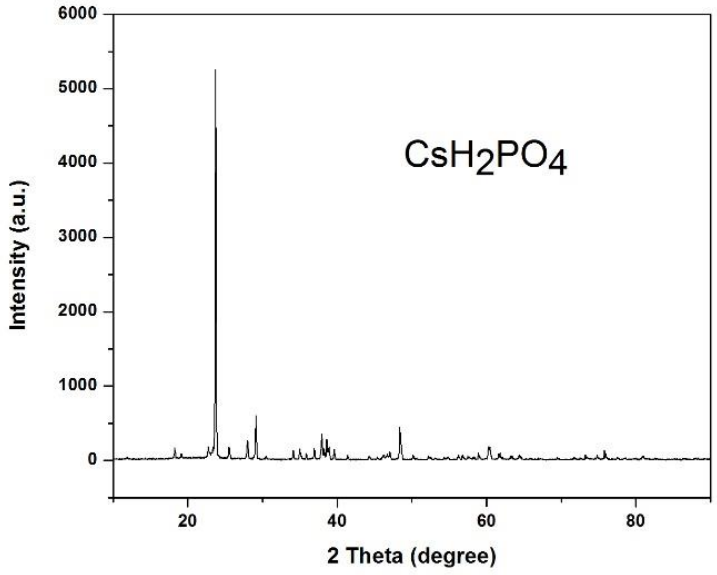

Figure 5-3. XRD pattern of CsH_2PO_4 powder.

Figure 5-4(a) shows the typical impedance spectra of CsH_2PO_4. Below 230 °C, the spectra exhibit a single arc that almost extends to the origin; the low frequency intercept of this arc with the real axis corresponds to the dc conductivity of the electrolyte. Above 230 °C, the behavior of the electrolyte can no longer be directly accessed. In this case, the extrapolated high frequency intercept with the real axis corresponds to the dc conductivity of the electrolyte. The conductivity of CsH_2PO_4 is quantitatively presented in **Figure 5-4**(b) in the Arrhenius form.

It is noteworthy that the superprotonic transition occurs at 230 °C under both test conditions. The conductivity increases 4 orders of magnitude from 220 °C to 230 °C. A moderate increase in conductivity under humid condition also observed. Contrary to the results in the literature, the conductivity decreases with the temperature below 230 °C. The reason may be due to the escape of adsorbed surface water. The powder samples were not

remove adsorbed surface water totally before conductivity measurement. Above 230 °C, the conductivity declined slightly, and the conductivity does not recover when the temperature is cooling down to 230 °C. The decrease can be assigned to dehydration of CsH_2PO_4. Even though we humidified the inlet gas, the dehydration of CsH_2PO_4 still did not be effectively inhibited.

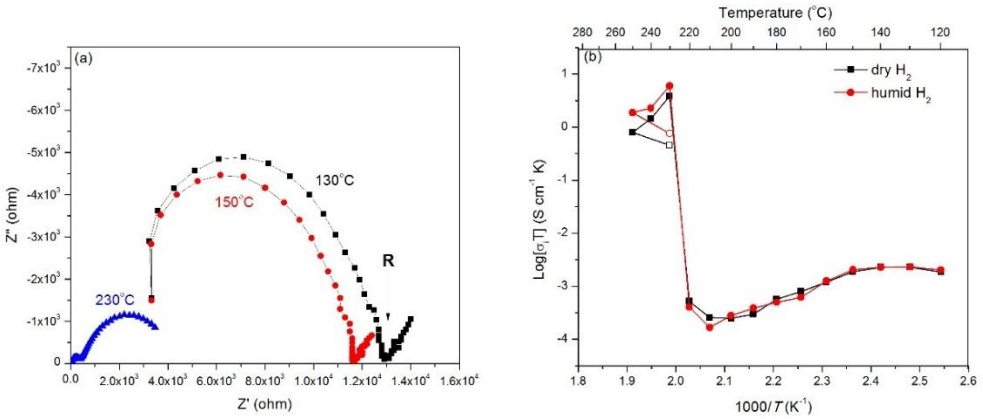

Figure 5-4. (a) Typical impedance spectra of CsH_2PO_4 measured in humid H_2; (b) Conductivity of CsH_2PO_4 under dry or humid H_2.

In order to use CsH_2PO_4 as the electrolytes for intermediate temperature fuel cells with energy-storage function, the stability of CsH_2PO_4 in the presence of WO_3 at high temperature must be considered. For this purposed, weight ratio 1:1 of CsH_2PO_4 with WO_3 powder were mixed and grounded with a mortar and pestle. Then the mixture powders were placed in ceramic crucibles and calcined in a box furnace at 250 °C in air for different times. The crystalline structure of after-calcined samples was then measured by XRD.

As shown in **Figure 5-5**, after calcination, the diffraction peaks of CsH_2PO_4 disappeared. The reason might be the decomposition of CsH_2PO_4 because the humidity did not carefully control during the calcination. Without humidification, dehydration of

CsH_2PO_4 will occur when the temperature is higher than 200 °C. For WO_3, although the peaks of WO_3 are weakened after calcination, the main characteristic peaks of WO_3 still remain. Further study will be conducted under more controlled environment. Nevertheless, considering that only a small quantity of WO_3 and CsH_2PO_4 will contact each other in the interface, we believe that CsH_2PO_4 could be used as electrolyte in the fuel cell cooperating with WO_3.

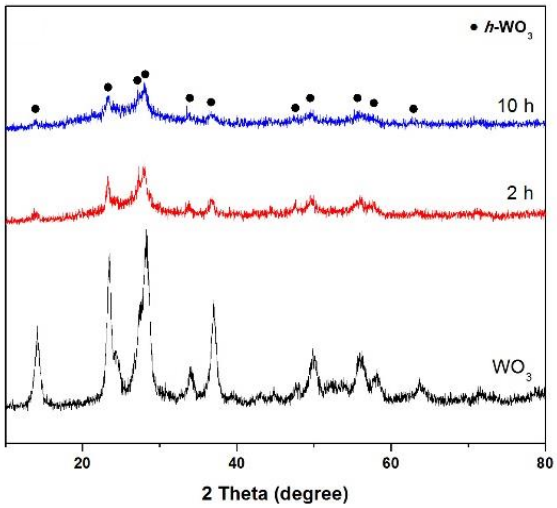

Figure 5-5. XRD patterns of the mixture powder of WO_3 with CsH_2PO_4 after calcination at 250 °C for 2 h and 10 h.

5.4 Conclusions

The electrocatalysis test of HOR indicates the synergetic effect between WO_3 and Pt catalyst. The WO_3 can enhance the HOR performance of the Pt by the spill-over effect which the dissociated H+ on the Pt active sites can move to WO_3 site rapidly and make the Pt surface available again for subsequent hydrogen dissociation reaction.

As-synthesized CsH_2PO_4 shows high proton conductivity at 230 °C, however, for applying CsH_2PO_4 as the electrolyte in a fuel cell, the humidity and temperature have to be

controlled cautiously to inhibit and avoid the dissolution and decomposition of CsH_2PO_4. WO_3 shows chemical stability with CsH_2PO_4 in short-term, which indicating WO_3 has potential to utilize in the fuel cell using CsH_2PO_4 as electrolyte.

5.5 Experimental methods

CsH_2PO_4: was prepared from an aqueous solution of Cs_2CO_3 and H_3PO_4 combined in a molar ratio of 1:2. Then methanol was added to induce its precipitation. The powder was then dried at 200 ^oC for several hours to remove the surface adsorbed water.

Conductivity test: The powders were pressed into pellets under a pressure of 6×10^3 kg cm^{-2}. Silver wires were applied on both sides of the obtained pellets using silver paste. The pellet samples were set in a quartz tube, and then dry or humidified hydrogen were supplied through the quartz tube at atmospheric pressure. The desired humidification levels were obtained by passing the inlet gas through a water bath maintained at 80 °C. Conductivity measurements were performed by means of ac impedance spectroscopy using a Solartion 1287 impedance analyzer in the frequency range from 10MHz to 1Hz with an applied voltage of 10 mV. The conductivity as a function of temperature was measured by stepwise increase the temperature from 120 °C to 250 °C. After having maintained the samples at 250 °C, the temperature was decreased to 230 °C and measured the conductivity at this point again. The ohmic resistance was carried out with a direct current (DC) polarization technique. The DC voltage was 0.2V.

Chapter 6. Conclusions

Proton exchange membrane fuel cells (PEMFCs) have been regarded as the most promising candidate for fuel cell vehicles and tools. Their broader adaption, however, has been impeded by cost and lifetime, as well as the inability to respond to fluctuations associated with operation conditions, fuel supply, and transient load. In this dissertation, a novel strategy to improve the performance and durability of PEMFCs for automotive application is purposed. Unlike the conventional hybrid strategies, which batteries or capacitors are always integrated with the fuel cell to achieve high fuel efficiency and high-power output, the novel fuel cell is integrated with energy-storage materials to form a hybrid device.

Tungsten oxide is proved to be a promising energy-storage material using in the PEMFC application, which has high chemical stability and excellent electrochemical performance in the fuel cell configuration. WO_3 with hexagonal crystal structure shows outstanding capacity in the PEM fuel cell environment and the rate performance is further improved by introducing carbon nanotube into the composite. By integrating a thin layer of tungsten oxide (WO_3) within the anodes, novel PEMFCs shows significantly enhanced power performance for transient operation, as well as improved durability against adverse operating conditions. Meanwhile, the enhanced power performance minimizes the use of auxiliary energy-storage systems and reduces costs.

In addition, the mechanisms of degradation of PEMFCs, as well as the working principles of WO_3 in the hybrid cell are studied. The WO_3 layer in the hybrid cell is serves as a rapid-response hydrogen reservoir, oxygen scavenger, sensor for power demand, and

regulator for hydrogen-disassociation reaction, effectively stabilize the anode potential and inhibits rising of the anode potential during the transient conditions.

References

1. https://yearbook.enerdata.net/total-energy/world-consumption-statistics.html. https://yearbook.enerdata.net/total-energy/world-consumption-statistics.html (accessed May 10).

2. Aricò, A. S.; Bruce, P.; Scrosati, B.; Tarascon, J.-M.; Van Schalkwijk, W., Nanostructured materials for advanced energy conversion and storage devices. *Nature materials* **2005,** *4* (5), 366-377.

3. Miller, J. R.; Burke, A. F., Electrochemical capacitors: challenges and opportunities for real-world applications. *The Electrochemical Society Interface* **2008,** *17* (1), 53.

4. Chen, Z.; Hassan, F. M.; Yu, A., Electrochemical Engineering Fundamentals. In *Electrochemical Technologies for Energy Storage and Conversion*, Wiley-VCH Verlag GmbH & Co. KGaA: 2011; pp 45-68.

5. Gao, H.; Liu, S.; Li, Y.; Conte, E.; Cao, Y., *A Critical Review of Spinel Structured Iron Cobalt Oxides Based Materials for Electrochemical Energy Storage and Conversion*. 2017; Vol. 10, p 1787.

6. Hoogers, G., *Fuel cell technology handbook*. CRC press: 2002.

7. Frano, B., PEM fuel cells: theory and practice. *Academic, Burlington Google Scholar* **2005**.

8. Crow, D. R., *Principles and applications of electrochemistry*. Routledge: 2017.

9. Fuel Cell Technologies Office Multi-Year Research, Development, and Demonstration Plan. Energy, D. o., Ed. 2017.

10. O'hayre, R.; Cha, S.-W.; Prinz, F. B.; Colella, W., *Fuel cell fundamentals*. John Wiley & Sons: 2016.

11. Wang, B., Recent development of non-platinum catalysts for oxygen reduction reaction. *J Power Sources* **2005,** *152*, 1-15.

12. Wagner, N.; Schnurnberger, W.; Müller, B.; Lang, M., Electrochemical impedance spectra of solid-oxide fuel cells and polymer membrane fuel cells. *Electrochim Acta* **1998,** *43* (24), 3785-3793.

13. Santiago, E. I.; Batista, M. S.; Assaf, E. M.; Ticianelli, E. A., Mechanism of CO tolerance on molybdenum-based electrocatalysts for PEMFC. *J Electrochem Soc* **2004,** *151* (7), A944-A949.

14. Park, S.; Lee, J.-W.; Popov, B. N., A review of gas diffusion layer in PEM fuel cells: Materials and designs. *International Journal of Hydrogen Energy* **2012,** *37* (7), 5850-5865.

15. Kleemann, J.; Finsterwalder, F.; Tillmetz, W., Characterisation of mechanical behaviour and coupled electrical properties of polymer electrolyte membrane fuel cell gas diffusion layers. *J Power Sources* **2009,** *190* (1), 92-102.

16. Singh, S., System reliability modeling and evaluation. *Journal of Mines, Metals & Fuels* **1989,** *37* (3), 117-122.

17. Albarbar, A.; Alrweq, M., Proton Exchange Membrane Fuel Cells: Review. In *Proton Exchange Membrane Fuel Cells: Design, Modelling and Performance Assessment Techniques*, Springer International Publishing: Cham, 2018; pp 9-29.

18. Zhou, Y.; Neyerlin, K.; Olson, T. S.; Pylypenko, S.; Bult, J.; Dinh, H. N.; Gennett, T.; Shao, Z.; O'Hayre, R., Enhancement of Pt and Pt-alloy fuel cell catalyst activity and durability via nitrogen-modified carbon supports. *Energy & Environmental Science* **2010,** *3* (10), 1437-1446.

19. Crabtree, R. H., *Energy production and storage: inorganic chemical strategies for a warming world*. John Wiley & Sons: 2010.

20. Scott, K.; Xu, C.; Wu, X., Intermediate temperature proton-conducting membrane electrolytes for fuel cells. *Wiley Interdisciplinary Reviews: Energy and Environment* **2014,** *3* (1), 24-41.

21. Staiti, P.; Arico, A.; Antonucci, V.; Hocevar, S., Morphological variation of platinum catalysts in phosphotungstic acid fuel cell. *J Power Sources* **1998,** *70* (1), 91-101.

22. Surowiec, J.; Bogoczek, R., Studies on the thermal stability of the perfluorinated cation-exchange membrane Nafion-417. *Journal of thermal analysis* **1988,** *33* (4), 1097-1102.

23. Wilkie, C. A.; Thomsen, J. R.; Mittleman, M. L., Interaction of poly (methyl methacrylate) and Nafions. *J Appl Polym Sci* **1991,** *42* (4), 901-909.

24. Samms, S.; Wasmus, S.; Savinell, R., Thermal stability of Nafion® in simulated fuel cell environments. *J Electrochem Soc* **1996,** *143* (5), 1498-1504.

25. Shin, S.-J.; Lee, J.-K.; Ha, H.-Y.; Hong, S.-A.; Chun, H.-S.; Oh, I.-H., Effect of the catalytic ink preparation method on the performance of polymer electrolyte membrane fuel cells. *J Power Sources* **2002,** *106* (1-2), 146-152.

26. Fowler, M.; Mann, R.; Amphlett, J.; Peppley, B.; Roberge, P., Reliability issues and voltage degradation. *Handbook of Fuel Cells* **2005**.

27. Yuan, X.-Z.; Li, H.; Zhang, S.; Martin, J.; Wang, H., A review of polymer electrolyte membrane fuel cell durability test protocols. *J Power Sources* **2011,** *196* (22), 9107-9116.

28. Pedersen, C. M.; Escudero-Escribano, M.; Velázquez-Palenzuela, A.; Christensen, L. H.; Chorkendorff, I.; Stephens, I. E., Benchmarking Pt-based electrocatalysts for low temperature fuel cell reactions with the rotating disk electrode: oxygen reduction and hydrogen oxidation in the presence of CO. *Electrochim Acta* **2015,** *179*, 647-657.

29. Ahn, S.-Y.; Shin, S.-J.; Ha, H.; Hong, S.-A.; Lee, Y.-C.; Lim, T.; Oh, I.-H., Performance and lifetime analysis of the kW-class PEMFC stack. *J Power Sources* **2002,** *106* (1-2), 295-303.

30. Meier, J. C.; Galeano, C.; Katsounaros, I.; Topalov, A. A.; Kostka, A.; Schüth, F.; Mayrhofer, K. J., Degradation mechanisms of Pt/C fuel cell catalysts under simulated start–stop conditions. *Acs Catalysis* **2012,** *2* (5), 832-843.

31. Wilkinson, D.; St-Pierre, J., Durability. *Handbook of fuel cells* **2003**.

32. Antunes, R. A.; Oliveira, M. C. L.; Ett, G.; Ett, V., Corrosion of metal bipolar plates for PEM fuel cells: a review. *International Journal of Hydrogen Energy* **2010,** *35* (8), 3632-3647.

33. Yang, L.; Larouche, N.; Chenitz, R.; Zhang, G.; Lefèvre, M.; Dodelet, J.-P., Activity, performance, and durability for the reduction of oxygen in PEM fuel cells, of Fe/N/C electrocatalysts obtained from the pyrolysis of metal-organic-framework and iron porphyrin precursors. *Electrochim Acta* **2015,** *159*, 184-197.

34. Gabreab, E. M.; Hinds, G.; Fearn, S.; Hodgson, D.; Millichamp, J.; Shearing, P. R.; Brett, D. J., An electrochemical treatment to improve corrosion and contact resistance of stainless steel bipolar plates used in polymer electrolyte fuel cells. *J Power Sources* **2014,** *245*, 1014-1026.

35. Brady, M. P.; Elhamid, M. A.; Dadheech, G.; Bradley, J.; Toops, T. J.; Meyer III, H. M.; Tortorelli, P. F., Manufacturing and performance assessment of stamped, laser welded, and nitrided FeCrV stainless steel bipolar plates for proton exchange membrane fuel cells. *International Journal of Hydrogen Energy* **2013,** *38* (11), 4734-4739.

36. Tan, J.; Chao, Y.; Yang, M.; Williams, C.; Van Zee, J., Degradation characteristics of elastomeric gasket materials in a simulated PEM fuel cell environment. *Journal of materials engineering and performance* **2008,** *17* (6), 785-792.

37. Ciureanu, M.; Wang, H., Electrochemical Impedance Study of Electrode-Membrane Assemblies in PEM Fuel Cells: I. Electro-oxidation of H 2 and H 2/CO Mixtures on Pt-Based Gas-Diffusion Electrodes. *J Electrochem Soc* **1999,** *146* (11), 4031-4040.

38. García, G.; Silva-Chong, J.; Guillén-Villafuerte, O.; Rodríguez, J.; González, E.; Pastor, E., CO tolerant catalysts for PEM fuel cells: Spectroelectrochemical studies. *Catalysis Today* **2006,** *116* (3), 415-421.

39. Uribe, F.; Valerio, J.; Rockward, T.; Stenersen, E. In *205th Meeting of The Electrochemistry Society, San Antonio, TX, May 2004*, Abstract.

40. Mikkola, M. S.; Rockward, T.; Uribe, F. A.; Pivovar, B., The effect of NaCl in the cathode air stream on PEMFC performance. *Fuel cells* **2007,** *7* (2), 153-158.

41. Mohtadi, R.; Lee, W.-K.; Cowan, S.; Van Zee, J.; Murthy, M., Effects of hydrogen sulfide on the performance of a PEMFC. *Electrochemical and solid-state letters* **2003,** *6* (12), A272-A274.

42. Mohtadi, R.; Lee, W.-K.; Van Zee, J., Assessing durability of cathodes exposed to common air impurities. *J Power Sources* **2004,** *138* (1-2), 216-225.

43. Mukerjee, S.; Urian, R. C., Bifunctionality in Pt alloy nanocluster electrocatalysts for enhanced methanol oxidation and CO tolerance in PEM fuel cells: electrochemical and in situ synchrotron spectroscopy. *Electrochim Acta* **2002,** *47* (19), 3219-3231.

44. Moore, J. M.; Adcock, P. L.; Lakeman, J. B.; Mepsted, G. O., The effects of battlefield contaminants on PEMFC performance. *J Power Sources* **2000,** *85* (2), 254-260.

45. Urdampilleta, I.; Uribe, F.; Rockward, T.; Brosha, E. L.; Pivovar, B.; Garzon, F. H., PEMFC poisoning with H2S: dependence on operating conditions. *ECS Transactions* **2007,** *11* (1), 831-842.

46. Rocheleau, R. E. *Final Technical Report: Hawaii Hydrogen Center for Development and Deployment of Distributed Energy Systems*; University of Hawaii: 2008.

47. Uribe, F.; Zawodzinski Jr, T. In *200th Meeting of The Electrochemistry Society, San Francisco, CA, September 2001*, Abstract.

48. Uribe, F.; Brosha, E.; Garzon, F.; Mikkola, M.; Pivovar, B.; Rockward, T.; Valerio, J.; Wilson, M., VII. I. 4 Effect of fuel and air impurities on PEM fuel cell performance. *DOE Hydrogen Program* **2005**, 1046-1051.

49. Garzon, F.; Uribe, F. A.; Rockward, T.; Urdampilleta, I. G.; Brosha, E. L., The impact of hydrogen fuel contaminates on long-term PMFC performance. *ECS Transactions* **2006,** *3* (1), 695-703.

50. Uribe, F. A.; Gottesfeld, S.; Zawodzinski, T. A., Effect of ammonia as potential fuel impurity on proton exchange membrane fuel cell performance. *J Electrochem Soc* **2002,** *149* (3), A293-A296.

51. Garzon, F.; Uribe, F., Effects of contaminants on catalyst activity. *Handbook of Fuel Cells* **2009**.

52. Zhang, J.; Thampan, T.; Datta, R., Influence of anode flow rate and cathode oxygen pressure on CO poisoning of proton exchange membrane fuel cells. *J Electrochem Soc* **2002,** *149* (6), A765-A772.

53. Si, Y.; Jiang, R.; Lin, J.-C.; Kunz, H. R.; Fenton, J. M., CO tolerance of carbon-supported platinum-ruthenium catalyst at elevated temperature and atmospheric pressure in a PEM fuel cell. *J Electrochem Soc* **2004,** *151* (11), A1820-A1824.

54. Qi, Z.; Kaufman, A., CO-tolerance of low-loaded Pt/Ru anodes for PEM fuel cells. *J Power Sources* **2003,** *113* (1), 115-123.

55. Qi, Z.; He, C.; Kaufman, A., Effect of CO in the anode fuel on the performance of PEM fuel cell cathode. *J Power Sources* **2002,** *111* (2), 239-247.

56. Lee, W.-K.; Van Zee, J.; Murthy, M., A Method for Characterizing CO Transients in a PEMFC. *Fuel Cells* **2003,** *3* (1-2), 52-58.

57. Krishnan, P.; Park, J.-S.; Kim, C.-S., Performance of a poly (2, 5-benzimidazole) membrane based high temperature PEM fuel cell in the presence of carbon monoxide. *J Power Sources* **2006,** *159* (2), 817-823.

58. Roth, C.; Benker, N.; Buhrmester, T.; Mazurek, M.; Loster, M.; Fuess, H.; Koningsberger, D. C.; Ramaker, D. E., Determination of O[H] and CO Coverage and Adsorption Sites on PtRu Electrodes in an Operating PEM Fuel Cell. *Journal of the American Chemical Society* **2005,** *127* (42), 14607-14615.

59. Ciureanu, M.; Wang, H., Electrochemical impedance study of anode CO-poisoning in PEM fuel cells. *Journal of New Materials for Electrochemical Systems* **2000,** *3* (2), 107-120.

60. Krumpelt, M.; Krause, T.; Carter, J.; Kopasz, J.; Ahmed, S., Fuel processing for fuel cell systems in transportation and portable power applications. *Catalysis today* **2002,** *77* (1-2), 3-16.

61. Knights, S. D.; Colbow, K. M.; St-Pierre, J.; Wilkinson, D. P., Aging mechanisms and lifetime of PEFC and DMFC. *J Power Sources* **2004,** *127* (1-2), 127-134.

62. Taniguchi, A.; Akita, T.; Yasuda, K.; Miyazaki, Y., Analysis of electrocatalyst degradation in PEMFC caused by cell reversal during fuel starvation. *J Power Sources* **2004,** *130* (1-2), 42-49.

63. Ralph, T. R.; Hudson, S.; Wilkinson, D. P., Electrocatalyst stability in PEMFCs and the role of fuel starvation and cell reversal tolerant anodes. *ECS Transactions* **2006,** *1* (8), 67-84.

64. Meyers, J. P.; Darling, R. M., Model of carbon corrosion in PEM fuel cells. *J Electrochem Soc* **2006,** *153* (8), A1432-A1442.

65. Paul, T. Y.; Gu, W.; Makharia, R.; Wagner, F. T.; Gasteiger, H. A., The impact of carbon stability on PEM fuel cell startup and shutdown voltage degradation. *Ecs Transactions* **2006,** *3* (1), 797-809.

66. Makharia, R.; Kocha, S.; Yu, P.; Sweikart, M. A.; Gu, W.; Wagner, F.; Gasteiger, H. A., Durable PEM fuel cell electrode materials: requirements and benchmarking methodologies. *Ecs Transactions* **2006,** *1* (8), 3-18.

67. Barton, R. H., Cell voltage monitor for a fuel cell stack. Google Patents: 2004.

68. Reiser, C. A.; Bregoli, L.; Patterson, T. W.; Jung, S. Y.; Yang, J. D.; Perry, M. L.; Jarvi, T. D., A reverse-current decay mechanism for fuel cells. *Electrochemical and Solid-State Letters* **2005,** *8* (6), A273-A276.

69. Patterson, T. W.; Darling, R. M., Damage to the cathode catalyst of a PEM fuel cell caused by localized fuel starvation. *Electrochemical and Solid-State Letters* **2006,** *9* (4), A183-A185.

70. Pekula, N.; Heller, K.; Chuang, P.; Turhan, A.; Mench, M.; Brenizer, J.; Ünlü, K., Study of water distribution and transport in a polymer electrolyte fuel cell using neutron imaging. *Nuclear Instruments and Methods in Physics Research Section A: Accelerators, Spectrometers, Detectors and Associated Equipment* **2005,** *542* (1-3), 134-141.

71. Fuller, T. F.; Newman, J., Water and thermal management in solid-polymer-electrolyte fuel cells. *J Electrochem Soc* **1993,** *140* (5), 1218-1225.

72. Darling, R. M.; Meyers, J. P., Kinetic model of platinum dissolution in PEMFCs. *J Electrochem Soc* **2003,** *150* (11), A1523-A1527.

73. Darling, R. M.; Meyers, J. P., Mathematical model of platinum movement in PEM fuel cells. *J Electrochem Soc* **2005,** *152* (1), A242-A247.

74. Komanicky, V.; Chang, K.; Menzel, A.; Markovic, N.; You, H.; Wang, X.; Myers, D., Stability and dissolution of platinum surfaces in perchloric acid. *J Electrochem Soc* **2006,** *153* (10), B446-B451.

75. Wang, X.; Kumar, R.; Myers, D. J., Effect of voltage on platinum dissolution relevance to polymer electrolyte fuel cells. *Electrochemical and Solid-State Letters* **2006,** *9* (5), A225-A227.

76. Perry, M. L.; Patterson, T.; Reiser, C., Systems strategies to mitigate carbon corrosion in fuel cells. *Ecs Transactions* **2006,** *3* (1), 783-795.

77. Zheng, H.; Ou, J. Z.; Strano, M. S.; Kaner, R. B.; Mitchell, A.; Kalantar-zadeh, K., Nanostructured Tungsten Oxide - Properties, Synthesis, and Applications. *Advanced Functional Materials* **2011,** *21* (12), 2175-2196.

78. Butler, M. A., Photoelectrolysis and physical properties of the semiconducting electrode WO<inf>2</inf> . *Journal of Applied Physics* **1977,** *48* (5), 1914-1920.

79. Benson, J. E.; Kohn, H. W.; Boudart, M., On the reduction of tungsten trioxide accelerated by platinum and water. *Journal of Catalysis* **1966,** *5* (2), 307-313.

80. Orsini, G.; Tricoli, V., Mesoporous, high-surface-area tungsten oxide monoliths with mixed electron/proton conductivity. *Journal of Materials Chemistry* **2010,** *20* (30), 6299-6308.

81. Orsini, G.; Tricoli, V., Facile nonhydrolytic sol-gel route to mesoporous mixed-conducting tungsten oxide. *Journal of Materials Chemistry* **2011,** *21* (38), 14530-14542.

82. Orsini, G.; Tricoli, V., Fractal mesoporosity and proton transport in WO3 xerogels. *Journal of Materials Chemistry* **2012,** *22* (45), 23861-23870.

83. Li, Y. M.; Hibino, M.; Miyayania, M.; Kudo, T., Proton conductivity of tungsten trioxide hydrates at intermediate temperature. *Solid State Ionics* **2000,** *134* (3–4), 271-279.

84. Antolini, E.; Gonzalez, E. R., Tungsten-based materials for fuel cell applications. *Applied Catalysis B: Environmental* **2010,** *96* (3–4), 245-266.

85. Jo, C.; Hwang, J.; Song, H.; Dao, A. H.; Kim, Y.-T.; Lee, S. H.; Hong, S. W.; Yoon, S.; Lee, J., Block-Copolymer-Assisted One-Pot Synthesis of Ordered Mesoporous WO3−x/Carbon Nanocomposites as High-Rate-Performance Electrodes for Pseudocapacitors. *Advanced Functional Materials* **2013,** *23* (30), 3747-3754.

86. Yoon, S.; Kang, E.; Kim, J. K.; Lee, C. W.; Lee, J., Development of high-performance supercapacitor electrodes using novel ordered mesoporous tungsten oxide materials with high electrical conductivity. *Chemical communications* **2011,** *47* (3), 1021-1023.

87. Wang, Y. H.; Wang, C. C.; Cheng, W. Y.; Lu, S. Y., Dispersing WO3 in carbon aerogel makes an outstanding supercapacitor electrode material. *Carbon* **2014,** *69* (0), 287-293.

88. Chang, K.-H.; Hu, C.-C.; Huang, C.-M.; Liu, Y.-L.; Chang, C.-I., Microwave-assisted hydrothermal synthesis of crystalline WO3–WO3·0.5H2O mixtures for pseudocapacitors of the asymmetric type. *Journal of Power Sources* **2011,** *196* (4), 2387-2392.

89. Cui, X.; Shi, J.; Chen, H.; Zhang, L.; Guo, L.; Gao, J.; Li, J., Platinum/Mesoporous WO3 as a Carbon-Free Electrocatalyst with Enhanced Electrochemical Activity for Methanol Oxidation. *The Journal of Physical Chemistry B* **2008,** *112* (38), 12024-12031.

90. Chen, L.; Lam, S.; Zeng, Q.; Amal, R.; Yu, A., Effect of Cation Intercalation on the Growth of Hexagonal WO3Nanorods. *The Journal of Physical Chemistry C* **2012,** *116* (21), 11722-11727.

91. Xia, Y.; Yang, P.; Sun, Y.; Wu, Y.; Mayers, B.; Gates, B.; Yin, Y.; Kim, F.; Yan, H., One-dimensional nanostructures: synthesis, characterization, and applications. *Advanced materials* **2003,** *15* (5), 353-389.

92. Gu, Z.; Zhai, T.; Gao, B.; Sheng, X.; Wang, Y.; Fu, H.; Ma, Y.; Yao, J., Controllable assembly of WO3 nanorods/nanowires into hierarchical nanostructures. *The Journal of Physical Chemistry B* **2006,** *110* (47), 23829-23836.

93. Huang, K.; Pan, Q.; Yang, F.; Ni, S.; Wei, X.; He, D., Controllable synthesis of hexagonal WO3nanostructures and their application in lithium batteries. *Journal of Physics D: Applied Physics* **2008,** *41* (15), 155417.

94. Wang, J.; Khoo, E.; Lee, P. S.; Ma, J., Controlled synthesis of WO3 nanorods and their electrochromic properties in H2SO4 electrolyte. *The Journal of Physical Chemistry C* **2009,** *113* (22), 9655-9658.

95. Zhu, J.; Wang, S.; Xie, S.; Li, H., Hexagonal single crystal growth of WO3 nanorods along a [110] axis with enhanced adsorption capacity. *Chemical communications* **2011,** *47* (15), 4403-5.

96. Wang, L.; Liu, H., Performance studies of PEM fuel cells with interdigitated flow fields. *J Power Sources* **2004,** *134* (2), 185-196.

97. Hwang, J. J.; Hwang, H. S., Parametric studies of a double-cell stack of PEMFC using Grafoil™ flow-field plates. *J Power Sources* **2002,** *104* (1), 24-32.

98. Williams, M. V.; Kunz, H. R.; Fenton, J. M., Operation of Nafion®-based PEM fuel cells with no external humidification: influence of operating conditions and gas diffusion layers. *J Power Sources* **2004,** *135* (1), 122-134.

99. Kim, J.; Lee, S. M.; Srinivasan, S.; Chamberlin, C. E., Modeling of Proton Exchange Membrane Fuel Cell Performance with an Empirical Equation. *J Electrochem Soc* **1995,** *142* (8), 2670-2674.

100. Wang, L.; Husar, A.; Zhou, T.; Liu, H., A parametric study of PEM fuel cell performances. *International Journal of Hydrogen Energy* **2003,** *28* (11), 1263-1272.

101. Amphlett, J. C.; Baumert, R. M.; Mann, R. F.; Peppley, B. A.; Roberge, P. R.; Harris, T. J., Performance Modeling of the Ballard Mark IV Solid Polymer Electrolyte Fuel Cell: I . Mechanistic Model Development. *J Electrochem Soc* **1995,** *142* (1), 1-8.

102. Springer, T. E.; Zawodzinski, T. A.; Gottesfeld, S., Polymer Electrolyte Fuel Cell Model. *J Electrochem Soc* **1991,** *138* (8), 2334-2342.

103. Berg, P.; Promislow, K.; St. Pierre, J.; Stumper, J.; Wetton, B., Water Management in PEM Fuel Cells. *J Electrochem Soc* **2004,** *151* (3), A341-A353.

104. Rajalakshmi, N.; Jayanth, T. T.; Thangamuthu, R.; Sasikumar, G.; Sridhar, P.; Dhathathreyan, K. S., Water transport characteristics of polymer electrolyte membrane fuel cell. *International Journal of Hydrogen Energy* **2004,** *29* (10), 1009-1014.

105. Hyun, D.; Kim, J., Study of external humidification method in proton exchange membrane fuel cell. *J Power Sources* **2004,** *126* (1), 98-103.

106. Zhang, J.; Tang, Y.; Song, C.; Zhang, J.; Wang, H., PEM fuel cell open circuit voltage (OCV) in the temperature range of 23 °C to 120 °C. *Journal of Power Sources* **2006,** *163* (1), 532-537.

107. Wang, Y.; Wang, C. Y., Transient analysis of polymer electrolyte fuel cells. *Electrochimica Acta* **2005,** *50* (6), 1307-1315.

108. Yan, Q. G.; Toghiani, H.; Causey, H., Steady state and dynamic performance of proton exchange membrane fuel cells (PEMFCs) under various operating conditions and load changes. *Journal of Power Sources* **2006,** *161* (1), 492-502.

109. Shen, Q.; Hou, M.; Yan, X. Q.; Liang, D.; Zang, Z. M.; Hao, L. X.; Shao, Z. G.; Hou, Z. J.; Ming, P. W.; Yi, B. L., The voltage characteristics of proton exchange membrane fuel cell (PEMFC) under steady and transient states. *Journal of Power Sources* **2008,** *179* (1), 292-296.

110. Liu, Z. X.; Yang, L. Z.; Mao, Z. Q.; Zhuge, W. L.; Zhang, Y. J.; Wang, L. S., Behavior of PEMFC in starvation. *Journal of Power Sources* **2006,** *157* (1), 166-176.

111. Ralph, T. R.; Hudson, S.; Wilkinson, D. P., Electrocatalyst stability in PEMFCs and the role of fuel starvation and cell reversal tolerant anodes. *ECS Transactions* **2006**.

112. Jia, F.; Guo, L.; Liu, H., Mitigation strategies for hydrogen starvation under dynamic loading in proton exchange membrane fuel cells. *Energy Conversion and Management* **2017,** *139*, 175-181.

113. Reiser, C. A.; Bregoli, L.; Patterson, T. W.; Yi, J. S.; Yang, J. D.; Perry, M. L.; Jarvi, T. D., A Reverse-Current Decay Mechanism for Fuel Cells. *Electrochemical and Solid-State Letters* **2005,** *8* (6), A273-A276.

114. Tang, H.; Qi, Z. G.; Ramani, M.; Elter, J. F., PEM fuel cell cathode carbon corrosion due to the formation of air/fuel boundary at the anode. *Journal of Power Sources* **2006,** *158* (2), 1306-1312.

115. Yu, J. L.; Jiang, Z. W.; Hou, M.; Liang, D.; Xiao, Y.; Dou, M. L.; Shao, Z. G.; Yi, B. L., Analysis of the behavior and degradation in proton exchange membrane fuel cells with a dead-ended anode. *Journal of Power Sources* **2014,** *246*, 90-94.

116. Chen, Z.; Peng, Y. T.; Liu, F.; Le, Z. Y.; Zhu, J.; Shen, G. R.; Zhang, D. Q.; Wen, M. C.; Xiao, S. N.; Liu, C. P.; Lu, Y. F.; Li, H. X., Hierarchical Nanostructured WO3 with Biomimetic Proton Channels and Mixed Ionic-Electronic Conductivity for Electrochemical Energy Storage. *Nano Letters* **2015,** *15* (10), 6802-6808.

117. Sun, W. M.; Yeung, M. T.; Lech, A. T.; Lin, C. W.; Lee, C.; Li, T. Q.; Duan, X. F.; Zhou, J.; Kaner, R. B., High Surface Area Tunnels in Hexagonal WO3. *Nano Letters* **2015,** *15* (7), 4834-4838.

118. Sheng, W.; Gasteiger, H. A.; Shao-Horn, Y., Hydrogen Oxidation and Evolution Reaction Kinetics on Platinum: Acid vs Alkaline Electrolytes. *Journal of The Electrochemical Society* **2010,** *157* (11), B1529-B1536.